FACULTY OF ENGINEERING AND ARCHITECTURE

Dynamic simulation of CO_2 utilization through Pressure Swing Chemical Looping

Vincent Minten
Student number: 01905039

Supervisors: Prof. dr. ir. Mark Saeys
Counsellor: Marian Flores Granobles

Master's dissertation submitted in order to obtain the academic degree of Master of Science in Chemical Engineering

Academic year 2020-2021

GHENT UNIVERSITY

FACULTY OF ENGINEERING AND ARCHITECTURE

Dynamic simulation of CO_2 utilization through Pressure Swing Chemical Looping

Vincent Minten

Student number: 01905039

Supervisors: Prof. dr. ir. Mark Saeys

Counsellor: Marian Flores Granobles

Master's dissertation submitted in order to obtain the academic degree of Master of Science in Chemical Engineering

Academic year 2020-2021

GHENT UNIVERSITY

Preface & acknowledgements

This master's dissertation marks the end of my two year degree in Master of Science in Chemical Engineering at UGent. Two years ago, after finishing my first degree of Master of Science in Chemical Engineering Technology at KU Leuven, I decided to go a step further to broaden my knowledge and try to satisfy my curiosity in this field of engineering. The many great opportunities and experiences make that this degree is certainly an added to my life and knowledge. The master's thesis subject about the conceptual analysis of the novel chemical looping process perfectly matched my interest in process modelling and sustainability.

Despite the mostly home-work – obliged due to the corona virus measures taken during my last year at the time of this thesis – I am very grateful for everything that came along my path during this study. Therefore, I would like to use this opportunity to thank the people who have guided and supported me during this process.

I would like to thank my coach Marian Flores Granobles for her excellent guidance, her honesty and true kindness during my thesis. Working with you has been a pleasure and certainly an added value. My words also go to Prof. Mark Saeys for the valuable discussions.

A special word of thanks goes to my twin-brother Matthijs and friend Ruben, with whom I started and finished this adventure. Thank you for the unconditional friendship, the continued support and motivation and all unforgettable memories we made together along this way. Last, but certainly not least, I am grateful for having the best people close to me; my dad with his ever-lasting care and support, my sister Mano for all the listening, my girlfriend Lotte for all the motivation and distraction and all my friends for making my university years the good times that I will cherish forever.

Vincent Minten, June 2021

Declaration concerning accessibility of this master's dissertation

The author(s) gives (give) permission to make this master dissertation available for consultation and to copy parts of this master dissertation for personal use. In the case of any other use, the copyright terms have to be respected, in particular with regard to the obligation to state expressly the source when quoting results from this master dissertation.

Vincent Minten, June 2021

Abstract

A novel combined chemical looping process further enhances CO_2 utilization via dry reforming of methane for the production of high purity CO. The dynamic behavior of the process using a pressure swing operation is not yet investigated. Therefore, this work aims at creating a first dynamic simulation based on thermodynamic equilibrium to gain more insights on the dynamic behavior of the pressure swing operation of the process in an isothermal packed bed reactor configuration.

Principles of pressure swing adsorption are used to configure a process cycle in which the pressure swing operation is used. The process is split in two separate operating regimes, i.e. a reducer and oxidizer regime. Further thermodynamic analysis of the regimes leads to the selection of favorable operating conditions. The development of an equilibrium model based on adsorption isotherms makes the implementation in the dynamic simulator program Aspen Adsorption© possible.

Finally, a combination of the constructed model and the dynamic simulator Aspen Adsorption© is able to simulate the dynamics of the pressure swing chemical looping concept at equilibrium. Analysis of the performance of the reducer and oxidizer regime provides insight on the dynamic behavior and the potential of the process. A sensitivity analysis on the performance of the process with different process parameters provides knowledge on the behavior of the process.

Keywords – CO_2 utilization, RWGS, chemical looping, pressure swing, packed bed, Aspen Adsorption©

Dynamic simulation of CO_2 utilization through Pressure Swing Chemical Looping

Vincent Minten

Supervisors: prof. dr. ir. Mark Saeys, ir. Marian Flores Granobles

Abstract— **A novel combined chemical looping process further enhances CO_2 utilization via dry reforming of methane for the production of high purity CO. The process consists of two chemical looping concepts; iron redox looping for the reverse water gas shift reaction and calcium looping for inherent CO_2 capture. The process leads to a superior performance in terms of CO production.**

This work aims at investigating the dynamics of the process in an isothermal packed bed through the development of a first, equilibrium process model via the dynamic flowsheet simulator Aspen Adsorption©. Based on pressure swing adsorption principles, a cycle is developed for the pressure swing operation of the process. A thermodynamic analysis based on thermochemical data of FactSage© yields equilibrium relationships that are used for determining suitable operating conditions for the pressure swing approach. An equilibrium model is developed based on adsorption isotherms and is implemented in the simulation software. The obtained dynamic simulation is used for an analysis of the process performance and a further sensitivity analysis is performed to investigate the effect of process variables.

The analysis of the dynamic behavior of the process yields numerous insights into the challenges and further optimization potentials of the process that can serve as a basis for a future more detailed development of a dynamic process configuration.

Keywords— **CO_2 utilization, chemical looping, RWGS, packed bed, pressure swing, packed bed, Aspen Adsorption©**

I. Introduction

TEMPERATURE increase caused by excessive greenhouse gas emissions has lead to the change of human and natural systems all over the world, with disastrous weather conditions, floods and biodiversity loss as a consequence. The Intergovernmental Panel on Climate Change (IPCC) [1] has urged to limit this increase to 1.5 °*C* compared to pre-industrial levels. Consequently, decarbonization of energy intensive industries such as steel and chemicals is crucial to meet the increasing needs of the future.

Carbon capture and utilization (CCU) technologies play a key role for active control of CO_2 emissions by the conversion of CO_2 into chemical building blocks. In this way, a carbon neutral economy can eventually be achieved.

The Flemish research program "Moonshot" [2] and the North-CCU-Hub consortium [3] both acknowledge that the Super-Dry Reforming of methane (SDR) is one promising novel CCU technology. This process converts CO_2 and CH_4 – both greenhouse gases – into CO which is an important platform molecule in both the chemical and steel industry. SDR – originally proposed by Buelens et al. [4] – is a combined chemical looping concept that couples chemical looping redox reactions and calcium looping for CO_2 capture. The overall reaction of the process is given by Eq. (1) and schematically presented in Figure 1.

$$CH_4 + 3\,CO_2 \rightarrow 4\,CO + 2\,H_2O \quad (1)$$

Two distinct reacting systems are present in the process. First a dry-reforming unit is used to convert CH_4 and CO_2 into an equimolar mixture of H_2 and CO by using a nickel catalyst. The higher CO_2:CH_4 ratio equal to 3 avoids the carbon formation regime of conventional dry-reforming. Secondly, the obtained syngas mixture enters the combined chemical looping unit that further increases the CO production by an enhanced reverse water gas shift reaction (RWGS). In this combined looping unit, a "*reducer*" and "*oxidizer*" regime can be differentiated.

In the reducer regime, the syngas mixture reduces the iron-based oxygen storage material (OSM), thereby producing H_2O and CO_2 according to Eqs. (2) and (3). In the meanwhile, CO_2 is adsorbed on the calcium sorbent material shown by Eq. (4), thereby enhancing the reduction of iron through Le Châtelier's principle. H_2O leaving the reactor during this step makes the process "super-dry".

$$2\,FeO + 2\,CO \rightarrow 2\,Fe + 2\,CO_2 \quad (2)$$

$$2\,FeO + 2\,H_2 \rightarrow 2\,Fe + 2\,H_2O \quad (3)$$

$$4\,CaO + 4\,CO_2 \rightarrow 4\,CaCO_3 \quad (4)$$

In the oxidizer regime, the operating conditions are altered so that calcination of $CaCO_3$ takes place as shown in Eq. (5). The released CO_2 re-oxidizes the iron, thereby producing a high purity CO product stream and driving the calcination of $CaCO_3$ further as shown in Eq (6).

$$4\,CaCO_3 \rightarrow 4\,CaO + 4\,CO_2 \quad (5)$$

$$4\,Fe + 4\,CO_2 \rightarrow 4\,FeO + 4\,CO \quad (6)$$

In this work a packed bed reactor configuration is used for the combined chemical looping process after the dry-reforming unit. Alternation between the reducer and oxidizer regime is performed by an isothermal pressure swing operation as shown in Figure 1. First, a high pressure is used in the reducer regime to let carbonation take place. Then, in the oxidizer regime, the pressure is decreased to let calcination take place by means of a self-purging mechanism.

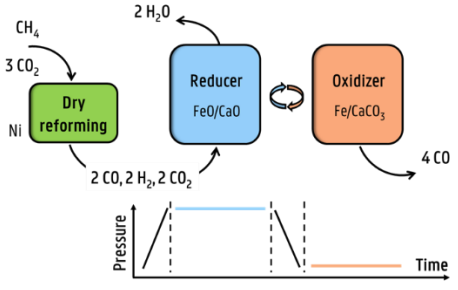

Figure 1: Schematic overview of the super-dry reforming process: a dry reforming unit followed by the combined chemical looping process in which a pressure swing operation is used to alternate between the "reducer" and "oxidizer" regime.

A process model for the dynamic simulation of such a pressure swing operation has not yet been developed. Therefore, this work aims at creating a first, dynamic simulation based on thermodynamic equilibrium to gain more insights in the dynamic behavior of the process. The model is then used in a sensitivity analysis to investigate the effect of process parameters on the process performance.

II. Methodology and Modelling Procedures

A. Aspen Adsorption© flowsheet simulator

For the dynamic simulation, Aspen Adsorption© is selected as the appropriate flowsheet simulator. The software is able to dynamically simulate reactive gas adsorption processes in a packed bed reactor configuration using a pressure swing operation. A cycle consisting of different steps is constructed by making use of the Cycle Organizer Tool of the software.

In the model several assumptions are made: the packed bed is modelled as a PFR reactor model, the gas phase behaves as an ideal gas, the pressure drop in the bed is determined by the Ergun equation, mass transfer is described by a linear driving force model and the bed is operated isothermally. A user defined equilibrium model is implemented in the software by using a FORTRAN code.

B. Process simulation at chemical equilibrium

The reactions taking place are; the redox reaction of iron with CO/CO_2 and H_2/H_2O, the carbonation/calcination reaction of calcium with CO_2 and the (R)WGS reaction. All are considered to be at thermodynamic equilibrium during the simulation. Consequently, thermodynamic relationships are required to describe the equilibria at the corresponding operating conditions. A model is then developed to describe the equilibria inside dynamically operated reactor.

1) Thermodynamic equilibrium

FactSage© is used to get acquainted with the thermodynamics of the system. Phase diagram analysis in the work of Claus [5] shows that the desired iron phases are FeO and Fe as they yield the highest CO purity. Consequently, only the latter two iron phases are considered in further equilibrium analyses.

Van 't Hoff relationships based on thermochemical data are constructed for all reaction as shown in Eq. (7)–(9). The equilibrium constant for the redox reaction of iron with CO/CO_2 decreases with increasing temperature due to the exothermicity of the reaction, whereas the opposite is true for the redox reaction of iron with H_2/H_2O. The combination of the latter two Van 't Hoff relationships describes the (R)WGS equilibrium. The equilibrium constant for the calcium system is equal to the equilibrium partial pressure of CO_2 and increases with increasing temperature because of the endothermicity of the calcination reaction.

$$K_{CO_2/CO} = \frac{P_{CO_2,eq}}{P_{CO,eq}} = 10^{\left(-1.0188+\frac{792.36}{T}\right)} \quad (7)$$

$$K_{H_2O/H_2} = \frac{P_{H_2O,eq}}{P_{H_2,eq}} = 10^{\left(0.4112--\frac{781.04}{T}\right)} \quad (8)$$

$$K_{Ca,CO_2} = P_{CO_2,eq} = 10^{\left(8.1282-\frac{9143.4}{T}\right)} \quad (9)$$

2) Equilibrium model based on adsorption isotherms

An equilibrium model is developed by which the gas mixture in the reaction mixture instantly reaches its thermodynamic equilibrium based on the available gas and solid reactants. The model takes into consideration the degree of conversion of the solid reactants, so that no further reaction can occur when the solids reach full conversion.

In this work, the equilibrium model represents the gas-solid reactions as individual adsorption processes. Herein, a gas phase component reacting with a solid is represented by adsorption on the solid, accompanied with the desorption of the corresponding product whilst taking into account the stoichiometry of the reaction.

Analogue to physical adsorption, the process can be described by the use of adsorption isotherms. These isotherms represent the amount of a component that can be adsorbed on a sorbent at equilibrium as function of the component's partial pressure for the corresponding temperature in *kmol.kg*$^{-1}$. A change in the partial pressure of the component or the temperature of the system, changes the loading of the component on the sorbent as shown in Figure 2.

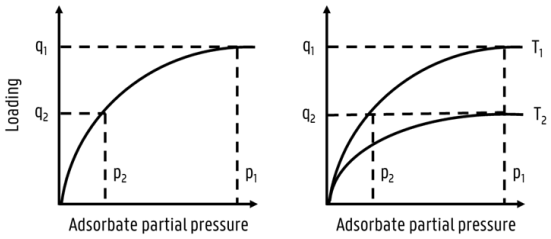

Figure 2: A change in loading of an adsorbate component due to a change in the partial pressure of the component or change in temperature of the system.

A gas-solid reaction can then be represented by a stepwise isotherm in which the loading of each component depends on the departure from its equilibrium. Instantaneous achievement of equilibrium is expressed by the stepwise profile of the isotherm as shown in Figure 3 with the following reasoning; in case the gas composition of A and B is higher than its equilibrium constant $K_{A/B}$ of its reaction with solid X, the reaction from A to B will be favored to reach equilibrium. Consequently, adsorption of A and desorption of B takes place. And *vice versa* for gas compositions lower than the equilibrium constant. Depending on the Van 't Hoff relation, the value of $K_{A/B}$ shifts these zones to the left or to the right.

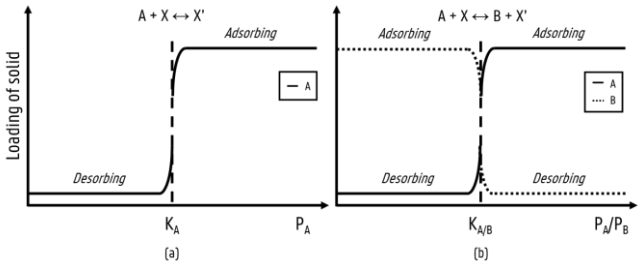

Figure 3: Schematic representation of gas-solid reactions by isotherms: (a) example of carbonation/calcination equivalent (b) redox of iron equivalent.

The maximal amount of loading for each solid is equal to the *mol* of solid available per *kg* of solid, i.e. the inverse of the molar mass of the sorbent, assuming 100% availability of the solid for reaction. The stepwise shape can be represented by a mathematical Sigmoid function in which the steepness of the curve can be manually adjusted. This equilibrium model is implemented in the Aspen Adsorption© flowsheet through a user defined FORTRAN code. Figure 4 represents the isotherm representations of the three gas-solid reaction of the system.

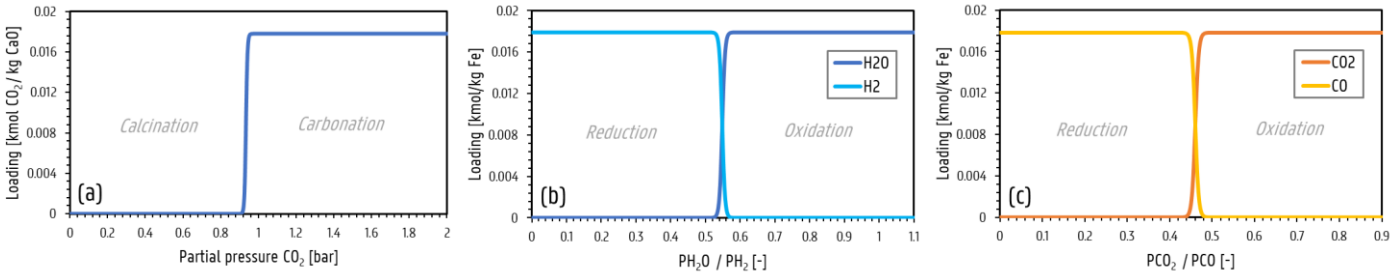

Figure 4: Adsorption isotherm representation of gas-solid reactions (a) carbonation/calcination of calcium in which loaded CO_2 represents $CaCO_3$ (b) redox of iron with H_2/H_2O in which loaded H_2 represents reduced iron and loaded H_2O oxidized iron (c) redox of iron with CO/CO_2 in which loaded CO represents reduced iron and loaded CO_2 oxidized iron.

In this isotherm approach, the loading of each gas-solid reaction changes separately and thus interaction between the loaded sorbent and other gas-solid reactions is not possible; this means that reduced iron by H_2/H_2O reaction cannot be used for reaction with CO/CO_2. Although the latter puts some limitation to the isotherm approach, it is shown to not significantly affect the dynamics of the process.

C. *Selection of operating conditions*

The equilibrium composition of the gas mixture in the reducer and oxidizer regime is subject to the thermodynamics of the two solid systems combined. The oxidizer regime yields the desired CO product stream and therefore its operating conditions are crucial in this process. The isothermal pressure swing operation of the reactor means that the oxidizer temperature also dictates the reducer temperature. Consequently, the selection of the operating conditions is a compromise of the reducer and oxidizer performance.

1) *Oxidizer regime*

The oxidizer regime is achieved by a pressure decrease in the reactor bed, thereby letting a self-purge of calcination take place. In this pressure swing operation, the minimum pressure is restricted to 1 *bar* and consequently, the temperature in the oxidizer regime should be chosen wisely.

During the oxidizer regime, calcination of calcium and oxidation of iron should take place at the same time. The released CO_2 re-oxidizes the reduced iron and produces the high purity CO stream. Consequently, the operating temperature should allow for operating in this region.

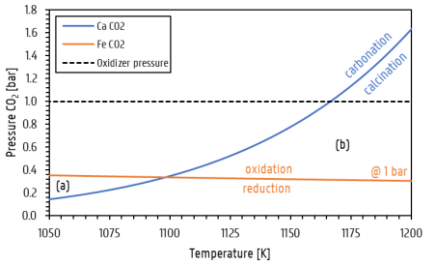

Figure 5: Equilibrium CO_2 pressure for calcium system (blue) and iron system at 1 *bar* total pressure (orange) as function of reactor temperature in oxidizer regime. Zone (a) iron reduction and carbonation (b) iron oxidation and calcination. Temperature of 1170 *K* required for operation in zone (b).

The CO_2 equilibrium pressure determined by the calcium and iron system for the oxidizer pressure of 1 *bar* is shown in Figure 5. The equilibrium pressure of the calcium system must be higher than that of the iron system to have a continuous driving force for calcination and oxidation of iron to take place. A temperature situated in region (b) is thus required. In case the opposite is true, carbonation and reduction of iron takes place as indicated by region (a), which is not the desired behavior of the oxidizer regime. Furthermore, for the initiation of the calcination reaction its equilibrium pressure must be higher than the oxidizer pressure of 1 *bar* to be able to generate a flow of CO_2 leaving the reactor. Consequently, a temperature of 1170 *K* yielding an equilibrium CO_2 pressure of 1.05 *bar* in the calcium system satisfies all aforementioned criteria and is selected as the operating temperature of the process. An equilibrium composition of 68.7 *mol%* CO and 31.3 *mol%* CO_2 can theoretically be obtained in the oxidizer regime.

2) *Reducer regime*

The high temperature required in the oxidizer regime to let the self-purging mechanism take place is, however, disadvantageous for the performance of the reducer regime. A increased temperature decreases the driving force for the carbonation reaction and of the reduction of iron with CO, consequently yielding an overall lower degree of reduction. A high pressure in the reducer regime is therefore required. A pressure of 15 *bar* is selected.

III. DYNAMIC SIMULATION OF COMBINED SOLID SYSTEM

After verification of the equilibrium simulation for a separate calcium and iron bed, the two solids are combined. The outlet of the dry-reformer unit from the work of Claus [5] is fed to the combined chemical looping reactor with 42.0 *mol%* CO, 24.8 *mol%* CO_2, 23.8 *mol%* H_2, 9.1 *mol%* H_2O and 0.09 *mol%* CH_4.

A. *Effect of combined solids*

The synergetic effect of the combination of the two solids is verified by simulating a reactor bed with alternating layers of calcium and iron. In Figure 6 (a) and (b) the composition profile in the reactor is shown in the reducer and oxidizer regime respectively.

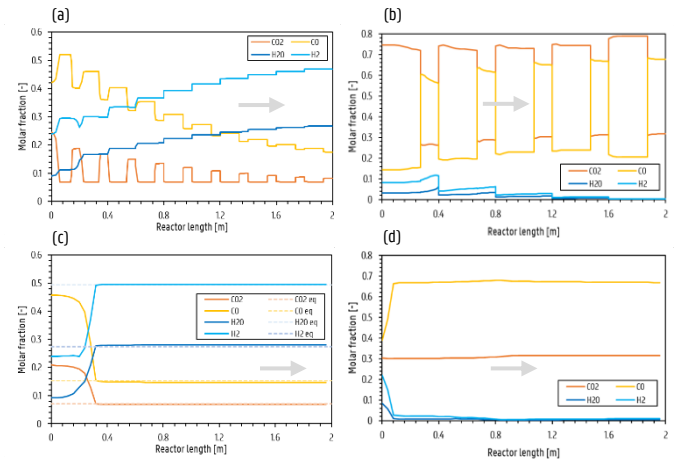

Figure 6: Composition profile in reactor in reducer and oxidizer regime respectively for alternating layers of calcium and iron (a), (b) and in a fully mixed bed of calcium and iron (c), (d). Arrow indicating direction of flow.

In the reducer regime it can be seen that carbonation takes place in the first calcium bed, thereby lowering the CO_2 partial pressure to its equilibrium pressure and creating a highly reducing mixture with respect to iron. In a subsequent iron layer, iron is reduced by CO and H_2 by which an increase in CO_2 and H_2O can be seen. In successive layers, carbonation and thereafter reduction of iron takes place again. This confirms that a continuous driving force for carbonation and iron reduction is created according to Le Châtelier's principle. At the end of the reactor, it can be seen that equilibrium is almost reached. In the oxidizer, the enhanced effect can be seen through a successive lowering of the CO_2 partial pressure going from a calcining $CaCO_3$ layer to an oxidizing Fe layer. In this way, again a continuous driving force for calcination and iron oxidation is generated according to Le Châtelier's principle. At the end of the bed, a molar fraction of 68.7 *mol%* of CO is achieved.

Figure 6 (c) and (d) show the composition profile in a reactor for a fully mixed bed of calcium and iron. Such a fully mixed bed can be described by an infinite amount of alternating layers of calcium and iron. Herein, the enhancing effect is utilized to its fullest and equilibrium is achieved almost instantaneously. Consequently, the continuous instantaneous driving force created in the reducer and oxidizer regime makes that full conversion is achieved the fastest. A fully mixed bed is thus beneficial for operation of this process.

B. *Simulation of pressure swing operation*

A full cycle of the combined chemical looping process using a pressure swing operation consisting of four steps is performed; (I) pressurization from 1 *bar* to 15 *bar*, (II) operation in reducer regime by feeding at 15 *bar*, (III) operation in oxidizer regime at 1 *bar* and (IV) a purge step for regeneration of the bed.

1) *Reducer regime*

Figure 7 represent the dynamic behavior of the conversion and composition profile in the reactor during the reducer regime. In the conversion and composition profile, two conversion fronts are developed:

(i) Towards the end of the bed, CaO and FeO are converted to $CaCO_3$ and Fe simultaneously by carbonation and reduction respectively. The composition can be seen changing close to the equilibrium composition of the reducer regime, yielding a raffinate product poor in CO and CO_2 and rich in H_2 and H_2O.

(ii) In the beginning of the bed, the calcium remains saturated whereas part of the reduced iron is re-oxidized again. The CO/CO_2 in feed retains its oxidizing nature because no CO_2 is taken out by the calcium sorbent, thereby re-oxidizing the part of reduced iron assigned to the CO/CO_2 reaction with iron. The reduced iron created by the reaction with H_2/H_2O cannot be re-oxidized by the CO/CO_2 mixture as there is no interaction because of the isotherm approach in this work. In the composition profile, the CO/CO_2 composition goes to its equilibrium.

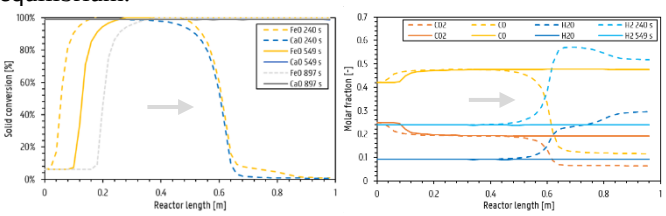

Figure 7: Dynamic behavior of conversion and composition profile in reactor during reducer regime at 1170 *K* and 15 *bar*. Arrow indicates flow direction.

At the end of the reducer regime, all calcium is carbonated in the reactor whereas only 80% of the iron is reduced. The other 20% is thus re-oxidized. This significantly affects the performance of the cycle as the reduced iron is required to produce CO in the oxidizer step.

2) *Oxidizer regime*

The feed of the reactor is stopped by closing the feed valve. Thereafter the product pressure is decreased to 1 *bar*, by which operation in the oxidizer regime starts. The calcination of $CaCO_3$ takes place in a co-current self-purging manner. Simultaneously with the conversion of $CaCO_3$ to CaO, Fe is oxidized as well thereby producing an extract product rich in CO, close to the equilibrium composition as shown in Figure 8. This product stream acts itself as a sweeping gas, thereby enhancing the calcination reaction. It can be seen that part of the reduced iron is not re-oxidized caused by the isotherm approach as earlier discussed.

The re-oxidation of iron in the reducer regime makes that there is no driving force for the $CaCO_3$ to calcine and consequently at the end of the oxidizer step, 20% of the $CaCO_3$ remains and can thus not be used for the production of CO.

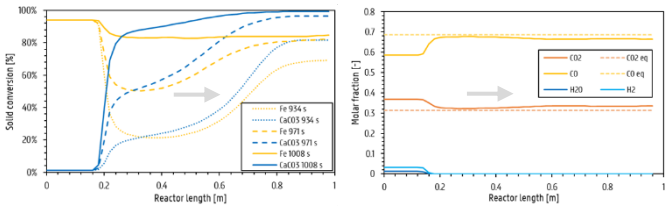

Figure 8: Dynamic behavior of conversion and composition profile in reactor during oxidizer regime at 1170 *K* and 1 *bar*. Arrow indicates flow direction.

3) *Purge step*

The bed is regenerated by using the raffinate product obtained in the reducer step as a purge stream. The latter is regarded more as a waste product and because of its low CO_2 partial pressure, it is an ideal purge stream. Figure 9 indicates that $CaCO_3$ is fully calcined, by which the released CO_2 further oxidizes the remaining reduced iron. Again, the reduced iron corresponding to the H_2/H_2O reaction can not be oxidized by CO_2. A product stream rich in CO_2 is obtained during this purge step.

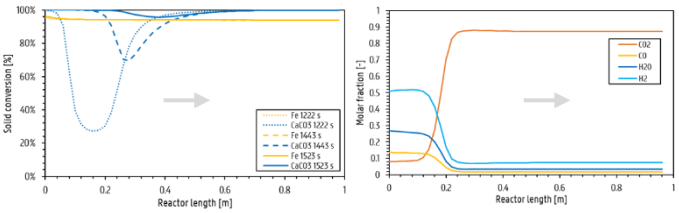

Figure 9: Dynamic behavior of conversion and composition profile in reactor during purge step at 1170 *K* and 1 *bar*. Arrow indicates flow direction.

4) *Overall cycle performance*

The overall performance based on the recovered CO and CO_2 gives an indication of the efficiency of the process. During the reducer regime, 75% of the amount of CO_2 and CO in the feed is retained in the bed in the form of $CaCO_3$. In the oxidizer regime, 80% of the CO_2 is recovered in the main extract product. Consequently, an overall feed conversion efficiency of 60% is achieved.

The overall performance of the cycle can thus be further optimized by maximizing the amount of CO and CO_2 retained in the bed and minimizing the fraction of reduced iron that is re-oxidized during the reducing regime.

C. *Sensitivity analysis*

The effect of the solid composition loaded in the bed and the feed pressure on the performance of the reducer regime is assessed in a sensitivity analysis.

1) *Solid composition*

In this sensitivity, total conversion of the end of the bed is simulated for different input ratios of iron and calcium initially loaded, all at 1170 *K* and 15 *bar*. All input ratios are chosen such that they are different relative to two system properties; i.e. the "*oxidizing ratio*" and the "*reducing ratio*".

The oxidizing ratio is the ratio of the final moles of oxidized iron achieved per mole of CO_2 at equilibrium of the reaction of CO/CO_2 with iron only. It thus represents the oxidizing power of the CO/CO_2 mixture and is equal to the equilibrium molar fraction of CO and its value is therefore only a function of the operating temperature.

The reducing ratio is the ratio of moles of reduced iron achieved per mole of carbonated calcium at equilibrium of the combined solid system. It represents the reducing power of the CO/CO_2 mixture created in the feed with respect to iron. It is a function of the operating temperature and pressure.

The simulation results show that the final ratio of reduced iron and carbonated calcium after the reducer regime is equal to the reducing ratio, independent of the input ratio as can be seen in Table 1. The operating temperature and pressure thus determine the final ratio of $CaCO_3$ and Fe.

The fraction of reduced iron and carbonated calcium are, however, dependent on the input ratio. On the one hand, it is observed that the fraction of reduced iron increases significantly with decreasing input ratio until the input ratio is equal to the oxidizing ratio. Thereafter, the fraction of reduced iron remains constant at a maximum value of approximately 89%. On the other hand, the fraction of carbonated calcium remains constant at approximately 100% for input ratios higher and equal to the oxidizing ratio. Whereas for lower input ratios, the fraction of carbonated calcium decreases significantly. The input ratio thus significantly affects the performance of the process, with an input ratio equal to the oxidizing ratio yielding both the highest fraction of reduced iron and carbonated calcium at the end of the reducer regime. Consequently, the oxidizing ratio yields the highest process performance.

Table 1: Simulation results of the effect of different input ratios of iron and calcium relative to the oxidizing ratio (OR) and reducing ratio (RR) on the performance parameters at the end of the reducer regime.

	OR = 0.687				RR = 0.619		
	R_1 >> OR	R_2 > OR	R_3 = OR	OR>R_4>RR	R_5 = RR	RR > R_6	RR >> R_7
R_i iron/calcium input	0.945	0.773	0.687	0.657	0.619	0.585	0.236
wt% calcium	0.500	0.550	0.579	0.590	0.600	0.610	0.800
wt% iron	0.500	0.450	0.421	0.410	0.400	0.390	0.200
Final Fe [kmol]	1.132	1.215	1.246	1.206	1.160	1.113	0.541
Final FeO [kmol]	0.599	0.302	0.152	0.148	0.139	0.131	0.055
Final CaCO3 [kmol]	1.825	1.958	2.012	1.957	1.870	1.794	0.884
Final Fe/CaCO3	0.621	0.620	0.619	0.616	0.620	0.620	0.612
% Reduced iron	65%	80%	89%	89%	89%	89%	91%
% Carbonated calcium	100%	100%	99%	95%	89%	84%	35%

Further analysis of the results reveal that these observations can be explained by looking at two different operating region as shown in Table 2; i.e. calcium as the limiting solid reactant and iron as the limiting solid reactant.

On the one hand, in case calcium is the limiting solid reactant, the fraction of reduced iron is determined by the potential of the system to reduce iron with the limiting amount of calcium present, i.e. input ratio and the reducing ratio. For this case, the fraction of carbonated calcium is 100%, as it is the limiting reactant and thus fully consumed.

On the other hand, in case iron is the limiting solid reactant, the fraction of reduced iron is determined by the oxidizing potential and the reducing potential of the system, i.e. the oxidizing ratio and the reducing ratio. Consequently, the fraction of reduced iron has a maximal value depending on both system properties, determined by the operating conditions. The fraction of carbonated calcium is then determined by the potential of the system to carbonate calcium with the limiting amount of iron present, i.e. the input ratio and the oxidizing ratio.

Table 2: Comparison of input ratio R_i with oxidizing ratio (OR) and reducing ratio (RR) to obtain theoretical fraction of reduced iron and carbonated calcium at the end of reducer regime.

% Reduced iron % Carbonated calcium	OR = 0.687				RR = 0.619		
Regimes	R_1 >> OR	R_2 > OR	R_3 = OR	OR>R_4>RR	R_5 = RR	RR > R_6	RR >> R_7
R_i iron/calcium input	0.945	0.773	0.687	0.657	0.619	0.585	0.236
RR/OR	90%	90%	90%	90%	90%	90%	90%
RR/R_i	65%	80%	90%	94%	100%	106%	262%
R_i/OR	138%	113%	100%	96%	90%	85%	34%
OR/OR	100%	100%	100%	100%	100%	100%	100%
Limiting reactant (OR)	Calcium	Calcium	/	Iron	Iron	Iron	Iron

At last it is observed that for decreasing input ratios lower than the oxidizing ratio, there is a build-up of $CaCO_3$ in the beginning of the reactor because of more calcium being available. Consequently, a higher fraction of the $CaCO_3$ will also be lost. For input ratios equal or higher than the oxidizing ratio, all $CaCO_3$ and Fe are distributed evenly.

2) *Effect of feed pressure*

A sensitivity analysis with the feed pressure as changing variable, operated with calcium as limiting reactant, indicates that for increasing feed pressure both the fraction of CO and CO_2 retained from the feed and the fraction of reduced iron in the reducer regime increases as shown in Table 3.

At lower feed pressures, less carbonation takes place accompanied with less conversion of CO to CO_2 and consequently more is lost in the raffinate outlet and less retained in the bed in the form of $CaCO_3$.

The increase in higher fraction of reduced iron for higher feed pressures is explained by the increasing reducing ratio. At high pressures, however, there is no significant difference between the reducing ratios. Consequently, a feed pressure of 15 *bar* is considered as a good trade-off between process performance and cost of compressor operation.

Table 3: Reducing ratio and corresponding calculated fraction of reduced iron compared to simulation results for feed pressures of 20, 15, 10, 7 and 5.5 *bar*.

	Input ratio = 0.773				
Feed pressure [bar]	**20**	**15**	**10**	**7**	**5.5**
Fraction CO+CO_2 retained	90%	86%	76%	56%	24%
% Reduced iron simulation	81%	80%	79%	75%	55%
Reducing ratio [mol Fe/mol $CaCO_3$]	0.623	0.620	0.610	0.580	0.427
Reducing ratio/input ratio	82%	81%	80%	77%	62%

IV. CONCLUSION

A novel combined chemical looping process that further enhances CO_2 utilization after a dry reformer reactor for the production of high purity CO is considered as a promising CCU technology.

In this work, a first dynamic simulation – of the combined chemical looping process using a pressure swing operation – is performed through an equilibrium process simulation in Aspen Adsorption© to gain insight in the dynamic behavior of the

process. An equilibrium model based on adsorption isotherms is developed and implemented within the simulation software. Herein, all gas-solid reactions are presented by adsorption processes that take place depending on the departure from their corresponding thermodynamic equilibrium. FactSage© is used for the construction of equilibrium relationships that further serve as the basis for the selection of the operating conditions in this work; i.e. an isothermal temperature of 1170 *K* and a feed pressure of 15 *bar* in the reducer regime and 1 bar in the oxidizer regime.

The simulation shows the ability of using a pressure swing operation for the combined chemical looping concept in a packed bed reactor.

In the first, pressurization step, the bed pressure is increased to reach the required reducer pressure of 15 *bar*. In the second, reducer step, the reactor is operated in the reducer regime by feeding the dry-reformer outlet at 15 *bar*. During this step, reduction of iron and carbonation of calcium takes place. A raffinate product close to the equilibrium composition, that is poor in CO and CO_2 is withdrawn. Thereafter, in the third oxidizer step, the reactor is operated in the oxidizer regime by decreasing the pressure to 1 bar. The release of CO_2 by a co-current self-purging mechanism is confirmed and by re-oxidation of the reduced iron, an extract product close to the equilibrium composition of 68.7 *mol%* CO is obtained. In the last purge step, the bed is regenerated by making use of a co-current purge with the raffinate product.

Although, the simulation does not yield the exact equilibrium compositions because of relaxed solver options, they remain within acceptable limits. The simulation provides key insights in the dynamic behavior of the reducer and oxidizer regime. In the reducer regime, it is found that in the beginning of the reactor bed, a significant amount of reduced iron is re-oxidized by the feed because of the saturation of calcium; 20% of the reduced iron is re-oxidized in the simulated case. In the oxidizer regime, it is found that only the $CaCO_3$ present together with the reduced iron is able to be recovered. These observations significantly affect the performance of the process.

A sensitivity analysis reveals that the solid composition of the bed dictates the operating behavior in the reducer regime. It is found that the re-oxidation of the reduced iron is inevitable. It can, however, be minimized by using an input ratio of iron and calcium equal to a so-called "*oxidizing ratio*", which is equal to the equilibrium partial pressure of CO with respect to its reaction with iron. Deviation from this optimal input ratio yields inferior performance in terms of fraction of re-oxidized iron and distribution of carbonated calcium and reduced iron. An increasing feed pressure is found to be superior in terms of the fraction of reduced iron and retention of CO and CO_2 during the reducer regime. However, at high pressures the difference in performance is found to be minor and consequently a pressure of 15 *bar* is a good trade-off between cost of compressor operation and achievable process performance.

As a first dynamic simulation, the equilibrium approach thus provides numerous insights into challenges of the process that could not have been assessed without its dynamic nature. These insights can be used to decide up on the viability of the process in terms of reactor selection and performance.

REFERENCES

[1] Intergovernmental Panel on Climate Change, "Global Warming of 1.5 ºC," 2021. https://www.ipcc.ch/sr15/ (accessed Jan. 27, 2021).

[2] Catalisti, "SDR," *Flanders Industry Innovation Moonshot*, 2021. https://moonshotflanders.be/mot3-sdr/ (accessed Jan. 27, 2021).

[3] North-CCU-Hub, "North-CCU-hub – Towards a climate-neutral economy in North Sea Port," 2021. https://northccuhub.eu/nl/ (accessed Jan. 27, 2021).

[4] L. C. Buelens, V. V. Galvita, H. Poelman, C. Detavernier, and G. B. Marin, "Super-dry reforming of methane intensifies CO2 utilization via Le Chateliers principle," *Science*, vol. 354, no. 6311, pp. 449–452, Oct. 2016, doi: 10.1126/science.aah7161.

[5] D. Claus, "Process simulation of CO2 utilization through Super-Dry Reforming," UGent, Gent, 2019.

Table of contents

List of figures

List of tables

List of abbreviations & acronyms

Abbreviation	Description
Eq(s).	Equation(s)
i.e.	Id est, Latin term for “that is” and “in other words”

Acronym	Description
Ca-L	Calcium Looping
CBFR	Circulating Fluidized Bed Reactor
CCS	Carbon Capture And Storage
CCS	Carbon Capture And Storage
CCU	Carbon Capture And Utilization
CCU	Carbon Capture And Utilization
DRM	Dry Reforming Methane
ET-PSA	Elevated-Temperature Pressure Swing Adsorption
EU	European Union
GHG	Greenhouse Gas
GM	Grain Model
GRAMS	Generalized Reaction-Adsorption Modelling and Simulation
IPCC	Intergovernmental Panel Climate Change
OSM	Oxygen Storage Material
PBR	Packed Bed Reactor
PFR	Plug Flow Reactor
PS	Pressure Swing
PSA	Pressure Swing Adsorption
RPM	Random Pore Model
RWGS	Reverse Water Gas Shift
RWGS-CL	Reverse Water Gas Shift Chemical Looping
SDR	Super-Dry Reforming
SERP	Sorption Enhanced Reaction Process
SESMR	Sorption Enhanced Steam Methane Reforming
SEWGS	Sorption Enhanced Water Gas Shift
SMR	Steam Methane Reforming
TS	Temperature Swing
UCM	Uniform Conversion Model
UDS1	Upwind Difference Scheme 1
WGS	Water Gas Shift

List of symbols

Greek symbols

Abbreviation	Description	Units
Γ_i	Discretization value	[units of variable]
ε_B	Bed porosity	[-]
ε_i	Interparticle voidage	[-]
ρ_g	Gas phase molar density	kmol.m^{-3}
ρ_s	Solid density	kg.m^{-3}
ΔG_r	Gibbs free energy of reaction	kJ.mol^{-1}
ΔH	Adsorption enthalpy	kJ.mol^{-1}
MTC	Mass transfer coefficient	s^{-1}
μ	Dynamic viscosity	N.s.m^{-2}
ψ	Sphericity factor	[-]

Roman symbols

Abbreviation	Description	Units
A	Pre-exponential factor	[units of constant]
C_{Ca}	Steepness factor Sigmoid function	[-]
c_i	Gas phase concentration	kmol.m^{-3}
CV	Linear valve constant	kmol.bar^{-1}.s^{-1}
E_A	Activation Energy	kJ.mol^{-1}
F	Molar flowrate	kmol.s^{-1}
K	Equilibrium constant	Bar^{-1}
M	Gas molar mass	kmol.kg^{-1}
MTC	Mass transfer coefficient	s^{-1}
P	(Partial) pressure	Bar
R	Universal gas constant	J.K^{-1}.mol^{-1}
r	Rate of reaction	[units of constant]
r_p	Particle radius	m
T	Temperature	K
v_g	Gas phase superficial velocity	m.s^{-1}
w	Loading	kmol.kg^{-1}
w^*	Equilibrium loading	kmol.kg^{-1}
y_i	Gas molar fraction	[-]
z	Axial distance	m
Z	Compressibility factor	[-]

Chapter 1

Introduction

1.1. Climate change – CCU as a pathway

The Intergovernmental Panel on Climate Change (IPCC) stated that human activities have increased the global temperature by approximately 1 °*C* in 2017 with respect to the pre-industrial level. The temperature rise to date has resulted in changing human and natural systems, including increasing extreme weather conditions such as droughts and floods, but also sea level rise and biodiversity loss. This changing climate affects people all round the world, but mostly people living in the lower income countries that will experience food insecurity and people living in coastal regions. The IPCC has urged to limit this increase to 1.5 °*C* only, since higher increase would make the transition to decrease the temperature drastically more difficult. [1]

The European Union (EU) has presented the Green Deal as an answer to the urgent climate change problematic. It is a strategy that enables the EU to grow towards a prosperous society in which economic growth is decoupled from resource use, thus focusing on circular economies. All of this while setting the goal to reach carbon neutrality by 2050, that is net zero greenhouse gas emissions (GHG). Energy-intensive industries such as steel and chemicals are indispensable for the modernization of civilization and the growing population because of their supply to key value chains, therefore the decarbonization of these sectors is essential. [2]

Extensive efforts have to be made in order to reduce GHG emissions to counteract the global warming. Predictions foresee that fossil fuels will retain a central role in industry, therefore key enabling technologies are carbon capture and storage (CCS) and carbon capture and utilization (CCU) for immediate decarbonization. The promotion of CCS and CCU requires commercial competitive technologies, CO_2 transportation and storage networks and industrial processes that use CO_2 as feedstock. [3]

CCU has drawn a lot of interest because of potential CO_2 emission reduction, replacement of carbon feedstocks and integration with renewable energy. CO_2 can serve the role of direct feedstock to produce chemicals such as urea, polycarbonate polyols and methanol. The latter is a platform molecule for a range of other reaction pathways. [3], [4]–[6]

In an alternative approach, the captured and stable CO_2 is converted to CO, a much more reactive molecule. CO is a platform molecule that is used in a wide variety of applications,

ranging from the steel and metal industry, for the reduction of ores, to the chemical industry, for production of acids, alcohols and esters. Consequently, by producing CO from CO_2, the potential of CCU technologies increases. [7], [8], [9]

The Flanders Industry Innovation Moonshot is a Flemish initiative which joins industries and governments to tackle the climate change challenge [10]. In this innovation program universities including UGent, research centers and industry combine their knowledge to develop breakthrough technologies for climate-friendly processes and products. One of the Moonshot research trajectories is about tackling the aforementioned challenge to convert captured CO_2 in usable raw materials, such as CO, methanol or dimethyl ether [11]–[14]. Besides the Moonshot initiative, also the North-CCU-Hub consortium is looking at ways to use captured CO_2 to synthesize high value products [15]. In both aforementioned initiatives, super-dry reforming of methane (SDR) is considered as a key technology for converting large amounts of CO_2 into a pure CO stream. In this work, a specific part of the SDR technology is elaborated upon.

1.2. CO_2 to CO production routes

Mixtures of CO and H_2 (syngas) are widely used in the chemical industry as platform molecules for bulk chemicals. The H_2/CO ratio of syngas depends on its production method. Nowadays, fossil fuels are the main source for syngas production. In light of current climate change challenges due to the rising CO_2 levels in the atmosphere, fossil-based processes must be minimized. One possible way to mitigate climate change is to use CO_2 as a carbon source instead of fossil carbon. [16]

Widely used methods for syngas production are steam methane reforming (SMR), coal gasification, reverse water gas shift and dry reforming of methane (DRM) [5]. In SMR, CO_2 is not consumed as a reactant but it is rather produced due to the combustion of fuel gases required to reach the high reforming temperatures. On the other hand, DRM requires CO_2 as a reactant, and proposes an interesting CCU approach. Although DRM produces more CO than SMR, it still requires further gas separation to obtain high purity CO. Consequently, further process adaptations are required in order to obtain high purity CO streams.

1.2.1. Dry reforming of methane

In DRM, the stable CO_2 molecule is converted to the more reactive CO molecule using a nickel based catalyst and CH_4 as reducing agent. This chemical reduction produces syngas (CO and H_2), as shown by Eq. (1.1), in an equimolar ratio. Because both methane and CO_2 are reactants, various feedstock can be used such as mixtures of methane and CO_2-rich gases

from capture processes or biogas, supporting the development of a carbon circular economy. However, due to the presence of the water gas shift reaction (WGS) as shown in Eq. (1.2), the CO product is subject to unwanted back reaction to CO_2 with H_2O. [5]

$$CH_4 + CO_2 \rightarrow 2\,CO + 2\,H_2 \qquad \Delta H^0_{298K} = 247\ kJmol^{-1}_{CH4} \tag{1.1}$$

$$CO + H_2O \leftrightarrow CO_2 + H_2 \qquad \Delta H^0_{298K} = -41\ kJmol^{-1}_{CO} \tag{1.2}$$

Other undesirable reactions like Boudouard reaction or methane decomposition could lead to carbon deposit formation and to catalyst deactivation. [5], [9]

DRM consumes 247 $kJmol^{-1}_{CH4}$, whereas SMR only consumes 206 $kJmol^{-1}_{CH4}$ [17], because of the need to overcome the high activation energy due to the inert nature of CO_2 in the DRM reaction. The obtained equimolar mixture of H_2/CO by DRM can be used for limited applications only, such as acetic acid production. Syngas mixtures with ratios of H_2/CO between 1.7-2.4 are suitable for methanol production and Fischer-Tropsch synthesis. Syngas with a higher CO content (H_2/CO of 0.4) can be produced via an additional reverse water gas shift reaction (RWGS) and can be used to obtain valuable high purity CO feedstocks. [17]

1.1.1. Super-dry reforming, a combined chemical looping process

A proposed concept for higher CO purity is the super-dry reforming process originally developed by Buelens et al. [9]. SDR is a combined process that includes DRM and a chemical looping redox system involving the RWGS reaction and inherent CO_2 capture by a sorbent material.

The concept of chemical looping was first introduced by Ishida et al. [18] for combustion processes in power generation industry. Herein, the overall reaction is split up in two separated subsystems, involving a chemical intermediate that is cycled successively through both subsystems, thereby coupling both reactions. For chemical looping combustion, a solid oxygen storage material (OSM), i.e. metal oxide, is the intermediate that is successively reduced and oxidized. This chemical looping concept results in an inherent separation of product gases, because direct contact of the two subsystems is avoided. Consequently, separation of e.g. CO_2 from waste gases is simplified and energy requirements for conventional intensive separation processes are avoided. The looping of two subsystems also offers possibilities of coupling of exothermic and endothermic reactions steps, thereby increasing heat recovery. [19], [18]

Chemical looping can also be applied for CO_2 capture, of which calcium looping (Ca-L) is an example. This method is used for CO_2 removal within chemical processes and for intrinsic CO_2 capture in sorption-enhanced reactions such as sorption enhanced steam methane reforming, thereby enhancing the production of H_2 according to Le Châtelier's principle and simplifying CO_2 separation [20]. A carbonation-calcination cycle is used for the capture and release of CO_2, according to Eq. (1.6).

In SDR, first a nickel-based catalyst is used to catalytically convert CH_4 and CO_2 to syngas products, according to the DRM reaction (Eq. (1.1)), with methane conversions up to 99% [5]. Subsequently, a combined chemical looping process of the RWGS reaction and CO_2 capture is performed to maximize the CO yield and to ease its separation. Two solids intermediates are required in this combined chemical looping process: Fe-based OSM for the RWGS reaction and a Ca-based sorbent for CO_2 capture.

In a first step, FeO is reduced to Fe while converting CO in CO_2 and H_2 into H_2O by making use of lattice oxygen as shown in Eqs. (1.3) and (1.4), respectively. Oxidation of syngas over iron oxide may remain only partial because of the WGS. Therefore, to ensure an improved degree of oxidation, CO_2 is inherently removed by CO_2 capture over CaO sorbent according to Eq. (1.5), to enhance syngas oxidation according to Le Châtelier's principle. All these steps occur during the called 'reducer' regime. Then in a second step, the so called 'oxidizer' regime, CO_2 is released from the Ca-based sorbent, and it re-oxidizes iron yielding high purity CO, according to Eqs. (1.6) and (1.7), respectively. The global reaction of the SDR process is then shown in Eq. (1.8) [9], while CO and H_2O are inherently separated in two different streams through the chemical looping process.

Reducer

$$2\,FeO + 2\,CO \rightarrow 2\,Fe + 2\,CO_2 \qquad \Delta H^0_{298K} = -18\ kJmol^{-1}_{CO} \qquad (1.3)$$

$$2\,FeO + 2\,H_2 \rightarrow 2\,Fe + 2\,H_2O \qquad \Delta H^0_{298K} = 16\ kJmol^{-1}_{H2} \qquad (1.4)$$

$$4\,CaO + 4\,CO_2 \rightarrow 4\,CaCO_3 \qquad \Delta H^0_{298K} = -178\ kJmol^{-1}_{CO2} \qquad (1.5)$$

Oxidizer

$$4\,CaCO_3 \rightarrow 4\,CaO + 4\,CO_2 \qquad \Delta H^0_{298K} = 178\ kJmol^{-1}_{CO2} \qquad (1.6)$$

$$4\,Fe + 4\,CO_2 \rightarrow 4\,FeO + 4\,CO \qquad \Delta H^0_{298K} = 18\ kJmol^{-1}_{CO} \qquad (1.7)$$

$$CH_4 + 3\,CO_2 \rightarrow 4\,CO + 2\,H_2O \qquad \Delta H^0_{298K} = 330\ kJmol^{-1}_{CH4} \qquad (1.8)$$

The SDR process avoids the main disadvantages of conventional DRM. Firstly, in the reformer section the deactivation of the DRM catalyst by carbon deposits is completely avoided by using a higher CO_2:CH_4 feed ratio of 3. This brings the system beyond carbon formation regime and lowers the upper temperature limit for carbon formation [21]. Secondly, the redox reaction of iron is no longer limited by the WGS reaction, because of the inherent CO_2 capture and water separation in the chemical looping process. This explains the origin of the name “super-dry” reforming. As consequence, H_2O will be produced instead of H_2, due to the reverse water-gas shift reaction. Compared to DRM, SDR is intensified process that converts up to three CO_2 molecules per molecule of CH_4. [8], [9]

1.2. Scope of this work

A detailed discussion on the development of the super-dry reforming process, the selection and characterization of the looping materials has been given in the work of Buelens et al. [9]. Thereafter, in the work of Claus [8] a first complete steady state kinetic study of the super-dry reforming process was performed in Aspen Plus©. The latter work gave insights on the process behavior and interactions between the different steps in a steady-state approach.

This work, however, focuses on the combined chemical looping concept of the SDR process, i.e. the process unit after the dry-reforming unit. The process is separated in two alternating regimes: the “reducer” and “oxidizer” regimes, referring to the reaction involving the oxygen storage material. Different reactor configurations can be used to alternate between these two regimes; on the one hand, the regimes can take place in separate reactors by which there is a separation of space. For this configuration circulating fluidized bed reactors (CFBR’s) can be chosen. On the other hand, by using one reactor, the regimes can take place by a separation in time. This configuration requires dynamically operated packed bed reactors (PBR’s) [8], [22]. In this work, a dynamically operated packed bed reactor is chosen for the combined chemical looping unit after the dry-reformer unit in the super-dry reforming process.

In a dynamically operated packed bed reactor, there is a need to cycle between the reducer and oxidizer regimes by means of changing the process conditions. The CaO sorbent has a finite CO_2 uptake capacity and the iron oxide has a finite oxygen storage capacity. As a result, the sorbent and the oxygen carrier need to be periodically regenerated by cycling to the next operating regime. There are three different operational modes for this process; firstly, an isobaric temperature swing (TS) approach, in which the temperature is used to switch from reducer to oxidizer and vice versa; secondly, an isothermal pressure swing (PS) approach, in which pressure change is used to alternate between reducer and oxidizer; or lastly, switching

from feed source, in which syngas is used in the reducer regime and an inert purge gas is used in the oxidizer regime to lower the partial pressure of CO_2.

In this work an isothermal pressure swing approach is used because it has several advantages over the other operation modes; i) varying pressure inside a reactor is faster than varying temperature, especially when solids are present, ii) temperature swing prohibits heat transfer between low temperature endothermic regime and high temperature exothermic regime, iii) temperature swing approach requires a compromise of very high temperatures and pressures or lower performance due to increased carbon formation. The work of Claus [8] proposed an operating temperature of 820 *°C* and a pressure of 15 *bar* in the reducer regime and 1 bar in the oxidizer regime.

The isothermal pressure swing operation of the packed bed reactor for the combined chemical looping process is shown schematically in Figure 1-1. After the dry-reforming unit, the outlet stream is fed to the combined chemical looping process that is further investigated in this work. A high pressure will favor the carbonation reaction and enhance the reduction of the oxygen carrier in the “reducer” regime, while in the “oxidizer” regime a low pressure will enhance the calcination reaction by which CO_2 is released for the reoxidation of the oxygen storage material. Small amounts of inert purge stream can be necessary for cleaning regeneration of the packed bed to be able to restart the cycle. [8], [9]

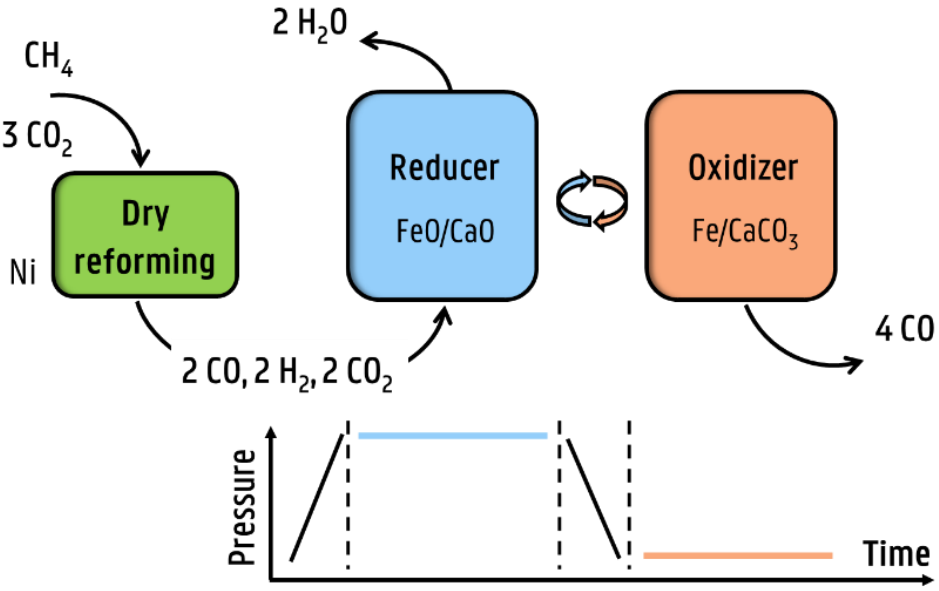

Figure 1-1: Schematic overview of the super-dry reforming process concept making use of a pressure swing operation. A nickel catalyst is used for the dry reforming reaction in a separate reformer reactor; reformate product is sent to the RWGS Chemical Looping system in which alternation from reducer to oxidizer and vice versa is done by means of pressure swing operation. In the reducer, FeO reduction by H_2 and CO takes place while CO_2 is inherently captured, as a result the main product is H_2O. In the oxidizer, calcination of $CaCO_3$ occurs and Fe is reoxidized by CO_2, the product stream consists of mainly CO.

This work aims to go a step further and provide a full dynamic simulation of the combined chemical looping process in a packed bed reactor with a pressure swing operation mode by using the simulation software Aspen Adsorption®. Analysis of the process will provide more insights on the reactor dynamics, achievable products compositions and recoveries and will serve as a basis to determine a process configuration where multiple reactors operate parallelly to ensure a continuous production high purity CO stream. The purpose of this work is not to precisely predict the reactor performance, but to provide insights and a good understanding of the dynamic behavior of the bed which will be a basis for the design of future experiments.

Chapter 2

Literature review: Reactor choice for dynamic operation

In this work, the reaction of interest is the reverse water gas shift reaction that converts CO_2 to CO by consuming H_2. Introducing a chemical looping concept for the RWGS splits the reaction in a reduction and oxidation reaction. Chemical looping separates reactants spatially thereby avoiding side reactions [16]. Chemical looping is an emerging technology for production of fuels, chemicals and electricity via combustion of fuels. The separation of undesired products generated during reactions are avoided, yielding an overall efficient, economical and low-emissions process. [23]

A metal oxide is used as an oxygen storage material for the redox looping reaction. This process is referred to as reverse water gas shift chemical looping (RWGS-CL). The RWGS is further enhanced by adding a calcium looping (Ca-L) system.

The reactor choice for the combined chemical looping process in this work is dependent on its operation requirements. First of all, the reactor has to contain solid intermediates for the RWGS-CL and Ca-L. Secondly, the reactor has to work at high temperatures of 800-900 °C. And lastly, it should be possible to swing between high and low pressures easily.

In the coming sections, first the available reactors are discussed to decide which reactor suits the combined chemical looping process for the RWGS reaction the most. Thereafter, a closer look is taken to processes that show resemblances with this process; i.e. chemical looping processes, sorption enhanced reaction processes and pressure swing adsorption.

2.1. Chemical looping reactors

There are two main type of reactors currently used for chemical looping reactors; i.e. circulating fluidized bed reactors and packed bed reactors. Packed bed and fluidized beds remain, because of their relative simplicity and well known behavior, the industrial preferred reactor types [16]. A general overview of the reactor types and their application is given together with all their (dis)advantages that will lead to the choice of reactor type for this work.

2.1.1. Fluidized bed reactors

Chemical looping combustion is the most mature chemical looping technology mentioned in literature for which mainly CFBR's are used [19]. In this configuration, physical transport of the oxygen storage material takes place between the oxidizer (air reactor) and reducer (fuel reactor) as shown in Figure 2-1. The fuel is injected in the reducer by which the oxygen storage material is reduced, thereby producing the combustion products. While in the oxidizer, the reduced oxygen storage material is reoxidized again to be sent to the reducer afterwards. Because the production of heat occurs in two steps in two separate reactors (reducer and oxidizer reactors), the dilution of the combustion products by N_2 is avoided and thus the subsequent CO_2 capture step is facilitated. In this process configuration, however, cyclones are required for gas-solid separation.

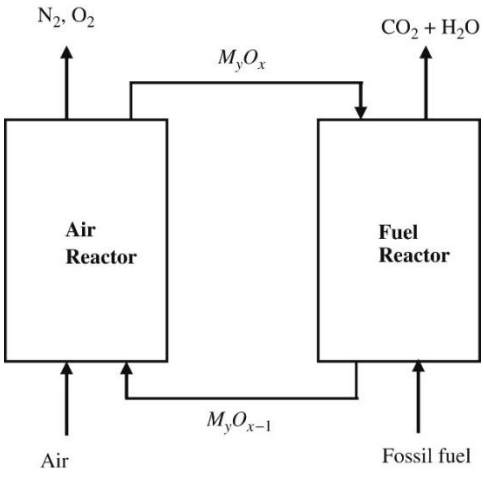

Figure 2-1: Schematic of chemical looping combustion in a circulating fluidized bed reactor; oxygen storage material cycled through air reactor for reduction and fuel reactor for oxidation. [19]

Chemical looping combustion using CFBR's is operated in several cases only at atmospheric pressure. While it is preferred to operate the process at higher pressures to achieve better energy efficiency [22], [24], [25], [26]. CFBR's at high pressure are still under development and are found to have difficulties with maintaining solid circulation [8], [22], [25]. Because in this work, elevated pressures up to 15 *bar* are used in a pressure swing operation, this might add big limitations to the system when using CFBR's. Ca-L is known to be performed in CFBR's for enhancing coal gasification or in carbon capture of flue gases. Herein, the heat demand for sorbent regeneration is provided by combustion of fuel with pure oxygen. This high heat demand makes the process very energy intensive [27], [28].

CFBR's show high mixing characteristics and provide good gas-solid contact. Another advantage is their capability to work at high temperatures and excellent heat transfer properties, which is advantageous for the exothermic reducer reactor and endothermic oxidizer

reactor. Consequently, they are less prone to form hotspots and material sintering [29]. The reactor operates in fluidized state and thus smaller particles can be used as there are no pressure drop issues under this operation [24].

The main drawback for CFBR's – acknowledged by multiple authors – is associated with the attrition of the solids, caused by mechanical and chemical stress during operation [24], [16]. This attrition causes fines to be produced, which give rise to separation issues in the cyclones. These losses in solids give rise to additional cleaning steps needed, which increase the total capital cost [24]. Another limitation is found in the operation of CFBR's due to limited flexibility in gas flow velocities opposed by the hydrodynamics of the system [16]. Particle agglomeration is another problem that possibly causes bed de-fluidization, thereby decreasing the performance of the reactor.

2.1.2. Packed bed reactors

Alternatively, the solids can be kept stationary while reactor conditions are switched, which can be achieved in a dynamically operated packed bed reactor configuration [22]. In principle, the fixed bed is switched between consecutive reduction and oxidation regimes. Chemical looping combustion can be performed by making use of a packed bed reactor as shown in Figure 2-2. First the fuel is sent over the oxidized oxygen storage material, by which it is reduced. When the bed is reduced, the fuel gas is switched to either first a purge gas to clean the bed or right away an air flow to re-oxidize the reduced oxygen storage material. In this way, the mixing of air products and combustion products is intrinsically avoided as well, thereby facilitating the separation subsequent CO_2 separation step. To obtain a continuous product stream, at least two parallel reactors working alternatively are required. [24]

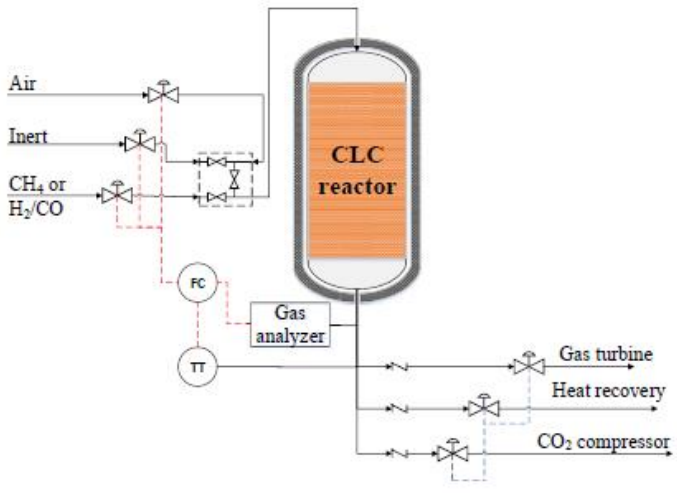

Figure 2-2: Schematic representation of chemical looping combustion in a fixed bed configuration: oxygen storage material remains stationary while feed enters for reduction and air enters for oxidation in a cyclic manner. [24]

PBR's have some advantages over CFBR's. First, they are known to have stable operation under elevated pressures and their operation is simpler and more known in industry [30]. Moreover, PBR's are used in pressure swing processes such as pressure swing adsorption [31]. Secondly, separation of gas and solids are intrinsically avoided and no fines are produced which avoid additional operation costs for its separation of the system [22], [24], [30], [32]. The solids inside a PBR are stationary and thus attrition issues are intrinsically avoided as well. The solids can, however, still suffer from constantly changing operating conditions.

Disadvantages of alternating PBR's include the need to use high temperature, high pressure, high flow gas switching systems. To deploy this technology at full scale, a sophisticated system of valves for different feeds and outlet gases is necessary, thereby increasing the cost of the process. Besides that, the discontinuity of flow can cause more wear on the installation [30], [26]. In large PBR's, oxygen carriers larger in size are favored compared to CFBR's to minimize pressure drop and plugging [24].

At last, heat transfer in PBR's is limited contrary to CFBR's. Consequently, agglomeration and sintering are more likely because of hotspot formation and can cause severe decrease in oxygen carrier performance over time [16], [29], [24], [25]. Heat management during the alternating reduction and oxidation step can be challenging. Several authors distinguish 2 different fronts inside the reactor, a reaction front and a heat front [30], [32]. Consequently, the PBR can be used as a temporary heat storage medium between the exothermic reduction step and endothermic oxidation step, thereby possibly yielding autothermal operation. Isothermal operation can be achieved when heat of reaction of endothermic and exothermic don't differ too much [23]. Therefore, PBR's for Ca-L recently also got interest for better heat management, as the heat of exothermic carbonation can be stored in the solids and used for the endothermic calcination later on [33].

In the SDR process, a similar heat management can be applied for the overall exothermic reduction step and endothermic oxidation step in a PBR configuration. In this work, however, an isothermal operation is assumed to decrease the complexity of the process. The pressure swing chemical looping concept works at elevated pressures, therefore a PBR configuration is the preferred reaction configuration as CFBR's have limitations under these conditions. Consequently, based on all above findings, in this work a PBR reactor will be used.

2.1.3. Packed bed reactor for Pressure Swing Chemical Looping

The combined chemical looping of the SDR process using a pressure swing operation consists of several successive steps that make up the full cycle. First the reformer outlet as feed gas at high pressure (15 *bar*) pressurizes the PBR. Subsequently, the product valve is open and the

PBR is operated in its reducer regime at this elevated pressure, in which carbonation is also taking place. Thereafter, the feed valve is closed and the pressure is vented to 1 *bar* to favor calcination and to let oxidation take place simultaneously. The SDR process in a PBR is a combination of i) a chemical looping concept, ii) a reactive and adsorption process with the Fe and Ca solid and iii) a pressure swing operation. The following sections discuss similar processes that demonstrate resemblances with the SDR process and serve as a benchmark for the reactor configuration of this process.

2.1.3.1. Chemical looping in packed bed reactors

Heidebrecht et al. [34], [35] investigated the behavior of a PBR for cyclic water gas shift reactor to produce H_2. In this chemical looping concept, FeO is used as an oxygen carrier and first reduced by syngas. Thereafter, Fe is reoxidized with steam, producing high purity H_2. They concluded that using a reverse flow configuration in alternating steps is advantageous for solid conversion. Wenzel et al. [16] investigated CO production from CO_2 by RWGS chemical looping with Fe in in both a PBR and CFBR at 1073 *K* and atmospheric pressure. First, H_2 is used to reduce the iron oxygen carrier. When the FeO is fully reduced, the feed is switched to counter-current flow of CO_2, which regenerates the FeO, thereby producing CO. They concluded that not much difference exists between a PBR and CFBR in terms of yield for continuous CO production. They, however, suggest that a PBR is advantageous over the CFBR because the former provides more degrees of freedom.

Several examples of packed bed reactors for a combined chemical looping process also exist. Most of them are found in sorption enhanced reaction processes (SERP). SERP show similarities with the SDR process which is of interest in this work. The formers are based on Le Chatelier's principle, in which a combined adsorption-reaction process is used. Herein adsorbent acts both as a support and a medium to adsorb intermediates formed during the reaction, thereby shifting the equilibrium towards the products by in-situ capture of one of the by-products. Consequently, high purity products are obtained and downstream processing could be eliminated [36]. This concept has been studied for various processes, e.g. sorption-enhanced water gas shift (SEWGS) and sorption-enhanced steam methane reforming (SESMR). The dynamic nature of the adsorption-reaction process makes the process modelling a complex task. However, literature provides numerous examples of modelling approaches and because of similarities with the super dry reforming process these can provide a good basis for its adsorption kinetic modelling.

Abanades et al. [30], [37, p. 2] investigated SESMR. This process consists of solid looping with CaO that serves as a high temperature (600-700 °*C*) CO_2 capture sorbent, combined with a second chemical loop of CuO/Cu for reforming of CH_4. The packed bed is used to store the

heat of the exothermic reduction of CuO with CH_4 for provide the heat for the calcination of $CaCO_3$ in a next step. Herein, the oxidation of Cu to CuO is carried out with air at 10 *bar*. Ridha et al. [38] used a CaO/CuO combined chemical looping concept for chemical looping combustion with focus on CO_2 capture. Carbonation takes place at 650 °*C*, whereas calcination takes place at 850 °*C* by using an additional air flow.

2.1.3.2. Chemical looping modelling

Arora et al. [39] provide a generalized reaction-adsorption modelling and simulation (GRAMS) framework capable of covering both reaction and adsorption dynamics in fixed-bed reactors with solid oxygen storage materials, porous adsorbents or both. GRAMS can be used for pressure swing adsorption (PSA) and SERP. GRAMS modelling framework states all required transport equations for conservation of mass, energy and momentum. Herein, gas-gas and gas-solid reaction kinetics and isotherms for adsorption processes can be implemented. The following examples of are processes modelled based on the GRAMS approach. A SERP for methanol production in which H_2O is adsorbed by NaX zeolite at 300 °*C* [40]. A SESMR model of Solieman et al. [20] in which CaO is used to capture in-situ CO_2 at a temperature of 600 °*C* and 17 *bar*, while desorption is performed at 1 *bar* and 820 °*C* using steam as purge. This work shows similarities with the conditions used in our combined chemical looping process, it is however only a conceptual analysis. Lee et al. [41] proposed a model for the transient behavior of SESMR with CaO for CO_2 removal in a packed bed reactor. Circar et al. [41] suggested also a SESMR process in which K_2O is used to reversibly adsorb CO_2 at temperature of 450 °*C* and 4.8 *bar*. The regeneration of the adsorbent is performed by a purge step of 400 °*C* and 1 *atm*.

The aforementioned examples show resemblances with the pressure swing chemical looping concept in this work. Iron is also used as OSM and combined with CaO as a sorbent for inherent CO_2 capture. The main difference with the SDR process lies in the regeneration step, or oxidizer regime in this work. Some examples use an additional air flow in the oxidation step, whereas in this work during oxidation $CaCO_3$ is calcined by means of decreasing the CO_2 partial pressure isothermally, i.e. producing a self-purge**.** The combined pressure swing chemical looping process of the SDR process is thus unique in its kind and no similar reference is found in literature.

SERP shows similarities with the SDR process. In this case, physical adsorption is taking place, an isotherm is used to describe the equilibrium loading together with a mass transfer model based on a linear driving force accounting for diffusional limitations. When a chemisorbent, such as CaO, is used, in the governing mass balance a stepwise isotherm is used. This resembles instantaneous achievement of the thermodynamic equilibrium of the

carbonation/calcination reaction. The latter is used together with a mass transfer model. In another approach the carbonation/calcination reaction kinetics are used in the governing mass balance. The GRAMS framework thus seems suitable for the SDR process in this work and can be modelled in a software like Matlab©, but programs containing this modelling framework already exist, namely Aspen Adsorption©. The latter provides a graphical user interface such as in Aspen Plus© in which a packed bed reactor can be simulated with all different inputs ranging from gas-gas reaction, gas-solid reactions, adsorption or a combination thereof. Moreover, it is suitable to simulate pressure swing operations. Aspen Adsorption© is available at the Laboratory for Chemical Technology at UGent and will consequently be used to model the dynamic SDR process.

Chapter 3

Literature review: Pressure swing operation

3.1. Pressure swing adsorption

Pressure swing adsorption is a mature technology and a wide variety of industrial applications operate using PSA working principles. Examples are drying of air by selectively adsorbing water on silica and H_2 purification separation from CO_2 using activated carbon [31]. In this work pressure swing operation will be used for CO_2 sequestration and subsequently its release and conversion to CO. Most PSA processes operate at low temperatures because physisorbent are used, whereas, in this work high temperatures are used by using chemisorbents. Nevertheless the same working principles apply and therefore a basic understanding of pressure swing adsorption operation is required and is discussed in this section.

3.1.1. Adsorption fundamentals

Gas separation by adsorption is a multistep process in which a molecule moves from the bulk fluid phase in to the pore phase of a solid particle, where it becomes attached to the surface by either physisorption or chemisorption [42]. Industrial applications of adsorption depend on differences in the affinity of a solid surface for different molecules. The crucial requirement is an adsorbent that is able to preferentially adsorb one or all expect one of the components. The selectivity depends on a difference in sorption rates or on a difference in adsorption equilibrium [31]. The product obtained during the adsorption at high pressure is referred to as raffinate. The adsorption step is followed by a regeneration step. In the latter, the regeneration occurs by pressure swing adsorption (PSA), by temperature swing adsorption (TSA) or a combination thereof. The working principles are shown in Figure 3-1. Higher pressures increase the amount of adsorbed species loaded on the adsorbent. Thus, regeneration is possible by decreasing the pressure. Analogously, TSA has a decreasing loading capacity at increasing temperatures. The desorbate recovered during regeneration is referred to as extract. In contrast to TSA, changing the pressure in a PBR can be done faster than changing the temperature, and therefore PSA operation is the most common in practice. Ideally, a PSA process operates at

isothermal conditions, consequently the working capacity is determined by the difference in loading between the feed and regeneration pressure, on the same isotherm. [31], [42], [43]

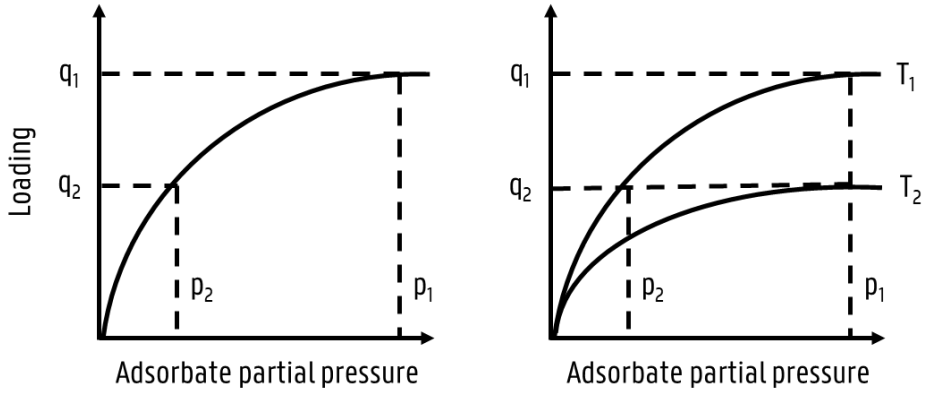

Figure 3-1: Schematic working principle of working principle of a PSA cycle (left) and a combination of PSA and TSA (right) given in a diagram of adsorbent loading as a function of adsorbate partial pressure.

3.1.2. Sorbents: physisorption and chemisorption

Solid surfaces cause a reduction in the potential energy of gas molecules because of their interactions. Consequently, gas molecules will concentrate in the vicinity of solid surfaces, increasing the molecular density compared to the bulk phase. The surface forces depend on the nature of the solid and the sorbate. In case weak forces - such as van der Waals interactions - are present, physisorption takes place. No chemical bond is formed, there is only a weak interaction between the adsorbed specie and the solid surface. The energy barrier needed to overcome is very small and consequently the process of adsorption and desorption are reversible and approximately non-activated. The adsorption rate is high at low temperatures [43]. On the other hand, if strong forces are present such as electron transfer, chemisorption is occurring [31]. The energy barrier is higher compared to physisorption and thus it is an activated process. Consequently, it is a slow process at low temperature, but very fast at high temperatures. The regeneration of a chemisorbed specie requires a very high temperature or low pressure. Both physisorption and chemisorption are exothermic processes, with the adsorption heat equal to the heat of condensation (-20 to -40 $kJ.mol^{-1}$) and the reaction heat (-40 to -400 $kJ.mol^{-1}$) respectively [43],[44].

Chemisorption is limited to a monolayer, while in physical adsorption multiple layers can be formed. Most practical adsorption separation processes at low temperature depend on physical adsorption rather than chemisorption because of too slow kinetics and capacity of chemisorption for economic viability [31]. At higher temperature, however, chemisorption is fast.

The adsorbent should be chosen such that there is a difference in the forces of the adsorbing molecules to improve the selectivity of the adsorption. Besides selectivity, the adsorbent's surface is a second crucial parameter as it determines the adsorption capacity of the bed and thus the reactor size and the process cost. Materials used in adsorption beds are therefore microporous of nature. [31]

Appropriate adsorbents are classified according to adsorption temperature as shown in Figure 3-2: low (<200 °*C*), intermediate (200-400 °*C*) and high (>400 °*C*) temperature adsorbents. Low temperature adsorbents are physisorbent materials which are temperature susceptible and have small CO_2 selectivity because of only weak interactions, e.g. zeolites, activated carbons. At intermediate and high temperatures, only chemisorbents are applied which yield higher selectivity towards CO_2 adsorption, e.g. metal oxides [45].

In this work CaO is used as a chemisorbent because of its potential advantages. It has high CO_2 adsorption performance, fast CO_2 adsorption/desorption kinetics and low material cost. A downside, however, is the difficulty of maintaining a stable capacity because of sintering [46], [47]. Theoretical CO_2 capture capacity of CaO is 17.8 $mol.kg^{-1}$, i.e. the inverse of the molar mass of 56 $g.mol^{-1}$ which assumes that every mole of CaO can adsorb one mole of CO_2. In reality, initial loading capacity between 6-10 $mol.kg^{-1}$ is observed. Moreover, after dozens of cycles this decreases drastically to observed capacities of only 3.5 $mol.kg^{-1}$due to sintering of the sorbent at high temperature [41], [48]. In Figure 3-2 it can be seen that CaO is the preferable adsorbent at high temperatures between 600-900 °*C*.

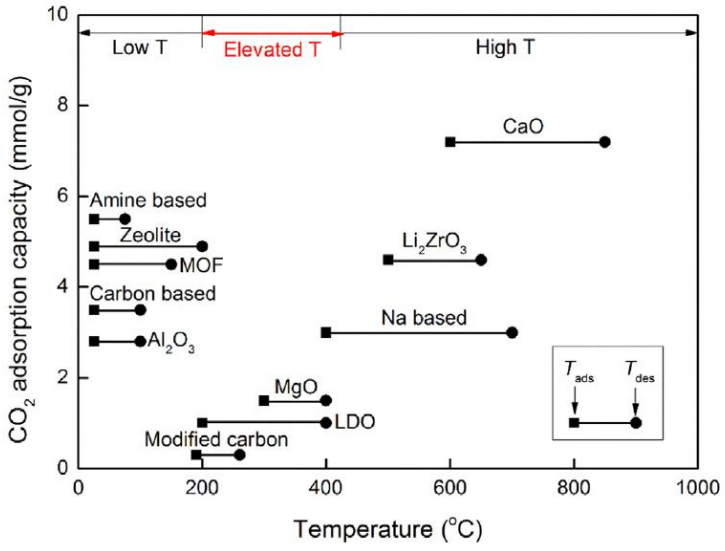

Figure 3-2: Typical CO_2 adsorption capacities of different types of adsorbents and their corresponding operating tempature range. [49]

3.1.3. Adsorption Equilibrium

Adsorption isotherms are used to describe the tendency of components to adsorb on a solid surface. These isotherms represent the amount of adsorbed components per unit of adsorbent (loading) at thermodynamic equilibrium as function of pressure for its corresponding temperature. The driving force of an adsorption process is the departure from this equilibrium and therefore isotherms are crucial in the design of adsorbers [50]. Physical and chemical sorption are exothermic processes, which are more favorable at lower temperatures while desorption is favored at higher temperatures. Different types of isotherms are widely used in literature. In PSA systems, the two most common isotherms are of type I and II as classified by Brunauer, shown in Figure 3-3. Type I is characteristic for a chemisorption phenomenon, where the occupation of all surface sites corresponds to its saturation or for a physisorption process in which all micropores are completely filled. Type II represents a multi-layer behavior or a situation where the sorbate-surface interactions are weaker at lower pressures than sorbate-sorbate interaction. [31]

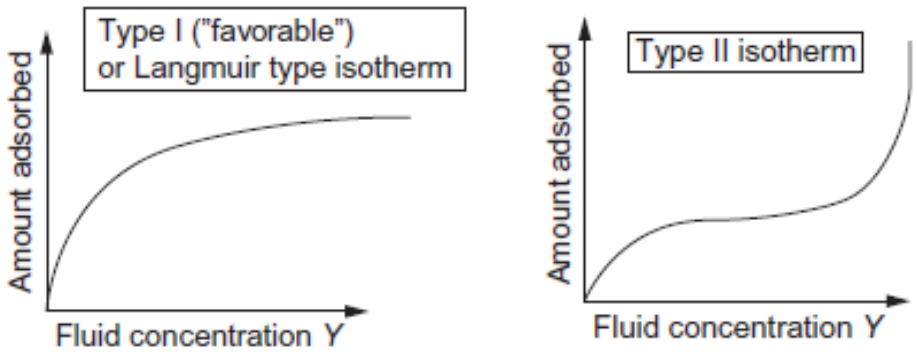

Figure 3-3: Brunauer classification of adsorption isotherms: type I characteristic for chemisorption, type II characteristic for multi-layer physisorption processes. [31]

Several models exist to describe the isotherm of a system. The applicability of the models depends on the operating conditions and system properties. [31]

At low partial pressures, Henry's law for equilibrium relation can be applied, which represents a linear relationship between loading and pressure as shown in Eq. (3.1). Parameter K in Eq. (3.2) represents the adsorption equilibrium factor, obeying Van 't Hoff relation for temperature dependency. Herein, w is the loading in $kmol.kg^{-1}$, P is the partial pressure of a component in *bar*, K is the adsorption equilibrium factor in $kmol.kg^{-1}.bar^{-1}$, ΔH is the adsorption enthalpy in $J.mol^{-1}$, R is the universal gas constant in $J{\cdot}K^{-1}{\cdot}mol^{-1}$ and T is the temperature in *K*.

$$w = K \cdot p \tag{3.1}$$

$$K = K_0 \cdot e^{-\Delta H/R \cdot T} \tag{3.2}$$

At higher concentrations, the equilibrium is not linear with pressure as can be seen in Figure 3-3 in Type I. Langmuir models can be used to describe this asymptotic behavior at higher pressures. They can be used in case chemisorption phenomena are occurring in which adsorbate coverage is limited to one molecular layer only. In the low pressure region it approaches Henry's law, while in the high pressure region it goes to the saturation limit (w_s) as shown in Eq. (3.3). K represents the adsorption equilibrium factor, following Van't Hoff relation for temperature dependency.

$$w = \frac{w_s \cdot K \cdot p}{1 + K \cdot p} \tag{3.3}$$

3.1.4. Adsorption kinetics

The rate of adsorption is generally limited by diffusional limitations. A distinction can be made between homogeneous and heterogeneous adsorbents. Homogeneous adsorbents exhibit a unimodal pore size, while the heterogeneous show a bimodal pore size character. The latter is caused by agglomerating microporous microparticles with in between macropores. As shown in Figure 3-4, three different resistances to mass transfer can be distinguished: external film diffusion, macropore diffusion and micropore diffusion. [31]

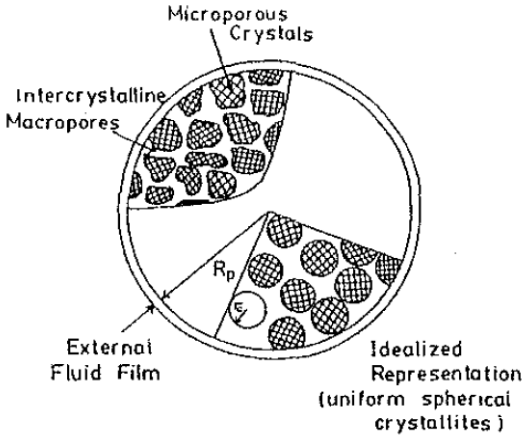

Figure 3-4: Illustrative overview of resistances to mass transfer in heterogeneous adsorbents. [31]

Diffusion in macropores can be described using four different diffusion mechanisms. Large pore diameters yield bulk diffusion as dominant mechanism, while at smaller pore diameters collisions between molecules and pore wall become more important and thus Knudsen

diffusion takes over. Besides that, also Poiseuille diffusion by forced flow takes place and at last surface diffusion through the adsorbed layer can contribute. [31]

On the other hand, micropore diffusion shows strong concentration dependency and is consequently described with Fickian diffusion. Micropore diffusion is an activated process and has a strong temperature dependency following the Arrhenius law. [31]

In modelling the adsorption kinetics, typically a linear driving force model is used as shown in Eq. (3.4). Here the linear driving force, MTC in s^{-1}, is a sum of the previously mentioned mass transfer resistances [31]. For fast kinetics, i.e. without mass transfer limitations, MTC is high.

$$\frac{\delta w}{\delta t} = MTC \cdot (w^* - w) \tag{3.4}$$

As mentioned before, temperature has an influence on adsorption kinetics by either Van't Hoff or Arrhenius relationship. In a PSA operated beds heat effects occur. There are two main heat effects, on one hand heat is generated upon adsorption because of the exothermicity of the reaction and on the other hand the compression inside increases the gas temperature. Besides heat being generated, the opposite of the aforementioned phenomena occur during desorption and depressurization. The relative magnitude of all these temperature changes depend on heats of adsorption and/or reaction, heat capacities and rates of mass and heat transfer. All these parameters are affected by the operating conditions, bed geometry, cycle design, etc. [31]

3.1.5. Operation fundamentals

Every PSA system consists of a sequence of steps for the cyclic operation. This operating cycle is critical for the objective of the process.

The most common elementary steps present in any PSA cycle are shown in Figure 3-5: [31]

I. **Pressurization:** the high pressure feed stream is fed in to the column with the product valve closed, by which the pressure in the column increases.
II. **High pressure feed with raffinate withdrawal**: the high pressure feed continues being fed to the column but the product end is opened, thus the raffinate is withdrawn from the product end.
III. **Pressure equalization**: in a multibed configuration, two or more columns operate cyclically but not at simultaneous steps. When the raffinate product's purity reaches its lower limit, the column's feed end is closed and the high pressure adsorption column is connected to the low pressure desorption column for pressure equalization, thereby

partially pressurizing the low pressure column and depressurizing the high pressure column. This procedure reduces energy requirements to obtain high pressure for the new adsorption cycle in the low pressure column.

IV. **Depressurization/blown-down:** to further depressurize the high pressure column, the column is disconnected from the low pressure column and the extract end is opened, thereby letting depressurization or blown-down happen by which the present gas is vented to atmosphere or storage tanks at lower pressure.

V. **Purge:** part of the raffinate product from a high pressure column in adsorption mode is used as a purge for the low pressure column in desorption mode, consequently decreasing the partial pressure and removing the strongly adsorbed species in the desorbing column. In some cases, a separate inert flow could also be used as purge gas.

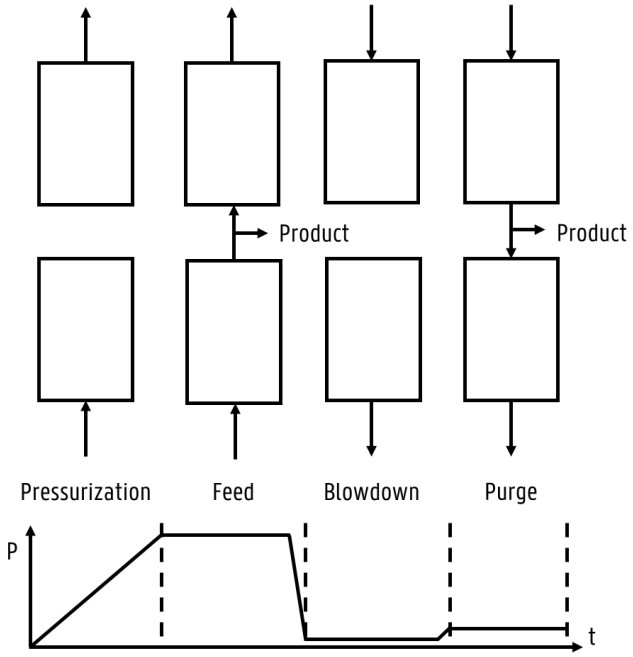

Figure 3-5: Schematic sequence of operations of a pressure swing adsorption cycle including pressurization, feed adsorption, blowdown and purge.

Four operating types can be distinguished based on the nature of adsorption; equilibrium or kinetic limited and the product stream with the goal of having the highest purity; raffinate or extract. In this work all systems are assumed to have no kinetic limitations. Consequently, the operating classes for equilibrium limited systems are the most important. The kinetic limited operating classes, however, still give important insights and are therefore also discussed. [31]

A. Pure raffinate equilibrium limited

A proper analysis of PSA cycles requires understanding how the concentration profile moves during each of these elementary steps. Figure 3-6 shows the gas-phase concentration profiles

in a column that undergoes pressurization, high-pressure adsorption, blown-down and low-pressure desorption in an air separation process. Oxygen is the less strongly adsorbed species in this example. During pressurization (step 4) the gas in the bed is pushed to the closed product end, where it forms a plateau significantly enriched in oxygen, whereas at the beginning the solid is already starting to get saturated with the strongly adsorbed specie and thus lower mole fractions of oxygen are observable. During high-pressure adsorption (step 1), the bed shows increasing saturation with strongly adsorbed species, making the concentration wave move towards to the column's end. During this stage, the high purity oxygen is withdrawn at the product end. When the bed is too saturated to obtain high purity raffinate, the blow-down is initiated which pushes the concentration wave back up the column and pushes all remaining gas out of the column. Thereafter, a low-pressure desorption with part of the raffinate product as purge is performed, flushing the void spaces yielding a clean initial bed again. The blown-down and purge are normally waste gas streams or part of the raffinate product rich in less strongly adsorbed species. [31]

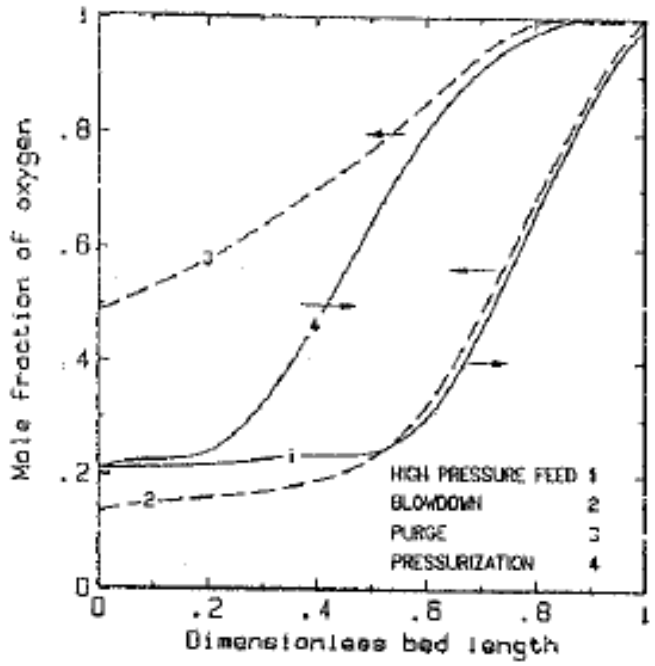

Figure 3-6: Illustrative figure of moving oxygen concentration profiles of less strongly adsorbed species during a PSA cycle with pressurization, high pressure feed, blown-down and purge. [31]

Regeneration counter-current to the feed direction prevents retention of strongly adsorbed species at the product end, consequently reducing the purge requirement. Increasing the purge will improve the product purity, but also lower the product recovery. Consequently, a optimum between both has to be found for every specific design. The loss of raffinate product as purge depends on the operating pressure difference of the adsorption and desorption mode. A bigger difference in pressure will result in a small fraction of the raffinate needed to obtain a

regenerated bed, because of lower generated partial pressures of the adsorbed specie in the bed. Improvements in raffinate losses and energy requirements can be found by using blowdown gas for purging other beds and using multiple beds with a sequence of pressure equalization steps respectively. In general multiple bed system show greater performance at the cost of more complex process schemes. [31]

B. Pure extract equilibrium limited

In case the pure extract is of interest, a vacuum swing cycle can be used. Here, a co-current depressurization is performed, thereby removing the raffinate product left in the void spaces and retaining the more strongly adsorbed species at the product end. Thereafter, a vacuum regeneration for producing the extract product is performed. The vacuum is only needed in case very strongly adsorbed species are present, else atmospheric pressure can be used. [31]

In the pressure swing operation of this work, first a mixture of CO, CO_2, H_2 and H_2O is fed into a high pressure bed of 15 bar. The reactions occurring produce mainly H_2O which will leave the bed together with the unreacted gases as the raffinate product, i.e. as steam. Near to the full conversion of the solids, the feed will breakthrough, and therefore the product end should be closed at this moment. Further in the cycle, the pressure will be decreased to 1 atm and a CO/CO_2 mixture will be produced as a main product that leaves the column as extract. Therefore, a co-current depressurization is preferred to obtain a high purity extract in this work. [31]

C. Kinetically limited

The cycles so far discussed are for separation based on equilibrium selectivity. For kinetically controlled separation on the other hand, the contact time is critical. The idea is to exploit the difference in diffusion rates of the species and consequently the contact time should be chosen such that it is short enough to avoid equilibrium and long enough to have significant uptake. Therefore the duration of the adsorption and desorption steps are crucial. The aforementioned purge step with raffinate during desorption would lead to unwanted diffusing raffinate in the bed, leading to decreased capacity for the fast diffusing specie. This can be circumvented by the use of vacuum desorption or a self-purging cycle. In both cases there is no need of a purge, consequently yielding a higher raffinate recovery. [31]

After the blow-down step, the fast and slow diffusing species are still present in the bed. By closing the bed at product end and leaving it for a period of time, the fast diffusing specie will come out first, followed by the slow diffusing specie. Self-purging is, however, not always effective. In case the slow diffusing species are not able to come out first, they are blocking the fast diffusing species inside the void volumes to come out. Consequently, an increased

contamination in the raffinate product with fast diffusion specie can be seen. Therefore there is a lower limit of slow diffusing species below which self-purging becomes ineffective. [31]

D. Pressure swing operation of the combined chemical looping reactor

The operation of the RWGS chemical looping reactor follows the operating fundamentals of PSA systems. It will consist of a pressurization step in which the reactor pressure is increased to 15 *bar* with high pressure feed gas. Subsequently, the 'reducer' regime step occurs at high pressure, where the high pressure feed is fed and the raffinate is produced. Thereafter a depressurization step occurs, reducing the pressure to 1 *bar* by closing the feed valve and venting the reactor co-currently. At last, the 'oxidizer' regime takes place at this low pressure in which a self-purge takes place by CO_2 release and conversion to CO. After the cycle is completed, the high pressure feed is introduced again to restart the cycle with the pressurization step.

A purge gas might be required based on the operating behavior of the reactor, especially on the calcination reaction in the 'oxidizer' regime. It is important that enough adsorbent is available for CO_2 capture and therefore an additional purge step can be required to fully regenerate the Ca-absorbent. Also, depending on the self-purging time, a purge step may be required to decrease the total cycle time.

3.1.6. State-of-the-art high temperature pressure swing adsorption

Pressure swing adsorption (PSA) shows resemblances with this work because of the alternating high and low pressure during the reducer and oxidizer regime step respectively. The main difference with common PSA technologies and the pressure swing chemical looping process is that in the former uses low temperatures while the latter requires higher temperatures up to 900 °*C*. PSA is mostly known for hydrogen purification as a separation step after steam methane reforming. These PSA systems work at temperatures of 20-40 °*C* and adsorption pressures of 4-30 *bar* and desorption pressures around atmospheric pressure [51], [52]. Consequently, a review on state-of-the-art PSA systems at high temperature is performed.

PSA systems at higher temperature are referred to as elevated temperature PSA (ET-PSA). There is interest in working at higher temperatures because of energy efficiency reasons. For example, outlet gases of a WGS reactor at 200-400 °*C* contain CO_2 that needs to be separated. Conventional separation uses low temperature PSA system and thus the hot outlet gas has to be cooled down first [49], [53]. Avoiding this cool down step by using ET-PSA can increase the

energy efficiency of the cycle. Zhu et al. [53] performed ET-PSA for such a system with physisorbents at 200-450 °*C* and 35 *bar* for adsorption and with a steam purge at 1 *bar* for regeneration. Furthermore, Liu et al. [54] propose a similar pressure swing system for CO_2 capture from flue gasses at temperatures of 200-300 °*C* with physisorbents. Especially for Ca-L there has been interest in using pressure swing operation for heat integration possibilities, as mentioned earlier. Butler et al. [55] performed experiments in a pressurized thermogravimetric analyzer for CO_2 capture with CaO using a pressure cycling approach. At a constant temperature of 1000 °*C*, carbonation was performed up to 21 *bar* and calcination at atmospheric pressure with a continuous CO_2 stream. Their results show higher solid utilization compared to temperature swing or purge regeneration approach. Moreover, fast depressurization was shown to be beneficial for desorption. Yin et al. [33] performed CO_2 capture with CaO for operating temperatures between 650 and 850 °*C* using a pressure swing approach. They used steam as purge for the regeneration of the sorbent.

It can be concluded that there is interest for ET-PSA systems, but currently they are still under development. In addition, pressure swing cycles for CO_2 adsorption in PBR's exist, but almost of the technologies use a purge step for the regeneration of the sorbent, thereby diluting the CO_2 stream. The main difference is that CO_2 is not a product of interest, it is only separated as a purification step for the main product. Therefore, it is not seen as a valuable component and thus not produced in high purity. While, in this work, high purity CO_2 is required as the main source to produce CO. This means that the pressure swing operation by self-purging of the sorbent used in this work is unique in its kind.

3.1.7. Pressure swing operation modelling

Pressure swing adsorption processes are modelled in either self-constructed programming and numeric computing platforms such as Matlab© and Python© or they are modelled in a flowsheet simulator program such as Aspen Adsorption©. The former requires the user to provide all governing equations to model the beds, while the latter provides a full interactive and comprehensive user-interface that can easily be used for design, optimization and analysis of adsorption processes. Aspen Adsorption© is part of the AspenOne® software collection and contrary to AspenPlus©, it is able to make dynamic simulations as required in this work.

Chapter 4

Literature review: Chemical looping reaction kinetics

An preliminary literature review on reaction kinetics data for the full super-dry reforming process was performed by Claus [8] to design a steady state process model based on kinetics. However, this work focuses on the dynamic behavior of the combined chemical looping concept for the reverse water gas shift reaction after the dry reforming reaction. Even though the reaction kinetic were not used in the dynamic simulation, a literature review was performed to prepare an up-to-date summary that will facilitate future works focused in kinetic modelling. In this section, an overview of the findings from Claus and this work is presented. The reaction kinetics found in literature should be viable for the phases and conditions used in the SDR process. First a summary of the process reactions and conditions is given. Thereafter, kinetic models from literature are presented and compared.

4.1. Combined chemical looping overview

The combined chemical looping process for enhanced RWGS reaction can be split up in two reactive systems. On one hand, there is a redox chemical looping system for the RWGS reaction with Fe-based oxides as OSM. Reaction kinetics for the reduction of FeO by CO and H_2 in the reducer regime are required as shown by Eqs. (4.1) and (4.2), respectively. Besides that, also reaction kinetics for the oxidation of Fe by CO_2 in the oxidizer regime are required, represented by the reverse reaction of Eq. (4.1).

$$FeO + CO \leftrightarrow Fe + CO_2 \quad (4.1)$$

$$FeO + H_2 \leftrightarrow Fe + H_2O \quad (4.2)$$

On the other hand, there is a Ca-looping system to enhance the RWGS reaction by capturing CO_2 in-situ and subsequently releasing it. Reaction kinetics for the carbonation reaction, shown by the forward reaction of Eq. (4.3) and for the calcination reaction, shown by the reverse reaction of Eq. (4.3) are required.

$$CaO + CO_2 \leftrightarrow CaCO_3 \quad (4.3)$$

A full thermodynamic equilibrium and kinetic steady-state process simulation is performed in the work of Claus to determine the operating conditions for the SDR process [8]. In this

simulation, a CH4 and CO2 mixture is fed to a dry reformer, and the reformed gas is fed to the chemical looping section. The operating conditions in the chemical looping PBR during the reducer regime are determined to be 15 *bar* and 828 °*C*, while 1 *bar* and 828 °*C* are the process conditions for the oxidizer regime. These conditions were used to evaluate the viability of the kinetic data from literature for the calcium and iron system.

4.1.1. Calcium looping system kinetics

CO_2 capture with CaO solids is a chemisorption process. The carbonation and calcination reaction are non-catalytic gas-solid reactions [47], [41]. Literature shows great variety of models applied for the carbonation and calcination reactions, however, the following key take-aways are recognized by them. First, it is observed that two regimes can be distinguished during the carbonation reaction, namely a fast chemical reaction controlled stage (surface chemical reaction) and a slow product layer diffusion controlled stage due to $CaCO_3$ layer formation as is shown in Figure 4-1 [47], [56]–[59]. Therefore, in operation mode the calcium looping system is preferably only making use of the first stage of CO_2 capture. After a degree of conversion of 60% the reaction rate is observed to drop because of the diffusion process due to clogging of the solid pores [56]. Thus, it is assumed that the reaction stays within the first fast regime. Secondly, a significant decrease in sorption capacity is observed after dozen of cycles due to sintering and solid breakdown [41], [48], [58]. Empirical formulas for loss in sorption capacity are proposed in literature, but will not be discussed.

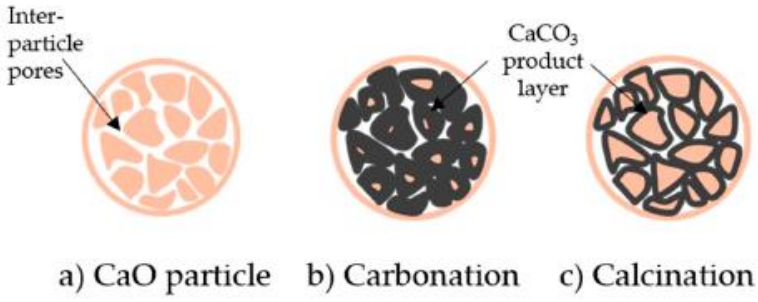

Figure 4-1: Schematic representation of CaO particle undergoing carbonation-calcination cycling reactions. [59]

For modelling carbonation/calcination reactions, various particle models exist for describing the non-catalytic gas-solid reaction in which a structural transformation takes place. These models describe the change of conversion as a function of the conversion and assumed structural transformation of the solid reactant. The grain model (GM) considers that the solid particles as composed of spherical grains, with voids in between to represent the porosity. On the other hand, random pore models (RPM) represent the porosity as cylindrical pores randomly interconnected inside the particle. For the calcination, an uniform conversion model

(UCM) could also be used. This model assumes that the conversion depends on the BET surface area of the undecomposed material and the rate of decomposition [52], [57], [59].

4.1.1.1. Carbonation

Claus [8] concluded that three scientific works were suitable to simulate the carbonation reaction in this work; being these the work from Bhatia and Perlmutter [58], Lemonidou et al. [61] and Sun et al. [62]. Additionally, an updated work of Lemonidou et al. [57] is added on Table 4-1, where a summary is presented.

Table 4-1: Carbonation kinetic data from different authors suitable for the operating conditions in this work.

Temperature [°C]	**Model**	**A** [$m^4kmol^{-1}s^{-1}$]	**E_a** [$kJ.mol^{-1}$]	**Ref.**
550-725	RPM	/	0	Bhatia and Perlmutter [58]
850	RPM	$6.9*10^{-6}$	20	Lemonidou et al. [61]
550-850	GM	$1.67 \cdot 10^{-3}$	29	Sun et al. [62]
670-820	RPM L-H	$6.08 \cdot 10^{-6}$	22.1	Lemonidou et al. [57]

Bhatia and Perlmutter [58] used a RPM model and concluded that the carbonation was a non-activated reaction. Their experiments show that there is no CO_2 partial pressure dependency above 0.01 bar. However, later work of Lemonidou et al. [61] rejected a non-activated carbonation reaction using the same RPM model. The activated process is confirmed by multiple other authors as well. Sun et al. [62] used a GM model and obtained an activated process as well. Similar to the work of Bhattia and Perlmutter [58], they found no CO_2 partial pressure dependency of the carbonation rate above 0.1 *bar*. Grasa et al. [37] observed, however, that the CO_2 partial pressure dependency stops at partial pressures higher than 1 *bar* as the CaO surface gets saturated

In a recent study from Lemonidou et al. [57], they modified their previous RPM model taking in to account inert phases present in CaO. A mechanistic Langmuir-Hinshelwood model shows that there a linear dependency with partial pressure of CO_2 in temperature ranges of 670-820 °*C* and partial pressure of CO_2 up to 1.2 *atm*. This is in contrast with what Bhatia and Perlmutter and Sun et al. found. They also propose a two-step Langmuir-Hinshelwood mechanism in which the sorption of CO_2 is rate determining. Their model is proposed as a general model for the basis of Ca-L technology. This led to the carbonation rate in Eq. (4.4) with a pre-exponential factor of 6.08E-6 $m^4kmol^{-1}s^{-1}$ and an activation energy of 22.1 $kJ.mol^{-1}$.

$$r = 6.08 \cdot 10^{-6}\, exp\left(-\frac{22\,100}{RT}\right)\left(\frac{P_{CO2}}{P_{CO2,e}} - 1\right) \tag{4.4}$$

Previous results show that there is no real agreement between all different authors for the carbonation reaction, certainly on the CO_2 partial pressure dependency. The CO_2 partial pressures of 3.72 *bar* in this work exceeds all previously mentioned transition points from first to zero order dependency. It is therefore very important that the CO_2 partial pressure dependency is taken in to account correctly to avoid either over- or underestimation. Consequently, it is recommended that experiments at high CO_2 partial pressures are performed to get the correct carbonation reaction mechanism.

4.1.1.2. Calcination

Claus [8] based his calcination kinetics on the work of Lemonidou et al. [61], which is based on the work of Borgwardt et al. [63]. Additionally, a more recent work of Lemonidou et al. [52] is further elaborated up on. Table 4-2 lists the kinetic data from the aforementioned authors together with the corresponding conditions of the kinetic study.

Table 4-2: Calcination kinetic data from different authors suitable for operating conditions in this work. units [ms^{-1}]*

Temperature [°C]	**Model**	**A** [$molm^{-2}s^{-1}$]	**E_a** [$kJmol^{-1}$]	**Ref.**
475-1000	UCM	$51 \cdot 10^6$	205	Borgwardt et al. [63]
950	RPM	5.5*	205	Lemonidou et al. [61]
825-885	UCM L-H	$18.9 \cdot 10^6$	210	Lemonidou et al. [52]

Borgwardt et al. [63] performed calcination experiments over a range of high temperature and high rates. Their findings for the activation energy of the calcination reaction using a UCM model of 205 *kJ.mol*$^{-1}$ is widely accepted and often used as comparison in other works. Later Lemonidou et al. [61] used a RPM model to describe the evolution of the solid structure combined with the aforementioned activation energy of Borgwardt et al. [63] to describe the calcination kinetics.

In the latest work of Lemonidou et al. [52], RPM, GM and UCM models are compared over a temperature range of 825-885 °C and CO_2 partial pressures of 0.1-0.6 *bar*. They concluded that the UCM model combined with a mechanistic Langmuir-Hinshelwood model described the calcination reaction the best. The calcination rate is found to be non-linearly dependent on partial pressure of CO_2 and results in the format shown by Eqs. (4.5), (4.6) and (4.7) with the corresponding value of the parameters in Table 4-3. Their activation energy is in accordance with the widely accepted value of Borgwardt et al. [63].

$$r = A \cdot (1-\theta)\, exp\left(-\frac{E_a}{RT}\right)\left(1-\frac{P_{CO2}}{P_{CO2,e}}\right) \quad (4.5)$$

$$\theta = \frac{K \cdot P_{CO2}}{1 + K \cdot P_{CO2}} \quad (4.6)$$

$$K = K_0 \cdot \left(\frac{-\Delta H}{R \cdot T}\right) \quad (4.7)$$

Table 4-3: Experimental fitted values used for calcination reaction Eq. (4.5).

Parameter	Fitted value by Lemonidou et al. [52]
E_a [kJmol^{-1}]	210
A [molm^{-2}s^{-1}]	$18.9 \cdot 10^6$
ΔH_{ads} [kJmol^{-1}]	-101
K_o [kPa^{-1}]	$1.38 \cdot 10^{-6}$

It can be said that there is no real agreement between all findings in scientific works. However, the extension with the works of Lemonidou et al. for the carbonation [57] and calcination [52] reactions are the latest scientific works that present generalized models that could possibly be used in the modelling of Ca-L.

4.1.2. RWGS iron looping kinetics

In literature, there is no common agreement on the kinetics of all redox reactions. There is no unified model proposed since all kinetic studies are performed in different operating conditions, with other objectives and with other materials, morphology, etc. This makes the comparison of the proposed models difficult. Therefore no definite conclusion can be drawn on which scientific work's kinetic model suits this work the best. The extensive literature search in the work of Claus [8] showed the great differences found in activation energies for all reactions. No further additions are found that are able to describe the iron redox reactions in this work and thus the main conclusions of the work of Claus [8] are shown here.

4.1.2.1. Reduction by CO and H_2

Iron exhibits three main oxides, namely FeO (+II) known as wüstite, Fe_3O_4 (+II,+III) known as magnetite and Fe_2O_3 (+III) as hematite. In this work only the reduction of FeO to Fe is considered, as Claus [8] determined that these oxidation states yield the highest possible CO purity. At the high temperatures, these oxidation states will only be present due to the composition in the reactor. In the work of Claus [8] it is concluded that the reaction kinetics for

the reduction of FeO to Fe with both H_2 and CO as reducing agents is best described by scientific work of Liu et al. [64] for the conditions in this work. They found the reduction reactions to have two distinct stages; increasing rate during nucleation and growth stage up to a conversion of 20% and decrease rate during diffusion controlled stage up to full conversion. A RPM model is found to adequately describe both regimes, resulting in kinetic expressions for both reduction by H_2 and CO presented in the work of Claus [8]. The reduction by H_2 is found to be substantially faster than with CO during the first regime, whereas the resistance to diffusion is comparable for both during the second regime. In addition, it is found that there is no synergy between the two reducing agents and the individual rate expressions can be summed to obtain the total rate of reduction.

4.1.2.2. Oxidation by CO_2

In the work of Claus [8] it is concluded that the work of Buelens et al. [65] and Wenzel et al. [16] describe the oxidation by CO_2 to the best extent. Experimental results performed by Buelens et al. [65] show that oxidation of Fe to Fe_3O_4 occurs without intermediate oxides. The scientific work of Wenzel et al. [16] also observed this and mention that the oxidation of Fe to FeO and FeO to Fe_3O_4 proceed at a very similar rate. The former work uses a shrinking core model, whereas the latter work uses a geometrical contraction model to describe the change of conversion by structural transformation. The work of Buelens et al. [65] obtained an activation energy of 108.4 $kJ.mol^{-1}$ as shown in Table 4-4 which is in accordance with the obtained activation energy in the work of Wenzel et al. [16]. The latter assumed that kinetics are controlled by a diffusion controlled-stage. The work of Wenzel et al. [16] appears the show the most resemblances with this work as it is presented for RWGS chemical looping and is therefore presented in the work of Claus [8].

Table 4-4: Activation energy of oxidation step obtained by corresponding author for shown material and model assumptions. RDS = rate determining step in kinetic model.

Material	**Ea** [$kJ.mol^{-1}$]	**Model**	**RDS**	**Ref.**
Fe	108.4	Shrinking core	Diffusion	Buelens et al. [65]
Fe	112	RPM	Diffusion	Wenzel et al. [16]

Chapter 5

Methodology and modelling procedures: Available simulation programs

In this work, two main programs are used, namely; Aspen Adsorption© for the dynamic simulation of the packed bed and FactSage© as thermochemical database. Besides these, also FORTRAN is used as programming language for the external user procedures linked to Aspen Adsorption© and Microsoft Excel© as post-processing tool.

5.1. Aspen Adsorption® Simulation Program

Aspen Adsorption® is selected as the simulation program for this work. It is a comprehensive flowsheet simulator with the ultimate aim to improve design, reduce capital and operating costs of adsorption processes [50]. It is able to simulate gas phase processes with adsorption only, or sorption enhanced processes where both reaction and adsorption reactions occur simultaneously. Typical simulated processes are PSA/TSA, air separation and hydrogen purification processes. [42], [66]

The program is determined to be the right simulation software for this work because of the resemblances, i.e. packed bed reactor where the RWGS reaction takes place and CO_2 is adsorbed/desorbed.

The program uses a set of partial differential equations, ordinary differential equations and algebraic equations that represent mass, momentum and energy balances, kinetic and equilibrium models together with the appropriate solver, initial and boundary conditions to fully describe adsorption processes. [66]

This modelling approach provides a better understanding of the process behavior without performing and analyzing several experiments. The use of modelling and simulation prior to experimental and commercial implementation of a technology is crucial for the design of a complex process such the combined chemical looping process in this work. The obtained model in Aspen Adsorption© is used for understanding the dynamic behavior of the system and can be used for designing an experimental set-up and method.

5.1.1. Model assumptions

Aspen Adsorption© model program can be used for gas processes with adsorption only, or where both reaction and adsorption occur simultaneously. The packed bed is modelled with several assumptions that will be listed here:

- **Bed type**

The bed is modelled as a vertical bed with one-dimensional discretization. Spatial derivates are evaluated in axial (flow) direction only.

- **Material and momentum balances**

The material balance assumption is selected so the model is as simple as possible, therefore only convection is taken into account, thus no axial nor radial dispersive terms are considered. This indicates a full radial mixing along the reactor and plug flow behavior. The momentum balance assumes either no pressure drop in the column or a pressure drop according to the laminar and turbulent flow momentum balances.

- **Kinetics**

A kinetic model for mass transfer can be chosen and is assumed to be based on the solid film model with a simple linear form and lumped overall resistance. Mass transfer coefficients are assumed to be constant throughout the simulation.

- **Isotherms**

Several adsorption isotherm equations are provided by the user interface, such as Langmuir, Freundlich and B.E.T. isotherms. The isotherm dependency can be selected to be concentration or pressure dependent. Besides that, the user can also specify an user procedure where a specific isotherm expression is developed in a separate FORTRAN code. In this work, the latter is chosen which will be explained further on.

- **Energy balance**

The energy balance inside the bed can be assumed to be either isothermal or non-isothermal. For the latter, the energy balance includes terms of thermal conductivity for gas and solid phase, compression effects, gas-solid heat transfer, heat of adsorption and heat of exchange with environment. The purpose of this work is to investigate the dynamic behavior of the combined chemical looping concept based on thermodynamic equilibria. Therefore, as a starting point, isothermal operation is assumed. Although the exo- and endothermicity of the reducer and oxidizer step, respectively, and compression and expansion will lead to temperature variations in the bed, this will complicate understanding the basic behavior of the

system and is thus not taken in to account in this work. In a later stage, the non-isothermal behavior can be evaluated as this is an important factor in the design to obtain isothermal operation by using external heat, cooling sources or making the process autothermal.

- **Reactions**

Reactions can be implemented in the packed bed with a choice between homogeneous reactions, heterogeneous reactions or a combination thereof. The heterogeneous reaction resembles catalyzed reactions with a solid. In this case two distinct solid phases can be present, being the adsorbent and the catalyst. Solid reactants can also be present, leaving the option to let them being formed by the heterogenous reaction or let them represent catalytically active sites being deactivated or reactivated. The former representation of the solid reactants can possibly be used to simulate the calcination/carbonation reactions and the latter representation for the reduction and oxidation reactions of iron-oxide and iron respectively. However, in this work the gas-solid reactions are not represented by the reaction module, but by the adsorption isotherms.

- **Gas phase**

The non-ideal behavior of the gas phase can be taken into account by using a compressibility factor. However, in this work the gas phase is assumed to behave ideally.

- **Reversibility**

All components in the simulation make use of a reversible model. Herein, all valves are modelled using reversible flow setter option in which the pressure difference dictates the direction of the flow. And all tank voids are modelled using a reversible pressure setter option by which the flow dictates the pressure difference. In this configuration it is possible to make use of counter- and co-current stream configurations.

- **Discretization method**

The default discretization method, being the Upwind Difference Scheme 1 (UDS1) has been chosen as it is the recommended and preferred option because it is reasonable accurate and requires the least simulation time. Simulation accuracy can be improved by increasing the number of discretization nodes. UDS1 is a first-order upwind differencing scheme, based on a first-order Taylor expansion as shown in Eq. (5.1).

$$\frac{\delta \Gamma_i}{\delta z} = \frac{\Gamma_i - \Gamma_{i-1}}{\Delta z} \tag{5.1}$$

5.1.2. Model equations

Aspen Adsorption© makes use of several governing partial differential equation to describe the plug flow behavior of the packed bed. The following model equations are solved for each node in the packed bed using the UDS1 discretization method. [50]

- **Material balance**

An adsorption column is essentially a packed bed and therefore the flow pattern can be described by an axial dispersed plug flow model. Material balance assumption is chosen to be as simple as possible, therefore only convection is taken into account with no axial or radial dispersive terms. The mass balance inside the column assumes no reactions that take place. The respective component material balance for the gas phase is given in Eq. (5.2), in which c_i is the gas phase concentration in *kmol.m*$^{-3}$, v_g is the gas phase superficial velocity in *m.s*$^{-1}$, z is the axial distance in *m*, ε_B is the bed porosity, ρ_s is the solid density in *kg.m*$^{-3}$ and w_i is the solid loading in *kmol.kg*$^{-1}$.

$$\frac{\delta(c_i v_g)}{\delta z} + \varepsilon_B \frac{\delta c_i}{\delta t} + \rho_s \frac{w_i}{\delta t} = 0 \tag{5.2}$$

- **Kinetic model**

A linear driving force model based on the solid film for mass transfer has been chosen, according to other authors [31] [39] [40] and shown in Eq. (5.3). It is based on the assumption that the driving force for mass transfer of the gas components to the solid surface is a linear function of the difference in equilibrium solid-phase loading (w_i^*) in *kmol.kg*$^{-1}$ and actual solid-phase loading (w_i). The linear driving force is represented by MTC in *s*$^{-1}$.

$$\frac{\delta w_i}{\delta t} = MTC(w_i^* - w_i) \tag{5.3}$$

- **Isotherm**

The isotherms describe the amount of each component adsorbed on the solid at thermodynamic equilibrium. The isotherms in this work are supplied by self-coded isotherm relationships using a FORTRAN subroutine *pUser_g_Isotherm_P* that are further discussed in Chapter 6. The equilibrium solid-phase loading w_i^* in *kmol.kg*$^{-1}$ is a function of temperature T

in K, total pressure P in *bar* and molar fractions of the gas components y_i as shown in Eq. (5.4).

$$w_i^* = f(T, P, y_i) \tag{5.4}$$

- **Gas model**

The gas model defines the relationship between pressure, temperature and molar density and is given by Eq. (5.5). Herein P is the total pressure in bar, y_i is the mole fraction of component i, Z is the compressibility factor, R is the universal gas constant in *bar.m^3.kmol^{-1}.K^{-1}*, T_g is the gas temperature in *K* and c_i the molar concentration of component I in *kmol.m^{-3}* . In this work an ideal gas phase is assumed and therefore the compressibility factor is equal to 1.

$$Py_i = ZRT_g c_i \tag{5.5}$$

- **Energy balance**

There is no need for an energy balance in this work because it is assumed to work at isothermal conditions. The gas temperature and the solid temperature are held constant and equal.

- **Momentum balance**

The momentum balance of a packed bed is represented by the Ergun equation as shown in Eq. (5.6). This model combines the description of change in pressure according to the Karman-Kozeny equation for laminar flow and Burke-Plummer equation for turbulent flow. The velocity and pressure gradient are related through this momentum balance. P is the total pressure in *bar*, μ the dynamic viscosity of the gas phase *N.s.m^{-2}*, ε_i the interparticle voidage, r_p the particle radius in *m*, ψ the sphericity, v_g the superficial gas velocity in *m.s^{-1}* , M gas molar mass in *kmol.kg^{-1}* and ρ_g the molar gas phase density in *kmol.m^{-3}*.

$$\frac{\delta P}{\delta z} = 150\frac{\mu(1-\varepsilon_i)^2}{{\varepsilon_i}^3\left(2r_p\psi\right)^2}v_g + 1.75M\rho_g\frac{(1-\varepsilon_i)}{{\varepsilon_i}^3 2r_p\psi}{v_g}^2 \tag{5.6}$$

- **Valve equation**

Valves are modelled as simple linear valves in which the flowrate through the valve is expressed as a linear function of the pressure drop across the valve as shown in Eq. (5.7) in which F is the flowrate in *kmol.s^{-1}*, Cv is the linear valve constant in *kmol.bar^{-1}.s^{-1}* and ΔP is the

pressure drop across the valve in *bar*. This equation inherently assumes reversibility of the flow, namely depending on the positive or negative ΔP the flow is in forward or reverse direction, respectively.

$$F = Cv\Delta P \tag{5.7}$$

5.2. FactSage©

FactSage© version 8.0 is used as a tool for thermochemical database in this work. The software allows the calculation of thermodynamic equilibria at varying conditions for the gas and solid components present in this work.

The *Reaction* module is used for calculating changes in enthalpy and Gibbs free energy for the chemical reactions. The former property is used to obtain the heat of reaction and the latter to obtain the Gibbs free energy of reaction as function of temperature $\Delta G_r(T)$ by which equilibrium constants can be constructed based on Eq. (5.8). [67]

$$K_{eq} = exp\left(\frac{-\Delta G_r(T)}{RT}\right) \tag{5.8}$$

The *Equilib* module is used to calculate multiphase and multicomponent equilibria using a Gibbs Energy Minimization method. Herein, the concentration of chemical species react completely or partially to reach a state of chemical equilibrium.

Chapter 6

Methodology and modelling procedures: Equilibrium simulations

In this chapter the methodology of the performed simulations is explained. As aforementioned, the kinetic study in Chapter 4 showed that great variety exists between authors for all kinetic data and thus that there is no common agreement on a generalized kinetic model for all reactions. Moreover, as the purpose of this work is a conceptual investigation of the reactor dynamics, rather than verifying the kinetic data at proposed conditions, a thermodynamic approach was followed. Therefore, in this work a conceptual investigation is performed based on the thermodynamic equilibrium of the reactions.

The following sections deal with the approach for simulating the dynamic equilibria of the reactions using isothermal equations. Thereafter, the simulation input and configuration of the Aspen Adsorption© simulator flowsheet is elaborated upon.

6.1. Equilibrium based approach

In the reactor, it is assumed that the gas phase molecules are in equilibrium with the solids. That means that in total three equilibria of the aforementioned reactions exist, i.e. for the redox reactions between Fe and FeO by H_2-H_2O and by CO-CO_2, together representing the WGS equilibrium, and the sorption/desorption of CO_2 by CaO/$CaCO_3$. The specific thermodynamics of the subsystems and the approach to implement these in Aspen Adsorption© are elaborated upon.

6.1.1. Thermodynamic equilibrium of system

In order to get acquainted with the two solid systems of this work, a thermodynamic analysis is performed using FactSage©. The resulting thermodynamic expressions are crucial for this work as they form the basis for the equilibrium simulations.

6.1.1.1. Iron-reverse water gas shift equilibrium

In this work it is assumed that iron is present in its metallic form, i.e. Fe and in only one of its oxides, FeO. The equilibrium constants for the reduction of FeO with CO and H_2 can be expressed as presented in Eqs. (6.1) and (6.2) respectively. Herein, $P_{CO_2,eq}$, $P_{CO,eq}$, $P_{H_2O,eq}$ and

$P_{H_{2,eq}}$ are the equilibrium partial pressures of the corresponding components in the gas phase. $\Delta G^{\circ}_{r,1}(T)$ and $\Delta G^{\circ}_{r,2}(T)$ represent the standard Gibbs free energy of the reduction of FeO by CO and H_2, respectively, as function of temperature in *Jmol^{-1}*. *R* is the universal gas constant equal to 8.31 *K.mol^{-1}K^{-1}* and T is the gas and solid temperature in *K*.

$$K_{CO_2/CO} = \frac{P_{CO_2,eq}}{P_{CO,eq}} = exp\left(\frac{-\Delta G^{\circ}_{r,1}(T)}{RT}\right) \quad (6.1)$$

$$K_{H_2O/H_2} = \frac{P_{H_2O,eq}}{P_{H_{2,eq}}} = exp\left(\frac{-\Delta G^{\circ}_{r,2}(T)}{RT}\right) \quad (6.2)$$

The temperature dependency of the Gibbs free energy can be represented by Shomate equations retrieved from FactSage© for every component in the system and are represented in Table 6-1. The equation are constructed using the format shown in Eq. (6.3).

$$G^{\circ}_i(T) = \sum A_i X_i \quad (6.3)$$

Table 6-1: Coefficients of Shomate equations for calculation of the standard Gibbs free energy of components for the iron system retrieved from FactSage©.

H_2		**H_2O**		**CO**		**CO_2**		**FeO**		**Fe**	
Ai	**X_i**	**Ai**	**X_i**	**Ai**	**X_i**	**Ai**	**X_i**	**Ai**	**X_i**	**Ai**	**X_i**
-13779.8231		152152.281		-203680.536		-415579		-322148		1225.7	
-17.7153374	T	164.817017	T	609.464125	T	642.7679	T	-330.687	T	124.134	T
-1.54E-03	T^2	-8.05E-05	T^2	3.12E-03	T^2	2.37E-03	T^2	-1.53E-02	T^2	-4.40E-03	T^2
147589	T^{-1}	-12075583.2	T^{-1}	770627.667	T^{-1}	20124.52	T^{-1}	1266650	T^{-1}	77358.5	T^{-1}
-2.38E-07	T^3	-83128.2757	lnT	32063.3157	lnT	-6993.15	$T^{0.5}$	6003.6	$T^{0.5}$	-5.89E-08	T^3
779.444975	$T^{0.5}$	5947.37003	$T^{0.5}$	-10357.019	$T^{0.5}$	11004.74	lnT	18.02447	TlnT	-23.5143	TlnT
-19.8256305	TlnT	-53.1457895	TlnT	-90.7535842	TlnT	-103.345	TlnT			-427.063	G

The Gibbs free energy can then be calculated using Eq. (6.4) to be used in Eqs. (6.1) and (6.2). The corresponding equilibrium constants are regressed as function of temperature in Excel to obtain Eq. (6.5) and Eq. (6.6) that can be used in a easier manner.

$$\Delta G_r(T) = \sum G^{\circ}_{product}(T) - \sum G^{\circ}_{reactant}(T) \quad (6.4)$$

$$K_{CO_2/CO} = \frac{P_{CO_2,eq}}{P_{CO,eq}} = 10^{\left(-1.0188+\frac{792.36}{T}\right)} \quad (6.5)$$

$$K_{H_2O/H_2} = \frac{P_{H_2O,eq}}{P_{H_2,eq}} = 10^{\left(0.4112--\frac{781.04}{T}\right)} \quad (6.6)$$

It can be seen that the equilibrium constant of the reduction of FeO with CO decreases with increasing temperature due to the exothermicity of the reaction ($\Delta H^0_{298K} = -18\, kJmol^{-1}_{CO}$),

whereas equilibrium constant for the reduction of FeO with H_2 increases with increasing temperature because of the endothermicity of the reaction ($\Delta H^0_{298K} = 16\ kJmol^{-1}_{H2}$) as shown by the van't Hoff relationship.

The equilibrium of the WGS reaction is described by the division of $K_{CO_2/CO}$ by K_{H_2O/H_2} which will determine the equilibrium composition of the mixture when all components are present.

6.1.1.2. Ca carbonation-calcination equilibrium

The equilibrium constant for the carbonation and calcination reaction is described by Eq. (6.7) in which it can be seen that it is related to the partial pressure of CO_2 only. The departure from equilibrium thus depends solely on the partial pressure of CO_2 in the system. The standard Gibbs free energy of reaction is obtained in the same way as previously described. Table 6-2 shows the Shomate coefficients and Eq. (6.8) represents the regressed equilibrium constant expression. It can be seen that the equilibrium pressure of CO_2 increases with increasing temperature due to the exothermicity of the reaction ($\Delta H^0_{298K} = -178\ kJmol^{-1}_{CO2}$).

$$K_{Ca,CO_2} = P_{CO_{2,eq}} = exp\left(\frac{-\Delta G^{\circ}_{r,3}(T)}{RT}\right) \tag{6.7}$$

$$K_{Ca,CO_2} = P_{CO_{2,eq}} = 10^{\left(8.1282 - \frac{9143.4}{T}\right)} \tag{6.8}$$

Table 6-2: Coefficients of Shomate equations for calculation of the standard Gibbs free energy of components for the calcium system retrieved from FactSage©.

$CaCO_3$		**CaO**		**CO_2**	
Ai	**X_i**	**Ai**	**X_i**	**Ai**	**X_i**
-298115.178		-155655.5109		-99325.71845	
151.1862752	T	90.02785941	T	153.6252232	T
-24.98	TlnT	-14.051427	TlnT	-24.69995283	TlnT
-0.00262	T^2	137087.235	T^{-1}	0.000566755	T^2
310000	T^{-1}	-128.015296	$T^{0.5}$	4809.876238	T^{-1}
		-4102086.833	T^{-2}	-1671.402708	$T^{0.5}$
				2630.196128	lnT

6.1.2. Equilibrium based on isotherms

The goal is to have a dynamic simulation as function of time in which the incoming feed instantly goes to its equilibrium depending on the present gases and solids in the system as described by the equilibria in the previous section. This means that the gas mixture – which is not at equilibrium – instantly reacts to its equilibrium composition, thereby converting the solids according to the reaction that is taking place. Reaching equilibrium can, however, only take place when the solids are still available for reaction and thus it is crucial to take into account the conversion of the solids. This approach inherently assumes that there are no kinetic and mass transfer limitations, it thus represents the best case scenario.

One possible approach is the use of adapted isothermal equations. As described in Chapter 3, isotherms describe the amount of loading (in $kmol.kg^{-1}$) of a component in equilibrium with the corresponding solid as function of partial pressure at a constant temperature. For adsorption processes, the amount of loading depends on the available surface and the interactions between the gas component the surface of the solid. The equilibrium loading increases with partial pressure of the gas component up to the solid saturation.

In this work, analogously to adsorption phenomena, the three gas-solid reactions are represented with the use of isothermal equations. For the adsorption of CO_2 on CaO, this analogy is intuitively as CO_2 is either adsorbed or desorbed. However, for redox reaction a certain gas components reacts to a certain product and thus both the reactant and product should be taken into account. The idea is that a component reacting with a solid is represented by adsorption of this component on the solid, accompanied with the simultaneous desorption of the associated product from the solid of the corresponding reaction, whilst taking into account the stoichiometry of the reaction. Therefore, the maximal amount of loading of a component at equilibrium is determined by the stoichiometry of the corresponding reaction and thus by the available moles of solid reactant. The latter can be calculated using the inverse of the molar mass of the solid, assuming 100% availability of the solid for reaction. The change of loading is then – differently from adsorption phenomena – a function of the departure of the gas composition from the equilibrium constant of the corresponding gas-solid reaction. The three previously described equilibria in Section 6.1.1 for the reduction of Fe with CO and H_2 and the carbonation of Ca with CO_2 are the basis for determining the departure of equilibrium.

6.1.2.1. Adsorption isotherm representation of gas-solid reactions

Isotherms for adsorption processes have a gradual increase of loading as function of partial pressure of the component as shown in Chapter 3. Contrary to the latter, in this work the instantaneous reaching of equilibrium should be represented by a stepwise-like profile of the

loading as function of the gas mixture composition. The steep increase or decrease in loading of a component, depending on adsorption or desorption, will occur at the equilibrium composition of the corresponding reaction. This reasoning is schematically shown in Figure 6-1. For the redox reactions with iron, in case the gas composition of the arbitrary molecules *A* and *B* is higher than its equilibrium constant $K_{A/B}$ of their reaction over the solid *X*, the reaction from *A* to *B* will be favored to reach equilibrium which will be represented by molecule *A* adsorbing on the solid and molecule *B* desorbing from the solid. In the opposite way, when the gas composition of *A* and *B* is smaller than $K_{A/B}$, molecule *B* is adsorbed on the solid and molecule *A* is desorbed from the solid. Depending on the value of $K_{A/B}$ these zones shift to the right or to the left. For the calcination/carbonation reaction, only one isotherm is required as only CO_2 is either adsorbed or desorbed as shown in Figure 6-1.

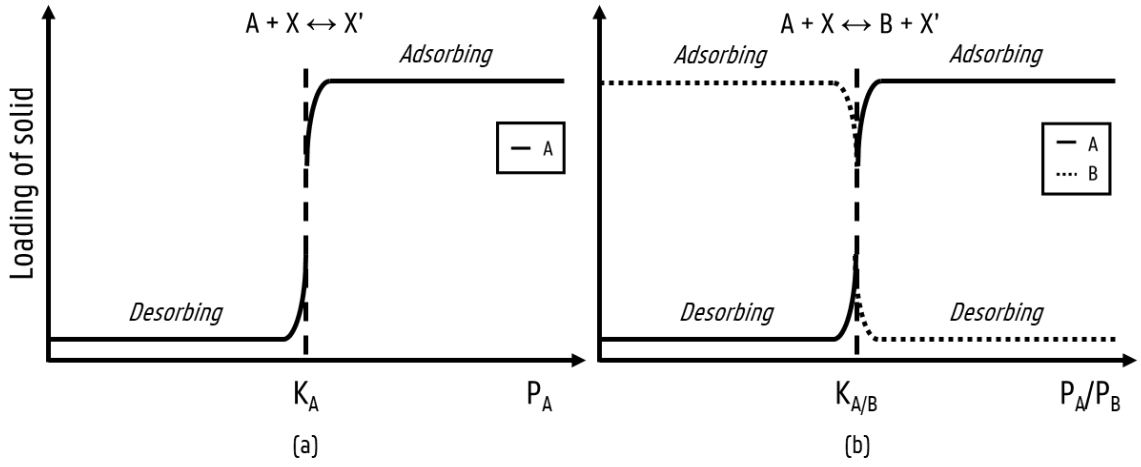

Figure 6-1: Schematic of isotherm representation of gas-solid reaction (a) calcination/carbonation reaction: molecule A adsorbed when P_A is greater than K_A (b) redox reaction A+X <-> B +X'. Loading of solid as function of gas composition for which $P_A/P_B < K_{A/B}$, A desorbing, B adsorbing. $P_A/P_B > K_{A/B}$, A adsorbing, B desorbing.

A mathematical expression is needed for the implementation of such a stepwise isotherm. The use of a piecewise function based on conditional statements is avoided because of the discontinuity and the corresponding calculation difficulties. A smooth S-shaped curve approximates a stepwise function and seems suitable for the isotherm representation. A Sigmoid function is a mathematical function having such characteristic S-shaped profile [68]. The general format of a Sigmoid function is shown in Figure 6-2. The steepness of the function can be adapted by changing the steepness factor c_1 yielding a steeper function for higher values which is desired to approximate a stepwise function. The function is asymptotically zero left from the central point c_2 and asymptotically equal to one to the right of c_2. The central point c_2 represents the equilibrium constant. Multiplication of the function with the maximal amount of loading will yield the final form of the isotherm in this work.

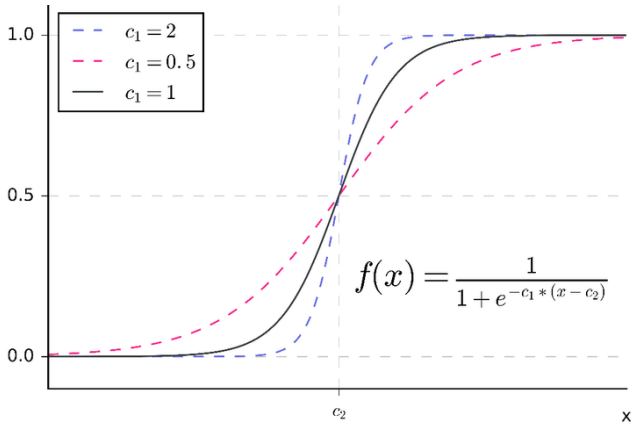

Figure 6-2: Graphical representation of Sigmoid curve for three different steepness factor c_1 [68].

It must be noted that the isotherm determines the equilibrium loading at the corresponding conditions of the reactor. The actual loading of the solid is determined by the mass transfer of the components from the gas phase to the solid surface. As previously mentioned in Chapter 5, the mass transfer model is based on a simple linear driving force model in which the mass transfer coefficient *MTC* is put very high to approximate no mass transfer limitations. The amount of molecules present in the gas phase of the reactor is thus instantly adsorbed until the maximal equilibrium loading is reached, i.e. full conversion of the solid.

The following two sections elaborate on the final form of the isotherm representation of the three gas-solid reactions taking place in this work.

6.1.2.1.1. Carbonation and calcination

The calcium solid is in equilibrium with CO_2 in the gas phase according to the carbonation and calcination reaction. Its equilibrium constant is solely related to the partial pressure of CO_2 in the reactor as previously discussed. Consequently, only one isotherm is required for CO_2 adsorption. The equilibrium loading profile of CO_2 in the isotherm representation depends on the partial pressure of CO_2 in the gas phase of the reactor P_{CO_2} and its departure from the equilibrium partial pressure of CO_2 at the $CaO/CaCO_3$ solid's surface K_{Ca,CO_2} as shown in Eq. (6.9).

$$w^*_{Ca,CO_2} = w_{Ca,CO_2,max} / \left(1 + e^{-C_{Ca}\left(P_{CO_2} - K_{Ca,CO_2}\right)}\right) \tag{6.9}$$

Figure 6-3 shows the isotherm representation of the carbonation and calcination reaction. For a temperature of 1162 *K* the equilibrium CO_2 pressure is equal to 0.93 *bar*, which can be seen as the transition point in the Sigmoid curve. At higher temperatures, this transition point shifts to the right due to the exothermicity of the reaction. The maximal loading capacity is equal to the inverse of the molar mass of the CaO solid (56.07 $g.mol^{-1}$) which results in 0.0178 $kmol.kg^{-}$

[1] CaO available for reaction. The CaO solid loaded with CO_2 represents $CaCO_3$, while when there is no CO_2 loaded, it represents CaO. It can be seen that carbonation or adsorption takes place when the partial pressure of CO_2 is larger than the equilibrium pressure and calcination or desorption in the reverse case.

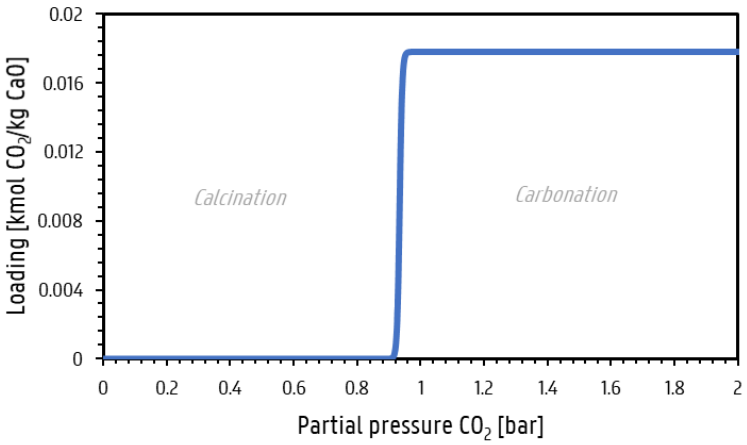

Figure 6-3: Loading of CO_2 on CaO as function of CO_2 partial pressure for the isotherm representation of the calcination and carbonation gas-solid reaction at a temperature of 1162 K with $K_{Ca,CO2}$ equal to 0.93 bar and C_{Ca} to 250.

6.1.2.1.2. Reduction and oxidation of iron

The iron solid is in equilibrium with two subsystems, i.e. the redox reaction with H_2O and H_2 and CO_2 and CO. For each subsystem the equilibrium constant relates to both components of the corresponding subsystem. Consequently, each subsystem is described by one isotherm per component, i.e. two isotherms in total. For the subsystem of iron with H_2O and H_2, the equilibrium loading profile of H_2O in the isotherm representation depends on the composition of H_2O and H_2 in the gas phase of the reactor P_{H_2O}/P_{H_2} and its departure from the equilibrium constant K_{H_2O/H_2} as shown in Eq. (6.10). Because of the stoichiometry of the reaction, the amount of H_2O adsorbed should be equal to the amount of H_2 desorbed and consequently the isotherm for H_2 is the complement to the maximal loading $w_{Fe,H_2O,max}$ of w^*_{Fe,H_2O} as shown in Eq. (6.11).

$$w^*_{Fe,H_2O} = w_{Fe,H_2O,max} / \left(1 + e^{-C_{Fe}\left(P_{H_2O}/P_{H_2} - K_{H_2O/H_2}\right)}\right) \quad (6.10)$$

$$w^*_{Fe,H_2} = w_{Fe,H_2O,max} - w_{Fe,H_2O,max} / \left(1 + e^{-C_{Fe}\left(P_{H_2O}/P_{H_2} - K_{H_2O/H_2}\right)}\right) \quad (6.11)$$

Figure 6-4 shows the isotherm representation of the redox reaction of H_2O and H_2 with iron. For a temperature of 1162 *K* the equilibrium constant is equal to 0.55, which can be seen as the transition point in the Sigmoid curve. At higher temperatures, this transition point shifts to

the right due to the endothermicity of the reaction. The maximal loading capacity is equal to the inverse of the molar mass of the iron solid (55.85 *g.mol*$^{-1}$) which results in 0.017907 *kmol.kg*$^{-1}$ iron available for reaction. It can be seen that iron reduction, i.e. the adsorption of H_2 and simultaneous desorption of H_2O, takes place when the gas composition is lower than the equilibrium constant, whereas oxidation of iron occurs in the reverse case. The iron loaded with H_2O thus represents oxidized iron, i.e. FeO, while iron loaded with H_2 represents reduced iron, i.e. Fe.

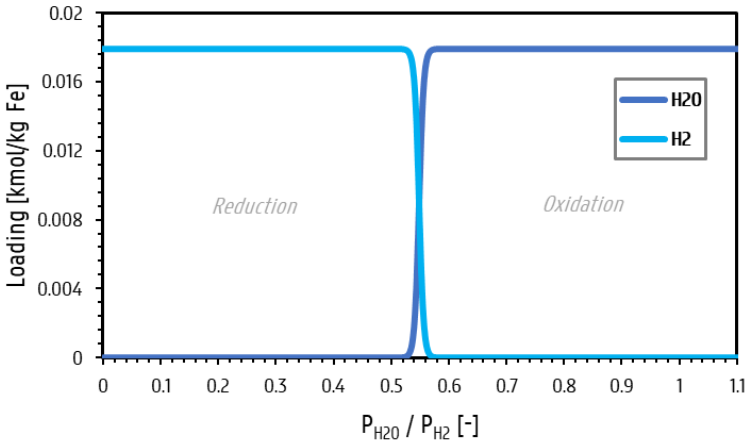

Figure 6-4: Loading of H_2O and H_2 on Fe as function of H_2O and H_2 gas composition for the isotherm representation of the redox reaction at a temperature of 1162 K with $K_{H2O/H2}$ equal to 0.55 and C_{Fe} to 250.

The same reasoning holds true for the subsystem of Fe with CO_2 and CO. The isotherm representation for the redox reaction with CO_2 and CO are shown by Eqs. (6.12) and (6.13) respectively.

$$w^*_{Fe,CO_2} = w_{Fe,CO_2,max} / \left(1 + e^{-C_{Fe}\left(P_{CO_2}/P_{CO} - K_{CO_2/CO}\right)}\right) \tag{6.12}$$

$$w^*_{Fe,CO} = w_{Fe,CO_2,max} - w_{Fe,CO_2,max} / \left(1 + e^{-C_{Fe}\left(P_{CO_2}/P_{CO} - K_{CO_2/CO}\right)}\right) \tag{6.13}$$

Figure 6-5 shows the isotherm representation of the redox reaction of CO_2 and CO with iron. The equilibrium constant is equal to 0.46 at 1162 *K*, which can be seen as the transition point in the Sigmoid curve. At higher temperatures, this transition point shifts to the left due to the exothermicity of the reaction. The maximal loading capacity is equal to the inverse of the molar mass of the iron solid (55.85 *g.mol*$^{-1}$) which results in 0.017907 *kmol.kg*$^{-1}$ iron available for reaction. It can be seen that reduction of iron, i.e. the adsorption of CO and simultaneous desorption of CO_2, takes place when the gas composition is lower than the equilibrium constant, whereas oxidation of iron occurs in the reverse case. The iron loaded with CO_2 thus represents oxidized iron, i.e. FeO, while iron loaded with CO represents reduced iron, i.e. Fe.

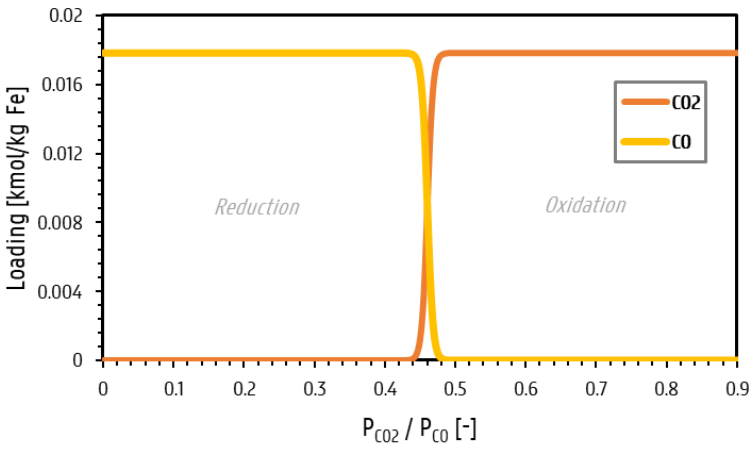

Figure 6-5: Loading of CO_2 and CO on Fe as function of CO_2 and CO gas composition for the isotherm representation of the redox reaction at a temperature of 1162 K with $K_{CO2/CO}$ equal to 0.46 and C_{Fe} 250.

Both iron subsystems of H_2O and H_2, and CO_2 and CO take place at the same time during reduction, thus the (R)WGS equilibrium is obtained. Both subsystems depend on the loading capacity of iron, which cannot be higher than the maximal loading capacity as earlier defined. Consequently, prior to running the simulation, a distribution of the maximal loading capacity has to be assigned to each subsystem as is shown in Eq. (6.14).

$$w_{Fe,max} = w_{Fe,H_2O,max} + w_{Fe,CO_2,max} \tag{6.14}$$

6.1.3. Aspen Adsorption© isotherm implementation

A combination of all the aforementioned isotherms can be used to simulate an equilibrium based model for gas-solids reactions limited by the solids availability in the reactor. The isothermal equations are implemented in Aspen Adsorption© through a user defined FORTRAN subroutine called *pUser_g_Isotherm_P*.

If only calcium is present, only Eq. (6.9) is required to represent the carbonation/calcination reaction. In case only iron is present, Eqs. (6.10), (6.11), (6.12) and (6.13) are required to represent the (R)WGS redox reactions. In case both solids are present, the isotherms for the same gas component are summed up, i.e. only for CO_2 both Eqs. (6.9) and (6.12) are summed.

It has to be noted that in Aspen Adsorption© differentiation between different kinds of solid sorbents is not possible. Consequently, all aforementioned maximal loading capacities are for the subsystems separately when only one ‘sorbent’ is present in the reactor. In case multiple subsystems are considered together with multiple solids, the one solid sorbent defined in Aspen Adsorption© represents both the calcium and iron solid. Therefore a distribution of the maximal loading capacity is required, which changes accordingly to the composition of the solid mixture and the availability for each component.

6.2. Aspen Adsorption© flowsheet

The general flowsheet configuration in Aspen Adsorption© used in this work is depicted in Figure 6-6. On the right, the single reactor configuration can be seen. It contains several blocks that each require input from the user:

- **Feed blocks:** F1, F2 and F3 represent feed blocks for which temperature, pressure and feed composition are required as input.
- **Product blocks:** P1 and P2 represent the product blocks in which the temperature and pressure of the product outlet are specified.
- **Valve blocks:** VF1, VF2, VF3, VP1, VP2 represent valve blocks can be tailored to be closed, fully open, to let flow go through at a fixed rate or based on a fixed CV-value. No temperature change is taken into account for the valves.
- **Bed block:** B1 represent the packed bed reactor which is configured as discussed in Chapter 5. The exact specifications will be elaborated further on.
- **Void blocks:** B2 and B3 represent the voids at the top and the bottom of the packed bed and are required to simulate co- and counter-current flows.
- **Cycle organizer:** the cycle organizer is a simulation tool provided in the program for automatic control and manipulation of block settings to simulate different steps of a cycle.

The flows and their direction depends on the settings of the valves and the feed and product pressure. Five flow directions are targeted for this process; (1) F1 to B1 for pressurization of the bed, (2) F1 to P1 for reduction and adsorption, the fresh goes through the reactor and the raffinate product goes out, (3) B1 to P1 or P2 for depressurization of the bed and extract production at the outlet, (4) F2 to P2 for counter-current purge and (5) F3 to P3 for co-current purge.

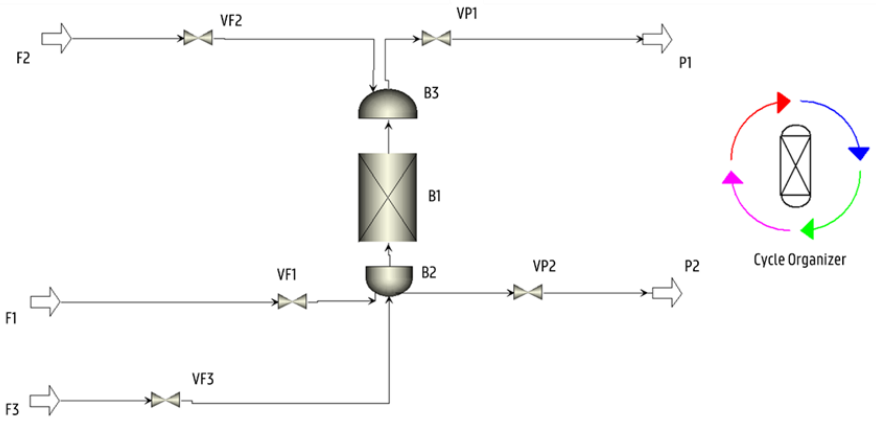

Figure 6-6: General flowsheet of Aspen Adsorption© simulator program containing the reactor configuration on the left and cycle organizer on the right.

6.2.1. Feed and product block specification

The feed F1 consists of the product composition from the outlet of the dry reforming unit obtained in the work of Claus [8] and can be found in Table 6-3. On the one hand, depending on the temperature specified in the chemical looping reactor – that determines the thermodynamics of the iron system – the feed can either have a reducing or an oxidizing nature with respect to the iron solid. On the other hand, depending on the total pressure and the temperature in the reactor – that determine the thermodynamics of the calcium system – the feed can lead to carbonation or calcination. The default temperature and total pressure are 1093 *K* and 15 *bar,* respectively, as taken from the results of Claus [8]. The latter two will, however, be adapted as will be shown in Chapter 7.

Table 6-3: F1 feed composition as obtained from the outlet of the dry reforming unit from the work of Claus [8].

Component	F1 molar fraction [-]
CO	0.420
CO2	0.248
H2	0.238
H2O	0.091
CH4	0.003

The purge gas feed composition cannot be determined beforehand as this will be composed of the raffinate or extract composition obtained during the dynamic simulations of this work. The product block's pressure specification depends on the step of the cycle, i.e. during raffinate production a pressure drop of 0.2 *bar* is assumed across the reactor and during extract production the pressure decreases to minimum 1 *bar*.

6.2.2. Bed specifications

All bed specifications are summarized in Table 6-4. The bed geometry is specified arbitrarily with a height and diameter of 1 *m* and 0.25 *m,* respectively. The bulk solid density of the solid depends on the composition of the 'sorbent', this value will be determined depending on the Ca:Fe ratio and based on the densities of the pure solids: 3300 $kg.m^{-3}$ for the calcium sorbent and 5740 $kg.m^{-3}$ for the iron sorbent. The mass transfer coefficients for all components are left at their default value, as they indicated to be sufficiently high to assume no mass transfer limitations. Except the mass transfer coefficient of the CH_4 component is put at 0, as it is not taking part of the reactions in this work. All other specification parameters are left at their default value as well, including the inter-particle and intra-particle voidage, the sorbent particle diameter and sphericity factor.

Table 6-4: Specifications of the bed block in the Aspen Adsorption© flowsheet used in this work.

Specification	Value
Height of sorbent layer	1 *m*
Diameter of sorbent layer	0.25 *m*
Inter-particle voidage	0.42
Intra-particle voidage	0.21
Bulk solid density	Calcium 3300 $kg.m^{-3}$; Iron 5740 $kg.m^{-3}$
Sorbent particle diameter	0.001 *m*
Sphericity factor	1
Mass transfer coefficient (CO,CO_2,H_2,H_2O)	0.05 $m.s^{-1}$
Mass transfer coefficient (CH_4)	0 $m.s^{-1}$

6.2.3. Flowsheet initialization

The simulation requires an initialization for the amount of loading on the solid and for the gas composition inside the bed and voids. It is assumed that the whole bed is fully calcined and fully oxidized at the start of the simulation. Consequently, the iron is completely loaded with H_2O and CO_2, and the calcium is completely unloaded with CO_2.

6.2.4. Cycle Organizer

The Cycle Organizer is a tool provided in Aspen Adsorption® to simulate different steps of cyclic processes. Herein, different steps can be defined with their corresponding control and manipulation actions. The cycle of the combined chemical looping concept consists of four main steps of which the corresponding control and manipulation actions are shown here.

I. **Pressurization:** The bed starts at an initial pressure of 1 bar. Only valve VF1 is put open, whereas all others remain closed. The feed F1 enters the reactor at a pressure of 15 *bar*, thereby increasing the reactor bed's pressure. This step is stopped by an event driven control action when reaching a pressure of 15 *bar* inside the bed.

II. **Reduction and adsorption:** After Step I, valve VP1 is opened and the product pressure is set at 14.9 *bar*. The reduction regime takes place during this step by which a raffinate product is obtained. This step is stopped when the last node of the reactor is fully oxidized.

III. **Depressurization/oxidation and calcination:** After step II, valve VF1 is closed and either valve VP1 is left open or valve VP2 is opened while VP1 is closed depending on the direction of the flow. The product pressure is set at 1 *bar*, thereby decreasing the pressure of the system and letting the oxidation regime take place by which a extract product can be obtained. This step is stopped by either an event driven control action when a certain degree of oxidation is reached or by a timer.

IV. **Purge/oxidation and calcination:** After step III, the last step consists of a purge step which can either be performed counter- or co-current to the feed of Step I. The former is executed by having VF2 and VP2 opened, while the others remain closed. The latter is done by having VF3 open and VP1 opened. During this step further oxidation and regeneration of the bed takes place by making use of the obtained extract or raffinate product. This step is stopped when a fully regenerated bed is reached, i.e. fully calcined calcium and oxidized iron.

6.3. Drawbacks of methodology

The methodology based on the isotherm approach for equilibrium simulations used in this work directly opposes some drawbacks to the simulation. One is about the isotherm approach itself, the other is about assuming equilibrium.

The isotherm approach implemented in Aspen Adsorption© makes it possibly to define one sorbent per reactor only. Consequently, there is no physical differentiation in the model, but only a mathematical differentiation between two solid sorbents in the bed. Therefore, prior to the simulation, the loading capacity of the two solids has to be adjusted according to the composition of the solid. In addition for the iron solid, its loading capacity has to be distributed and assigned to the H_2O/H_2 and CO_2/CO subsystem prior to the simulation. The *a priori* assignment of these distributions will directly affect the outcome of the simulation, thereby increasing the artificial nature of the simulation. This, however, makes that the analysis of the results easier and more intuitive.

The assumption of reaching instantaneous equilibrium also opposes drawbacks to the analysis of the simulation. Using this approach, all components are assumed to reach equilibrium equally fast and thus there will never be a rate limiting step in this simulation which would affect the process dynamics significantly. In the previous work of Claus [8] the identified rate limiting steps – based on the assumed kinetic models – are the reduction of iron by CO and its reoxidation in the reducer and oxidizer regime respectively, which will not be further investigated in this work.

Chapter 7

Results and discussion: Separate solids dynamic simulation

In this chapter the simulation results for two cases in which only one of the two solids is present are presented and discussed, together with the challenges and limitations of the applied methodology. The dynamics of a packed bed with only Fe for the (R)WGS and with only Ca for CO_2 capture are analyzed to get acquainted with the dynamics of the separate systems.

7.1. Iron (reverse) water gas shift dynamics

In this first case study, the outlet of the reformer is used as feed and goes over a bed with a height of 1 *m* and diameter of 0.25 *m*, composed of only iron at a total pressure of 15 *bar* and a default temperature of 1093 *K*. The feed's composition as shown in Table 7-1 indicates that the RWGS is favored because the feed gas ratio for WGS is higher than the equilibrium. The consumption of H_2 is accompanied with reduction of FeO, while the consumption of CO_2 occurs by oxidation of Fe. The feed thus is both oxidizing and reducing with respect to iron. As the bed is initialized with a fully oxidized state, i.e. FeO only, it is expected that H_2 will first reduce the FeO to Fe by which H_2O is produced and subsequently this Fe will be reoxidized again by CO_2 to FeO by which CO is produced.

Table 7-1: Equilibrium calculation of 1 mol of reformer outlet as feed in separate iron system simulation at 1093 K.

Component	Feed [mol]	Equilibrium [mol]	Δ[mol]
	$K_{CO2/CO} = 0.589$	$K_{CO2/CO} = 0.508$	
CO	0.420	0.443	0.0225
CO2	0.248	0.225	-0.0225
	$K_{H2O/H2} = 0.385$	$K_{H2O/H2} = 0.497$	
H2	0.238	0.220	-0.0178
H2O	0.091	0.109	0.0178
	$K_{WGS} = 1.531$	$K_{WGS} = 1.022$	
CH4	0.003	0.003	/

Figure 7-1 (a) shows the gas composition as function of the reactor length after feeding the feed for arbitrarily chosen 3000 *seconds*. Counterintuitively to what was described above, there is no change in the molar fraction of CO_2 and CO, but only of H_2 and H_2O to their equilibrium composition.

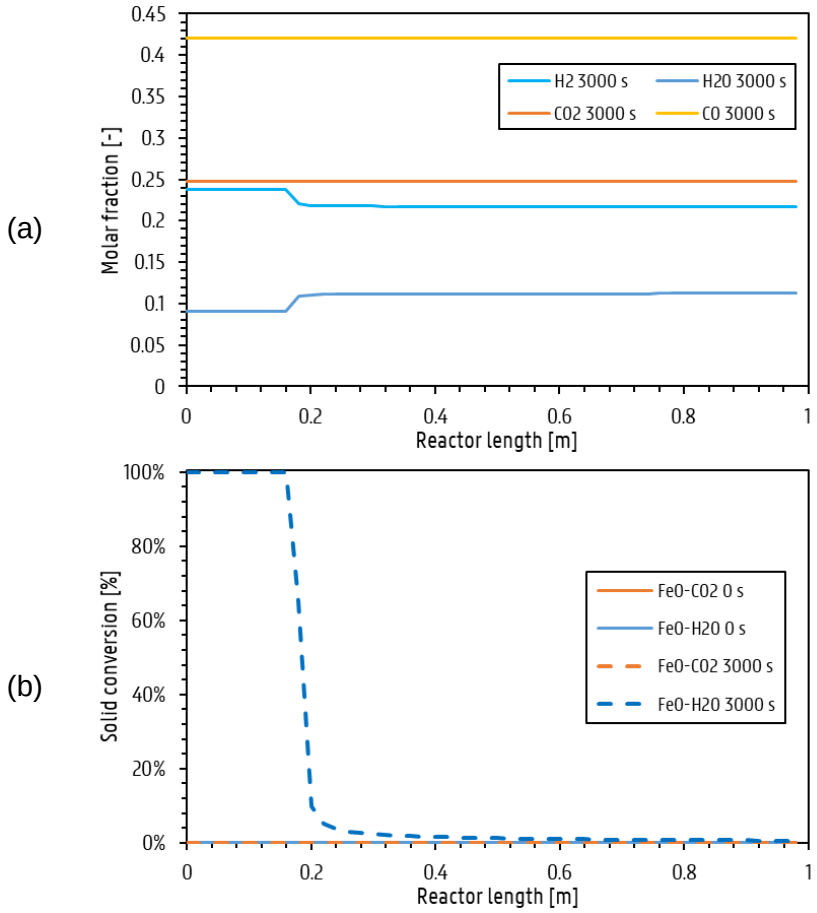

Figure 7-1: Reactor operated at temperature of 1093 K with reformer outlet as feed: (a) Dynamics of gas composition in the bed as function of reactor length at t = 3000 s. (b) Dynamics of solid conversion of FeO assigned to H_2O (FeO-H_2O) and CO_2 (FeO-CO_2) as function of reactor length for t = 0 s and 3000 s of feeding.

The reason for this can be found in Figure 7-1 (b) which shows the bed conversion as function of the reactor length. 100% conversion is equivalent to a saturated solid loaded with the corresponding component. It can be seen that at the beginning of the bed part of the FeO assigned to the H_2/H_2O subsystem is getting 100% converted to Fe, while the FeO assigned to the CO_2/CO subsystem remains unchanged throughout the bed. As the feed enters the fully oxidized bed, H_2 reacts over FeO to H_2O thereby partly reducing FeO to Fe (i.e. H_2 will be loaded and H_2O will be unloaded in the isotherm analogy). Whereas for CO_2 there is no Fe present to be oxidized as expected. This is due to the fact that the conversion of FeO of the H_2/H_2O and the CO/CO_2 subsystem is changing independently of each other, caused by the isotherm approach used in this work. Consequently, there is no interchange in the oxidation state of both subsystems and thus Fe will not be available for oxidation with CO_2.

Limitation of the isotherm approach: the loading capacity has to be determined a priori for each component separately, leading to the fact that the oxidation state of the solid is split up for each component individually. Furthermore, the loading of the pair H_2-H_2O changes separately without interaction with other pair CO-CO_2. FeO reduced by H_2 can therefore not be seen by CO_2 and cannot be used for CO production.

The latter example holds true in case that the two subsystems have an opposite oxidizing/reducing nature. In this work, however, the outlet of the reformer as feed will become reducing in nature because of inherent CO_2 capture by the Ca-sorbent, consequently a case with a fully reducing feed is also shown. Table 7-2 represents the case in which a fully reducing feed with respect to iron is used. Herein, both subsystems will reduce FeO to Fe.

Table 7-2: Equilibrium calculation of 1 mol of fully reducing feed used in separate iron system simulation at 1093 K.

Component	Feed [mol]	Equilibrium [mol]	Δ[mol]	Fraction of maximal iron loading
	$K_{CO2/CO} = 0.333$	$K_{CO2/CO} = 0.508$		
CO	0.501	0.457	-0.0581	
CO2	0.167	0.211	0.0581	77%
	$K_{H2O/H2} = 0.385$	$K_{H2O/H2} = 0.497$		
H2	0.238	0.212	-0.0178	
H2O	0.091	0.116	0.0178	23%
	$K_{WGS} = 0.866$	$K_{WGS} = 1.022$		
CH4	0.003	0.003	/	

The dynamic conversion profiles at 3000 s of feeding, shown in Figure 7-2, confirm that now the FeO assigned to both subsystems is converted to Fe. The effect of the latter can be seen in the composition profile of the reactor as shown in Figure 7-3 in which both subsystems' compositions change to approximately the equilibrium composition with molar fractions of 0.450, 0.219, 0.209 and 0.120 for CO, CO_2, H_2 and H_2O respectively. The changing conversion fronts of both subsystems remain approximately together due to the *a priori* assigned distribution of the loading capacity for each component; i.e. the fraction of iron required to reach equilibrium for reduction with CO and H_2 respectively, as shown in the last two columns of Table 7-2. The reaction fronts must remain together to yield the correct (R)WGS equilibrium inside the reactor.

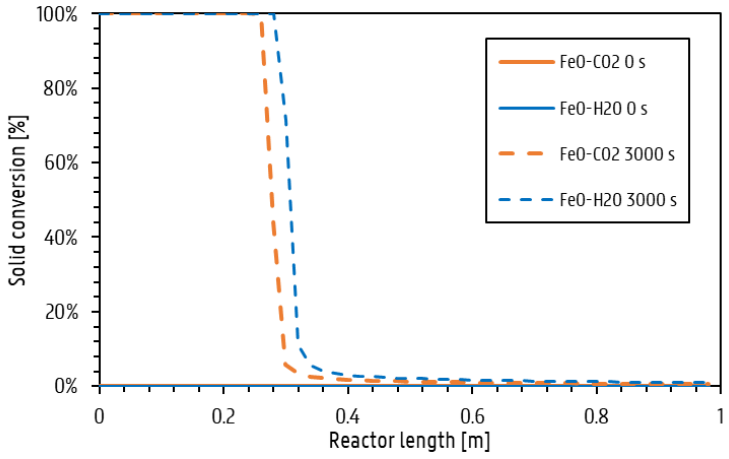

Figure 7-2: Reactor operated at temperature of 1093 K with fully reducing feed: dynamics of solid conversion of FeO assigned to H_2O (FeO-H_2O) and CO_2 (FeO-CO_2) as function of reactor length for t = 0 s and 3000 s of feeding.

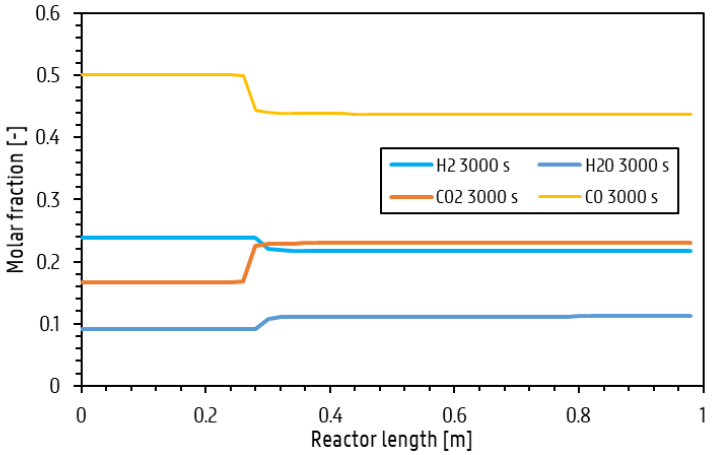

Figure 7-3: Reactor operated at temperature of 1093 K with fully reducing feed: dynamics of gas composition in the bed as function of reactor length at t = 3000 s.

Based on the last example, the methodology applied is able to simulate the reduction of FeO with CO and H_2 correctly as will be the case in reducer regime of the combined chemical looping concept. The obtained equilibrium composition with the simulation is approximately equal to the equilibrium calculation. The oxidation of iron yields the same results, however, here CO_2 is converted to CO while consuming Fe.

7.2. Ca carbon capture dynamics

In this case study, the dynamics of a packed bed reactor for CO_2 capture with a calcium sorbent and its subsequent release are investigated. The relevance of the calcium sorbent is twofold; on the one hand it is necessary to have *in-situ* CO_2 capture during the reducer regime of the combined chemical looping process, thereby making the feed highly reducing with respect to the iron in the combined system. This increases the degree of FeO reduction, yielding capacity for subsequent reoxidation in the oxidizer regime. And on the other hand, the calcium sorbent serves as a CO_2 sink during the reducer regime that is the main reactant source in the oxidizer regime to produce CO, consequently the calcium sorbent is very important.

The calcium system consists of a carbonation reaction for CO_2 capture and a subsequent calcination reaction for the release of CO_2 by making use of pressure swing approach. As the oxidizer regime is constrained to a minimum pressure of 1 bar, the equilibrium pressure of CO_2 in the calcium system has to be higher than 1 bar to be able to self-purge the CO_2. Figure 7-4 shows the equilibrium CO_2 pressure for the calcium system as function of reactor temperature. The partial pressure of CO_2 increases with temperature because of the exothermicity of the carbonation reaction. It can be seen that the default temperature of 1093 *K* yields an

equilibrium pressure of 0.3 *bar* only, therefore the temperature needs to be increased to at least 1170 *K* – with an equilibrium pressure of 1.05 *bar* – to be able to perform the self-purge.

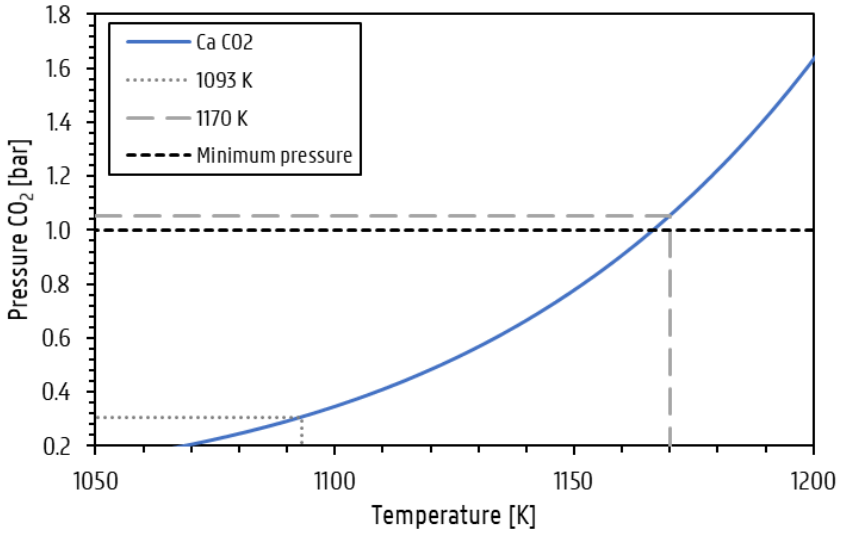

Figure 7-4: Equilibrium pressure of CO_2 in calcium system as function of reactor temperature. Temperature of 1170 K required to have equilibrium pressure of CO_2 higher than minimum pressure 1 bar in oxidizer regime.

The increased equilibrium pressure of CO_2 due to the increase in reactor temperature has as a consequence that less CO_2 from the feed will be captured. This is caused by a decreasing pressure difference that acts as a driving force for the carbonation reaction. Table 7-3 shows the effect of temperature increase in the percentage of CO_2 captured from the reformer outlet at equilibrium at a total pressure of 15 *bar*. For a temperature of 1170 *K*, 77% of the CO_2 can be captured by the calcium sorbent at equilibrium.

Table 7-3: Effect of reactor temperature on percentage of CO_2 captured from the reformer outlet with Ca-sorbent at equilibrium at a total pressure of 15 bar.

Reactor temperature [K]	Equilibrium CO_2 pressure [bar]	Percentage captured [%]
1093	0.31	94
1130	0.57	88
1170	1.05	77
1210	1.88	56

The investigated case thus operates isothermally at 1170 *K* with a pressure of 15 *bar* during the carbonation step and 1 bar during the calcination step. A full cycle consisting of four steps is performed in a calcium bed of 1 *m* height and 0.25 *m* diameter; (I) pressurizing the bed from 1 *bar* to 15 *bar* with the reformer outlet as feed, (II) carbonation with feed until full saturation of the bed, (III) shutting of feed and depressurization from 15 to 1 *bar* and (IV) calcination during self-purge until total regeneration of bed. Equilibrium calculations shown in Table 7-4 represent

the gas phase composition that should be seen during carbonation, whereas during calcination only CO_2 is expected to be present.

Table 7-4: Equilibrium calculation of 1 mol of reformer outlet as feed used in separate calcium system simulation for CO_2 capture at 1170 K and 15 bar.

Component	Feed [mol]	Equilibrium [mol]	Equilibrium fraction [-]	Δ[mol]
CO	0.420	0.420	0.519	/
CO2	0.248	0.057	0.070	-0.191
H2	0.238	0.238	0.293	/
H2O	0.091	0.091	0.113	/
CH4	0.003	0.003	0.004	/

Figure 7-5 represents the characteristic pressure profile as function of cycle time for the pressure swing operation of this case study in which the four different steps can be distinguished. The total cycle time is 8703 *s*, which is too long for industrially practical processes, but the main purpose here is to investigate the process dynamics and not to optimize its cycle.

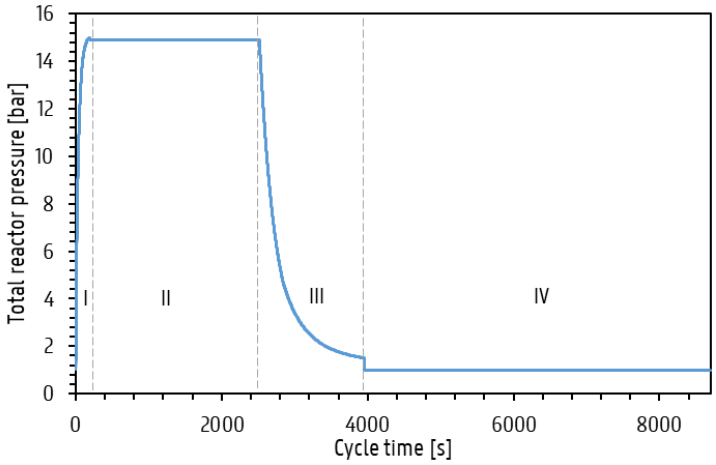

Figure 7-5: Total reactor pressure as function of cycle time with four distinct steps: (I) pressurization, (II) carbonation at 15 bar, (III) depressurization to 1 bar and (IV) calcination at 1 bar.

The pressurization step (I) is finished fairly quickly (191 *s*), after which the carbonation step (II) takes place for 2330 *s*. Figure 7-6 (a) and (b) show the dynamic behavior of the gas composition and solid conversion inside the reactor during the carbonation step for two time snapshots. It can be seen that the degree of carbonation increases with time and the calcium sorbent is saturated at the beginning of the reactor. Consequently, the change in gas composition follows the saturation front of the solids; i.e. at the left from the saturation front the

calcium sorbent is saturated and thus the feed composition can be seen in the composition profile, whereas at the right from the saturation front of the calcium sorbent the equilibrium composition is reached because there is still calcium sorbent available for CO_2 removal. The outlet composition of 0.521, 0.0670, 0.295 and 0.120 for CO, CO_2, H_2 and H_2O respectively match the equilibrium calculations in Table 7-4 well. The simulation yields a CO_2 capture efficiency of 77% as expected from the equilibrium calculations.

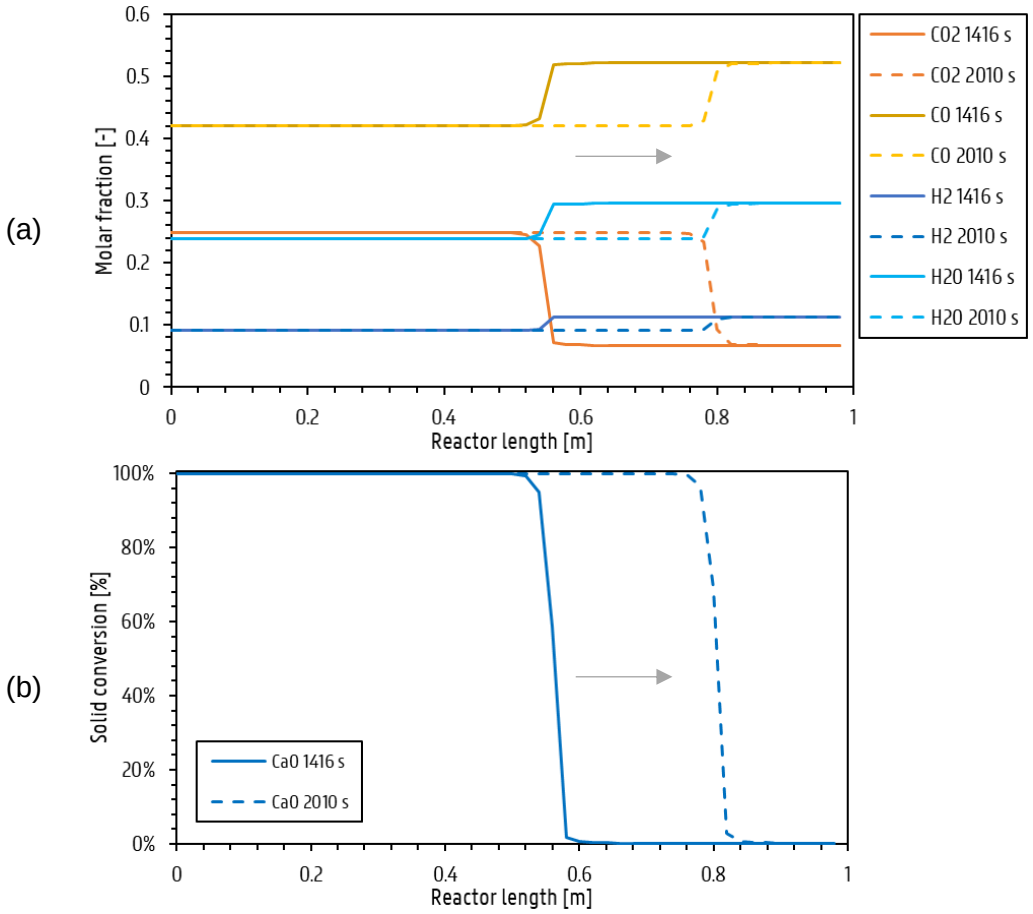

Figure 7-6: Carbonation step at 1170 K and 15 bar with reformer outlet as feed: (a) Dynamics of gas composition in calcium bed as function of reactor length. (b) Dynamics of CaO conversion as function of reactor length. Higher degree of carbonation with increasing time, conversion front shifting to right followed by composition change. Arrow indicates the direction of the feed stream in the reactor.

After the bed is fully carbonated, the depressurization step takes place (III) for 4742 *s*. Herein the pressure is decreased by gradually opening the valve thereby yielding a controllable product flow. After the pressure is almost equal to the calcination pressure of 1 *bar*, the valve is completely opened to let the calcination step (IV) take place. During the calcination step, a pure CO_2 is produced and will be present in the reactor gas phase as shown in Figure 7-7 (a). Depending on the co-current or counter-current self-purge with respect to the feed direction, the conversion front of the $CaCO_3$ moves differently in the reactor. For co-current self-purge

the $CaCO_3$ is calcined first at the product side end and therefore the $CaCO_3$ conversion increases in the reactor as shown in Figure 7-7 (b). The opposite is true for counter-current self-purge as can be seen in Figure 7-7 (c). In both cases of self-purge mode, 100% calcination (or regeneration) of the bed is achieved and thus 100% recovery of the captured CO_2 during the carbonation step is possible. This simulation shows that the applied methodology is able to represent a dynamic equilibrium simulation for CO_2 capture.

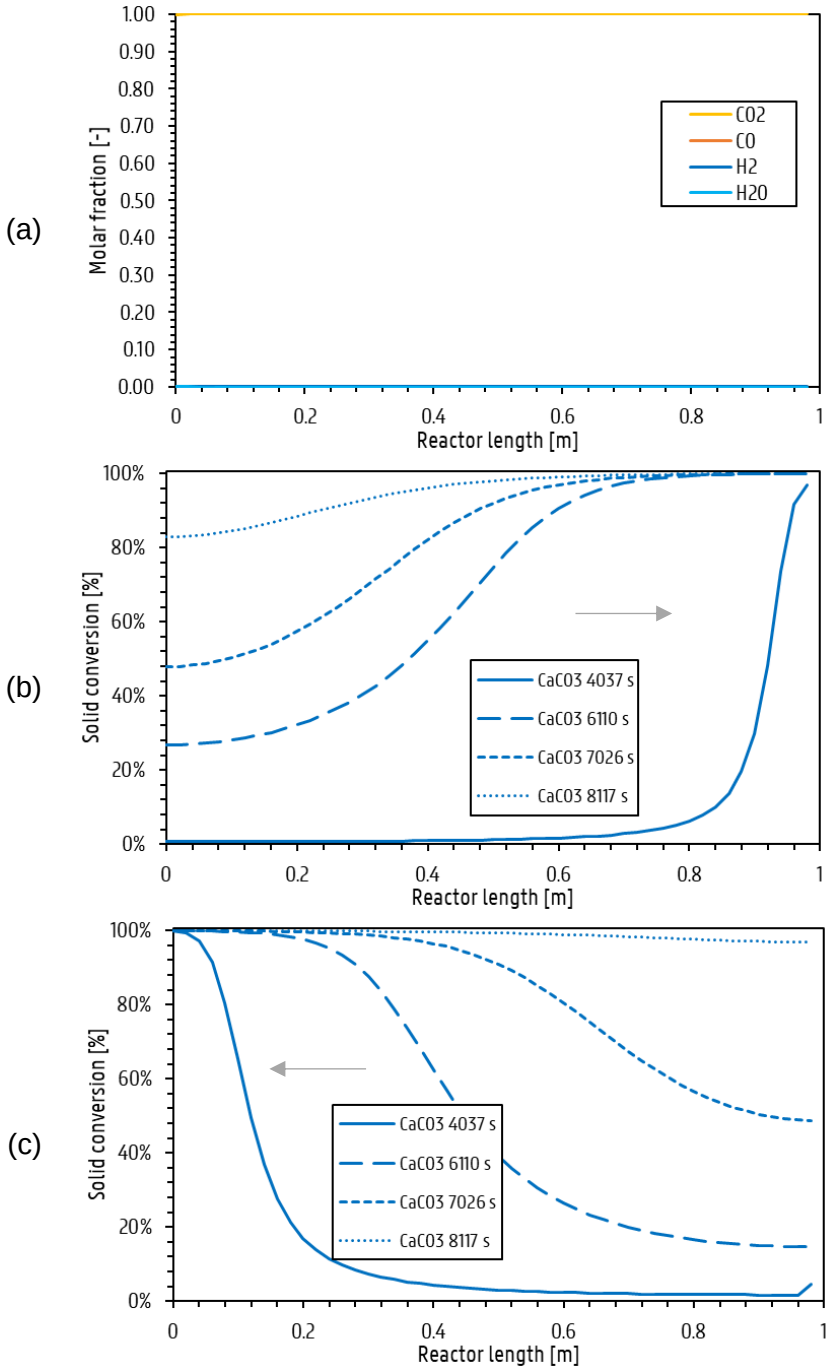

Figure 7-7: Calcination step at 1170 K and 1 bar: (a) Dynamics of gas composition in calcium bed as function of reactor length: pure CO_2 produced during calcination. (b) Dynamics of $CaCO_3$ conversion as function of reactor length for co-current self-purge. Conversion front moving from top to bottom of bed. (c) Dynamics of $CaCO_3$ conversion as function of reactor length for counter-current self-purge. Conversion front moving from bottom to top of bed. Arrow indicates the direction of the product stream leaving the reactor.

It has to be noted that there is a significant time difference between the carbonation and calcination step, with the calcination step taking twice the time of the carbonation step. The latter is due to the difference in driving force created by the pressure difference during the corresponding steps. During carbonation the high feed pressure of 15 *bar* yields a big driving force for carbonation to occur, whereas for calcination the calcination pressure of 1 *bar* only yields a small driving force thereby increasing the duration for full calcination.

Chapter 8

Results and discussion: Combined solids dynamic simulation

In this chapter the results of the combined chemical looping concept with the iron and calcium solids together are presented and discussed, together with the challenges and limitations of the applied methodology. First, the chosen operating conditions for the combined system is elaborated up on. Secondly, the general effect of combining the two solids on the dynamics in a packed bed is discussed. Thereafter, a full process cycle of the combined chemical looping concept is presented and discussed. At last, the effect of different adaptations to the process for further optimization is shown.

8.1. Selection of operating conditions

In the combined chemical looping concept, the iron and calcium solid are mixed together in a packed bed. The equilibrium gas composition during the reducer and the oxidizer regime will be determined by the thermodynamics of the two solid systems combined. During the reducer regime, the calcium sorbent will capture CO_2 *in-situ* thereby creating a feed mixture with a high reduction potential with respect to iron. Then in the oxidizer regime, the captured CO_2 will be released and will oxidize the iron, thereby producing CO. As the goal of the combined chemical looping concept is to produce a high purity CO stream, the operating conditions for the oxidizer regime are crucial.

As mentioned before, the oxidizer regime is constrained to a minimum pressure of 1 *bar*. Consequently, the temperature is the only parameter that can adjusted for the oxidizer regime. In the oxidizer, calcination of $CaCO_3$ and oxidation of iron with CO_2 have to take place simultaneously and thus the thermodynamics of the system should allow them, by choosing the operating temperature correctly. Figure 8-1 shows the CO_2 equilibrium pressure determined by the calcium system and determined by the iron system at a total pressure of 1 *bar*. In the oxidizer regime, the equilibrium pressure of the calcium system must be higher than that of the iron system to be able to have a continuous driving force for calcination and oxidation of iron with CO_2 to take place. In this way, the calcium system will yield a CO_2 pressure that induces oxidation of iron and thus production of CO. As a consequence the iron system will reduce the CO_2 pressure to its equilibrium pressure, thereby providing a continuous driving

force for calcination to take place. In region (a), left from the intersection of the two equilibrium lines, the reduction of iron and carbonation are favored because of too low CO_2 pressure. Whereas in region (b), the oxidation by CO_2 will be favored as required in the oxidizer regime. Consequently, the operating temperature has to be higher than 1100 *K* at which both equilibriums lines intersect. The default temperature of 1093 *K* is thus too low for the oxidizer regime, yet a temperature of 1110 *K* would suffice. In addition, in case no iron is present, yet only $CaCO_3$, the operating temperature should yield an equilibrium CO_2 pressure higher than 1 bar to be able to regenerate the calcium. Therefore a temperature of 1170 *K* fulfills the aforementioned criteria and is chosen as the operating temperature in this work.

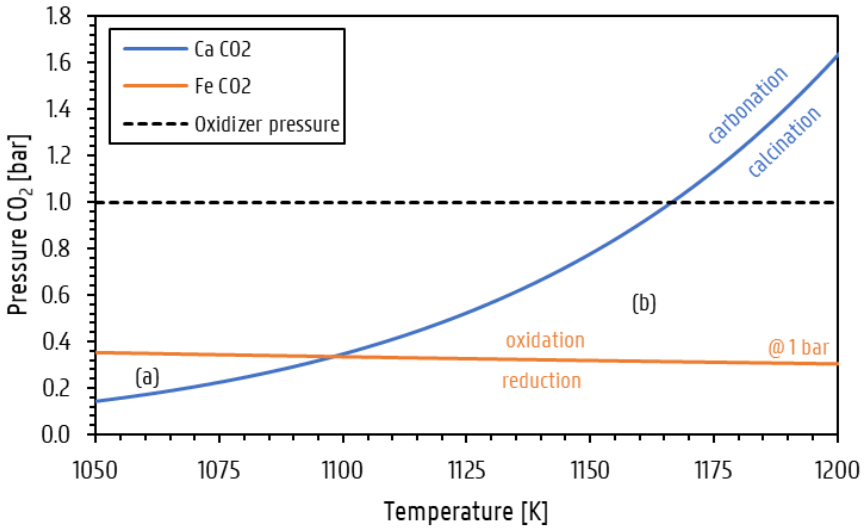

Figure 8-1: Equilibrium pressure of CO_2 for calcium system (blue) and iron system at 1 bar total pressure as function of reactor temperature for the oxidizer regime. Zone (a) left from intersection of both equilibrium lines (1110 K): region for carbonation and iron reduction. Zone (b) right from intersection of both equilibrium lines (1110 K): region for calcination and iron oxidation. Temperature of 1170 K required to have equilibrium pressure of CO_2 higher than minimum pressure 1 bar in oxidizer regime.

The increased temperature of 1170 *K* in the oxidizer regime is beneficial for the extract product composition because of the endothermicity of the oxidation of iron with CO_2. This yields an equilibrium mixture of 68.7 *mol%* CO and 31.3 *mol%* CO_2. Because of the isothermal operation of the combined chemical looping process, the chosen temperature in the oxidizer regime directly affects the equilibrium of the reducer regime. The higher temperature is disadvantageous for the reducer regime, because it decreases the driving force for carbonation due to the exothermicity of the carbonation reaction and the reduction of iron with CO. Although the endothermic reduction of iron with H_2 is favored, it does not counteract the latter and thus overall less reduction of iron takes place. This means that more CO_2 will be lost in the raffinate outlet. Although an increased pressure would counteract the increased temperature effect in the reducer regime, a pressure of maximum 15 *bar* is still used. Moreover, the higher temperature is beneficial for minimizing the Boudouard reaction.

Table 8-1 represents the calculated thermodynamic equilibrium in the reducer regime of the reactor for the reformer outlet as feed. It can be seen that the reduction of iron is greatly enhanced by the *in-situ* CO_2 capture with the calcium sorbent and *vice versa*, as compared to a system with only iron or calcium present as discussed in Chapter 7. Theoretically, 84% of the incoming CO in the feed is converted to CO_2. Whereas 95% of the CO_2 in the feed and produced from CO is captured by the calcium sorbent. Overall 86% of all CO and CO_2 is retained in the form of $CaCO_3$. Consequently, the raffinate product stream leaving the reactor during the reducer regime is rich in H_2O and H_2 and poor in CO and CO_2.

Table 8-1: Equilibrium calculation of 1 mol of reformer outlet as feed in reducer regime of combined chemical looping concept at 1170 K and 15 bar.

Component	Feed [mol]	Equilibrium [mol]	Equilibrium fraction [-]	Δ[mol]
CO	0.420	0.066	0.154	-0.354
CO2	0.248	0.030	0.070	-0.217
H2	0.238	0.212	0.494	-0.026
H2O	0.091	0.117	0.274	0.026
CH4	0.003	0.003	0.008	/

8.2. Effect of combined solids

The synergetic effect of the combination the two solids in the reducer regime is verified in Figure 8-2. Herein, the solid conversion and gas composition profile in the reactor is shown for different beds with equal amount of calcium and iron solid, yet differently distributed. A bed with one, five and ten alternating beds of calcium and iron and a fully mixed bed of calcium and iron is shown after 100 *s* operation in the reducer regime. In one alternating bed of calcium and iron – shown in Figure 8-2 (A-1) and (A-2) – it can be seen that carbonation takes place first, thereby decreasing the CO_2 partial pressure in the reactor to its equilibrium partial pressure and creating a highly reducing mixture with respect to iron. Then, this mixture reduces the subsequent iron solid, thereby increasing the partial pressure of CO_2 and H_2O, and decreasing the partial pressure of H_2 and CO. In case more alternating beds of calcium and iron are used, after each layer of iron, carbonation can take place again as the reduction of iron increased the partial pressure of CO_2. In this way the calcium keeps inducing reduction, whereas the iron keeps inducing carbonation. The more alternating beds in series, the more CO_2 is taken out of the system, thereby lowering the partial pressures of CO_2 and CO every subsequent alternating layer. The conversion and composition profile indicate that the driving force for carbonation and reduction to take place reduces with more consecutive alternating layers as equilibrium is being approached.

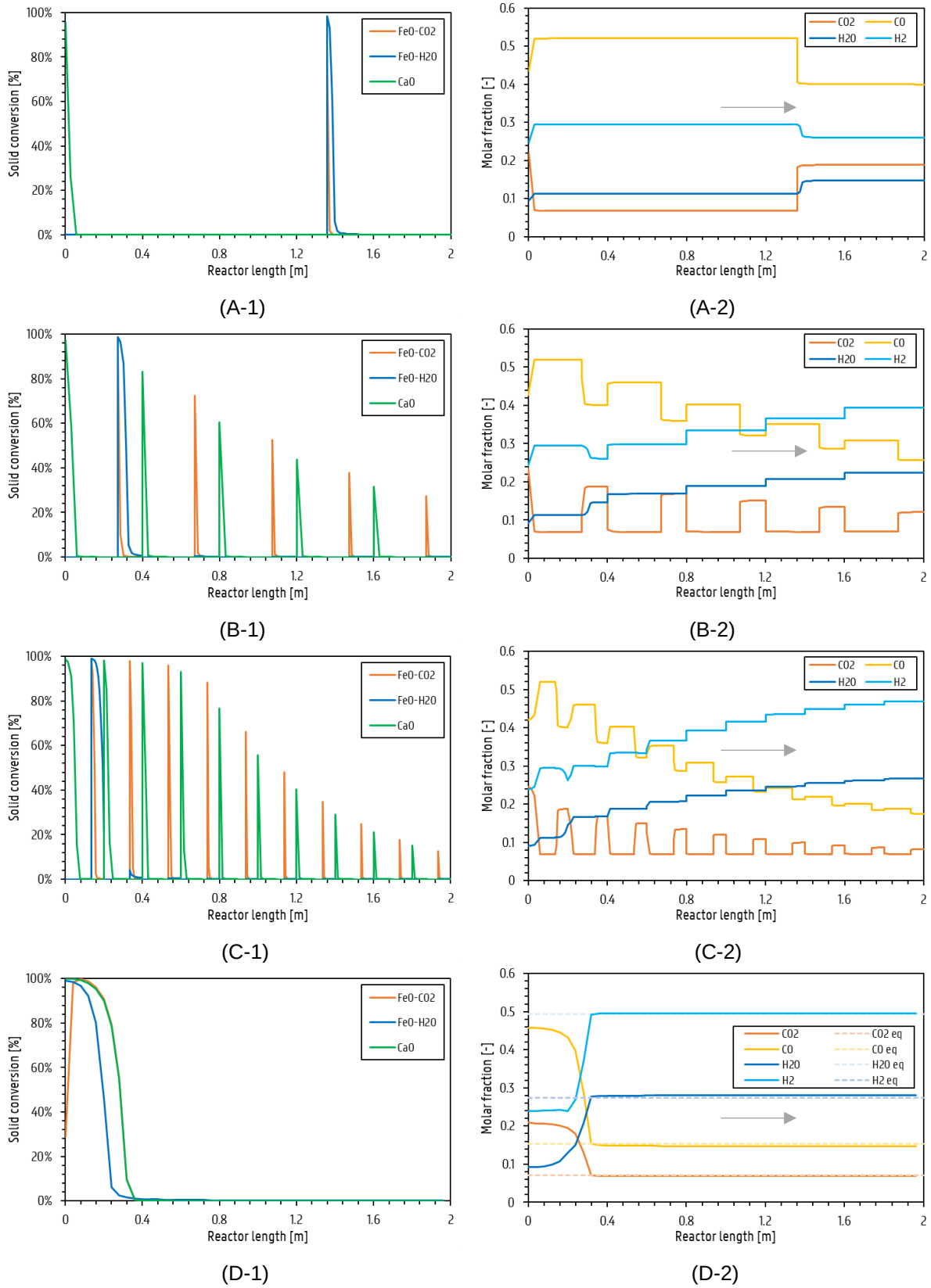

Figure 8-2: (A) One alternating bed of calcium and iron, (B) 5 alternating beds of calcium and iron, (C) 10 alternating beds of calcium and iron and (D) fully mixed bed of calcium and iron. (1) Conversion profile of solids and (2) composition profile in reactor during reducer regime (1170 K, 1 bar) after 100 s. Arrow indicating direction of flow.

For five alternating layers of calcium and iron, in Figure 8-2 (B-1) and (B-2) it can be seen that equilibrium is not reached as the gas composition still changes significantly. Whereas for ten alternating layers, Figure 8-2 (C-1) and (C-2) show that almost no change in the gas phase composition occurs as equilibrium is almost reached. Ultimately, this enhancing effect is best utilized in a fully mixed bed as shown in Figure 8-2 (D-1) and (D-2). This fully mixed bed can be described as an infinite amount of alternating layers of calcium and iron. Consequently – contrary to the stepwise profile to reach the equilibrium composition in the previous shown alternating beds – the equilibrium composition is reached almost instantaneously as shown by the steep composition front inside the reactor.

The enhanced effect of the combination of the solids on the conversion of the solids in the reducer regime is shown in Table 8-2. It can be seen that with a higher degree of mixing – i.e. a higher amount of alternating layers and ultimately a fully mixed bed – an increase in amount of reduced iron and carbonated calcium is achieved after 100 and 400 *s*. Consequently, a higher degree of mixing results in shorter time required to reach full conversion of a certain solid; in this case total carbonation of calcium occurs after 1371 *s* for a fully mixed bed, whereas for one alternating bed it takes 4718 *s*. Therefore, it can be concluded that a mixed bed is beneficial for the reducer regime as it yields the highest solid conversion and is able to achieve the equilibrium composition in the reactor.

Table 8-2: Solid fraction present in reactor after 100 s and 400 s in reducer regime and until total carbonation of calcium.

Alternating beds	**1 series**	**5 series**	**10 series**	**Fully mixed bed**
$t_{reducer}$ = 100 s				
Fe	2%	6%	9%	12%
FeO	98%	94%	91%	88%
$CaCO_3$	2%	8%	11%	14%
CaO	98%	92%	89%	86%
$t_{reducer}$ = 400 s				
Fe	6%	24%	32%	36%
FeO	94%	76%	68%	64%
CaCO3	10%	30%	39%	43%
CaO	90%	70%	61%	57%
Total carbonation	*4718 s*	*2359 s*	*1796 s*	*1371 s*
Fe	65%	76%	79%	81%
FeO	35%	24%	21%	19%
$CaCO_3$	100%	100%	100%	100%
CaO	0%	0%	0%	0%

In the oxidizer regime, the enhanced effect is proven as shown in Figure 8-3 for a bed with five alternating layers of calcium and iron. In the beginning of the reactor, the first $CaCO_3$ layer is calcined, thereby increasing the CO_2 partial pressure. The high CO_2 partial pressure induces the oxidation of iron, thereby increasing the CO partial pressure and decreasing the CO_2 partial pressure. This mixture then goes over the next $CaCO_3$ layer, which induces calcination because of low CO_2 partial pressure and thus acts like a sweeping gas. This enhancing effect makes that calcination induces oxidation of iron, and oxidation of iron induces further calcination during the oxidizer regime. For a fully mixed bed – as shown in Figure 8-4 – this enhancing effect takes place instantaneously, thereby yielding the equilibrium composition along the whole reactor. H_2 and H_2O can be seen to be removed from the reactor caused by the release of CO_2 and to reach negligible partial pressures.

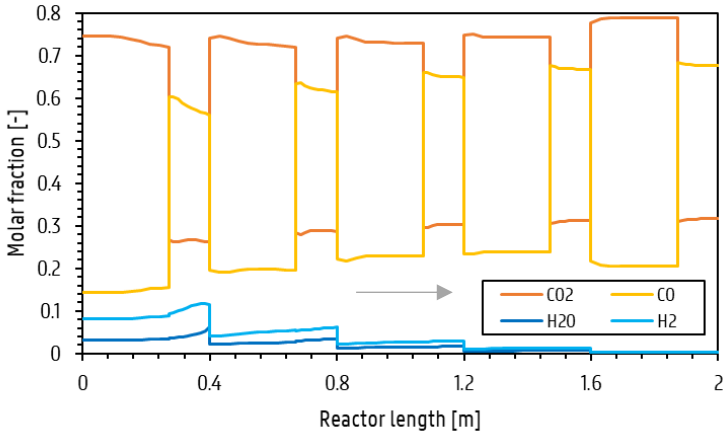

Figure 8-3: Composition profile in reactor during oxidizer regime (1 bar, 1170 K) for 5 alternating beds of calcium and iron. Arrow indicating direction of flow.

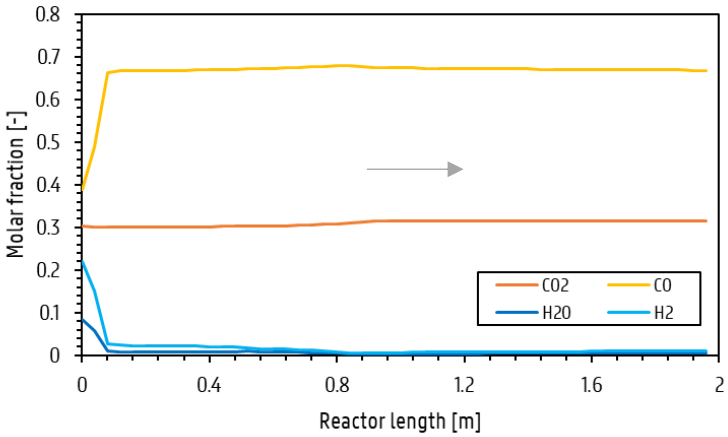

Figure 8-4: Composition profile in reactor during oxidizer regime (1 bar, 1170 K) for 5 alternating beds of calcium and iron. Arrow indicating direction of flow.

8.3. Combined chemical looping dynamics

A full cycle for the combined chemical looping concept using a pressure swing operation is presented in this section. The cycle consists of four steps; (I) pressurization from 1 *bar* to 15 *bar*, (II) feeding the reactor at 15 *bar* for operation in the reducer regime until the iron solid at the end of the reactor is fully reduced, (III) depressurization and self-purge for operation in the oxidizer regime until all iron is oxidized and (IV) a purge step for regenerating the bed. The bed has a height of 1 *m* and diameter of 0.25 *m* and contains 55 *wt%* calcium and 45 *wt%* iron. The average solid bed density is therefore 4080 $kg.m^{-3}$ and the maximal loading capacities for the isotherms of all components are adjusted accordingly. In this simulation, the steepness factor of the sigmoid functions had to be lowered to a value of 50 to be able to run the simulation without convergence problems.

The pressure profile as function of the cycle time retrieved from the simulation – as shown in Figure 8-5 – differentiates the four different steps used in the cycle. The first pressurization step takes 47 *s* to increase the pressure from 1 *bar* to 15 *bar*. Subsequently in the second step in which the reducer regime takes place, it takes 549 *s* to reach full conversion of the iron and calcium solid in the bed. The simulation, however, requires the reducer step to take place until 850 *s* to be able to run the subsequent steps. Letting the reducer step run for longer than required decreases the performance of the total cycle. Therefore, the observed trends are based upon the total performed cycle, whereas the performance metrics will be based upon the data taking into account the reducer step to take place until 549 *s* only. Thereafter, the pressure is decreased to 1 *bar* and the self-purge takes place for 109 *s* during the oxidizer regime until there is no significant flow coming out of the bed. At last, a purge step at 1 *bar* is performed for the remaining 643 *s* until the bed is fully regenerated.

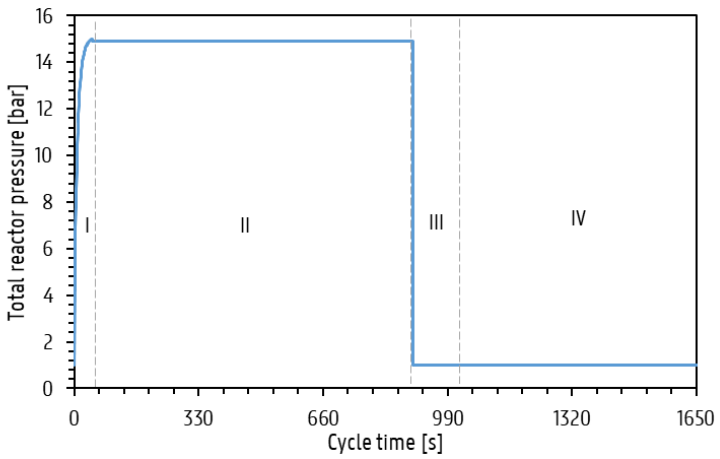

Figure 8-5: Total reactor pressure as function of cycle time with four distinct steps: (I) pressurization, (II) reducer regime at 15 bar, (III) oxidizer regime at 1 bar and (IV) purge at 1 bar.

Figure 8-6 presents the flowrates of the feed, product and purge streams during the four distinct steps. During the pressurization step there is only feeding and no product that is being formed. Starting from the reducer step, a product can be seen formed that has a lower flowrate than the feed, showing the retention of part of the feed in the bed. After 549 *s* in the reducer step, it can be seen that there is breakthrough of the feed taking place: i.e. product and feed flowrates are equal. In the oxidizer regime, product can be seen generated by the self-purging mechanism. At last, a small purge is required to regenerate the bed, yielding a higher flow rate.

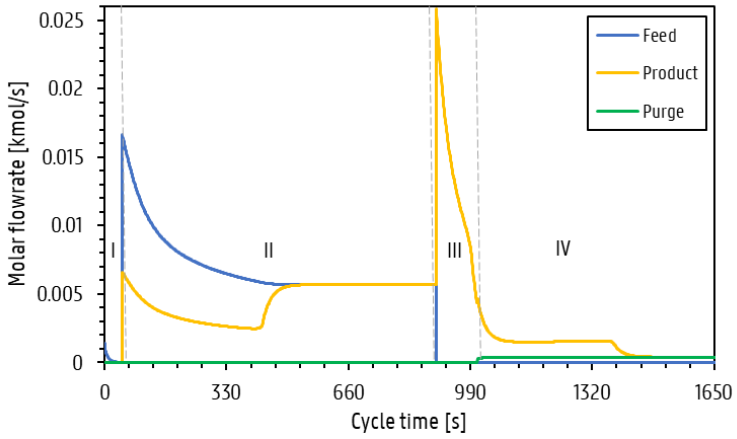

Figure 8-6: Flowrates of feed, product and purge stream with four distinct steps: (I) pressurization, (II) reducer regime at 15 bar, (III) oxidizer regime at 1 bar and (IV) purge at 1 bar.

In the following sections, the results from the last three steps; the reducer regime, the oxidizer regime and the purge step are presented and discussed with a focus on the dynamic behavior of the process and the achievable performance metrics.

8.3.1. Reducer regime

In the second step of the cycle, after a pressurization step from 1 to 15 *bar*, the reducer regime takes place starting from 47 *s* until 549 *s* to reach total conversion of the calcium and iron solid at the end of the bed. Herein, the reformer outlet is fed to the bottom of the reactor at 15 *bar* while at the top of the reactor the raffinate product is withdrawn at a pressure of 14.9 *bar*. As mentioned before, the simulation requires the reducer step to run until 897 *s*, while total conversion of the solids at the end of the bed already takes place at 549 *s*. The latter is believed to be caused by convergence issues. The observed trends will be shown until 897 *s*, whereas taking into account the data until 897 *s* would decrease the performance of the whole cycle significantly and consequently it is chosen to base the performance metrics on the reducer step until 549 *s* only.

The reformer outlet entering the bed leads to carbonation of the calcium solid. The solid conversion profile in Figure 8-7 (a) shows that after 240 *s* part of the calcium solid in the bed has completely converted to $CaCO_3$. The carbonation reaction is accompanied with the reduction of iron because of the obtained highly reducing gas mixture. This leads to the reduction of the iron solid and consequently part of the FeO in the bed is completely converted to Fe as shown in Figure 8-7 (a) after 240 *s* at a reactor length of 0.6 *m*. The conversion fronts of the iron and calcium solid move closely together through the bed because of their enhancing effect. Towards the outlet of the reactor, the CO_2 partial pressure decreases to its equilibrium pressure because of the carbonation reaction, accompanied with the CO_2/CO and H_2O/H_2 systems reaching their corresponding equilibrium with respect to the reduction of the iron solid as can be seen in Figure 8-7 (b). The raffinate product obtained is rich in H_2 and H_2O and poor in CO and CO_2.

Meanwhile, at the beginning of the reactor a new conversion front in the iron solid appears as shown in Figure 8-7 (a) at a reactor length of 0.05 *m*. As the calcium sorbent is already saturated at the inlet of the reactor, the reformer feed is not transformed to fully reducing with respect to iron. Consequently, the CO_2/CO composition keeps its oxidizing nature and thus starts to re-oxidize the freshly reduced iron. After the re-oxidation conversion front, the partial pressure of CO is increased and the partial pressure of CO_2 is decreased to achieve their corresponding equilibrium with respect to the oxidation of iron as can be seen in Figure 8-7 (b).

As time passes during the reducer regime, the conversion fronts of the carbonation of calcium and reduction of iron move towards the outlet of the bed until it can be seen that the remaining CaO and FeO are converted to $CaCO_3$ and Fe respectively after 549 *s*. Also the re-oxidation front moves further towards the outlet of the reactor up to a reactor length of 0.1 *m*. It can be seen that before the re-oxidation front, both $CaCO_3$ and Fe are present. Only at the re-oxidation conversion front the partial pressures in the reactor change, whereas towards the outlet from the re-oxidation front the rest of the calcium and iron is fully converted and thus the composition remains unchanged. At this point in time – at which there is breakthrough of the latter composition – the reducer regime should be stopped by closing the feed valve. In front of the re-oxidation front, there is no change in the gas composition and the reformer feed can be seen here. The simulation, however, requires the reducer step to take place until 897 *s*, which yields a significant higher loss of reduced iron as can be seen in Figure 8-7 (a).

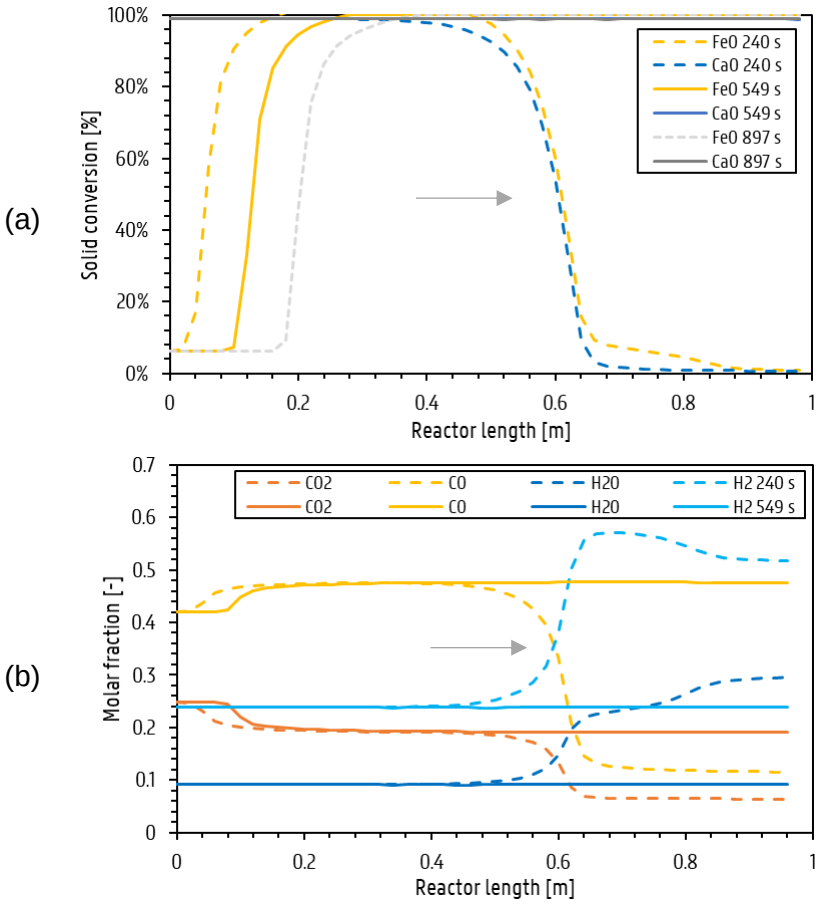

Figure 8-7: Dynamic behavior in reactor during reducer regime at 1170 K and 15 bar at 240 s, 549 s and 897 s: (a) solid conversion profile of CaO and FeO as function of reactor length. (b) Gas phase composition profile as function of reactor length. Arrow indicates direction of flow.

It has to be noted that during the re-oxidation of iron, the FeO conversion decreases until 6% and thus no full conversion is achieved. This deviation is due to the individual assignment of the loading capacity for each reaction that is taking place in the isotherm approach used in this work. The fraction of iron that remains unoxidized, is the part assigned to the H_2/H_2O reaction with respect to iron. Because of the individual assignment, there is no interaction with the CO/CO_2 reaction with respect to iron and thus the reduced iron originating from the H_2/H_2O reaction is not re-oxidized by the oxidizing nature of the CO/CO_2 composition in the feed. Although, the total amount of re-oxidized iron remains the same, it would be distributed differently in the reactor, thereby shifting the re-oxidation front more towards the beginning of the bed. Moreover, as the amount of loading capacity assigned to the H_2/H_2O reaction is only 6%, the effect hereof is expected be minor.

Limitation of the isotherm approach: the loading capacity has to be determined a priori for each reaction separately, leading to the fact that the oxidation state of the solid is split up for each reaction individually. Furthermore, the loading of each component changes individually without interaction with other components. Fe obtained via the reduction with H_2 can therefore not be oxidized with CO_2.

The following performance metrics are based on the reducer step until 549 *s*. At the end of the reducer step, all calcium is carbonated, while only 80% of the iron is reduced. The other 20% is thus reoxidized by the reformer feed. This is a significant loss of reduced iron and because of its purpose to produce CO in the oxidizer regime, it directly affects the performance of the whole process. In total 73% of the fed CO is converted to CO_2 and 91% of the fed CO_2 and CO_2 produced from CO is stored in the bed in the form of $CaCO_3$, the rest thus leaves the reactor in the raffinate product. These inferior performances as compared to the aforementioned theoretical retention of 84% and 95% respectively are due to breakthrough of part of the feed during the carbonation and reduction of the last part of solids. The latter is due to low mass transfer coefficients in the mass transfer equation, consequently not yielding instantaneous loading of the components close to saturation of a solid. Increasing the mass transfer coefficient is again a compromise of yielding more accurate results and being able to run the simulation.

The raffinate composition obtained during the simulation of the reducer step can be seen in Table 8-3. When the breakthrough at the end of the reducer step is not taken into account, it can be seen that the retrieved raffinate product is still off the calculated thermodynamic equilibrium. This can also be seen in a snapshot of the composition profile shown in Figure 8-8. The latter is due to the lower steepness factor in the sigmoid functions, consequently yielding less accurate results. Again this is a compromise of letting the simulation run and retrieve accurate results. In case the breakthrough at the end of the reducer step is taken into account, it can be seen that the outlet contains more feed: i.e. higher in CO_2 and CO and lower in H_2O and H_2.

Table 8-3: Raffinate product composition obtained during the simulation and the calculated thermodynamic equilibrium. NB=no breakthrough. B=breakthrough.

Component	Raffinate product *NB**	Raffinate product *B**	Thermodynamic equilibrium
CH_4	0.007	0.006	0.008
CO	0.111	0.197	0.154
CO_2	0.063	0.092	0.070
H_2	0.520	0.472	0.494
H_2O	0.299	0.233	0.274

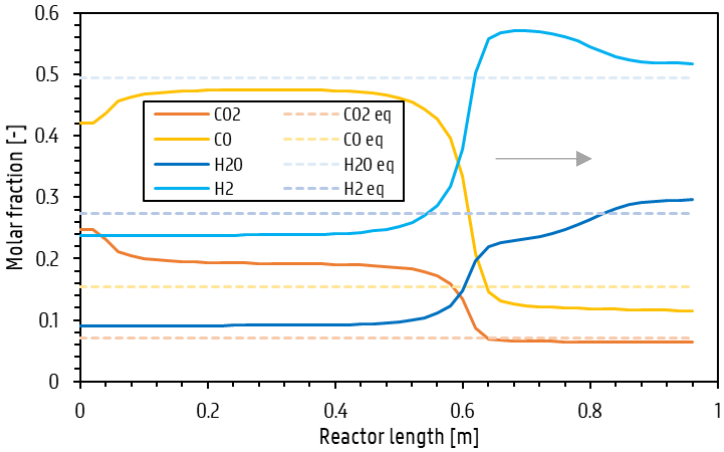

Figure 8-8: Gas phase composition profile as function of reactor length after 240 s in reducer regime with thermodynamic equilibrium composition lines.

The results obtained during the reducer step are not as accurate for the redox reactions with iron with respect to the expected theoretical equilibrium values due to the simulation input values; i.e. a relative low steepness factor and mass transfer coefficient. The simulation is, however, able to identify the re-oxidation of iron during the reducer regime, which is important with regard to the performance of the whole process.

8.3.2. Oxidizer regime

After the reducer step is completed, the feed valve is fully closed and the product pressure is put at 1 *bar*. In this way, the pressure inside the bed decreases, thereby letting the oxidizer regime take place with extract product withdrawal at the top of the reactor: i.e. co-current to the feed. Although the reducer step should have finished after 547 *s,* the oxidizer step starts from 897 *s* because else the simulation would not run. Consequently, the amount of reduced iron present in the bed is lower. The oxidizer step continues until 1008 *s*. The obtained trends and performance metrics are expected to remain valid for the other case as well.

At the end of the reducer step and thus start of the oxidizer step, two regions in the bed can be differentiated; at the beginning of the reactor a first region in which $CaCO_3$ and FeO is present and upward from that region, a second region in which $CaCO_3$ and Fe is present.

The pressure decrease in the bed allows for calcination to take place in the second region of the bed, thereby increasing the $CaCO_3$ conversion as can be seen in the conversion profile in Figure 8-9. The produced CO_2 is converted instantly to CO by re-oxidizing Fe, thereby increasing the conversion of Fe in the bed. It can thus be seen that both calcination and

reoxidation of iron takes place simultaneously because of their enhancing effect, as expected. During the continuation of the oxidizer step, more $CaCO_3$ is calcined and more Fe is oxidized as shown Figure 8-9. At the end of the oxidizer step – after 1008 *s* – it can be seen that at the end of the bed all $CaCO_3$ is calcined, whereas further down in the bed part of the $CaCO_3$ remains. This profile can also be generated by the extract product acting as a purge gas, thereby enhancing calcination. For Fe no full conversion is achieved anywhere in the bed. In addition to the iron assigned to the H_2/H_2O reaction that could not be used for the CO/CO_2 reaction with iron, part of the iron assigned to the CO/CO_2 reaction remains unoxidized as well. The latter is highly likely due to a faster and bigger release of CO_2 due to calcination and a slower and less big uptake of CO_2 by the oxidation of Fe. Consequently, full conversion of $CaCO_3$ is reached first from which the released CO_2 can not be completely used to further oxidize the remaining Fe.

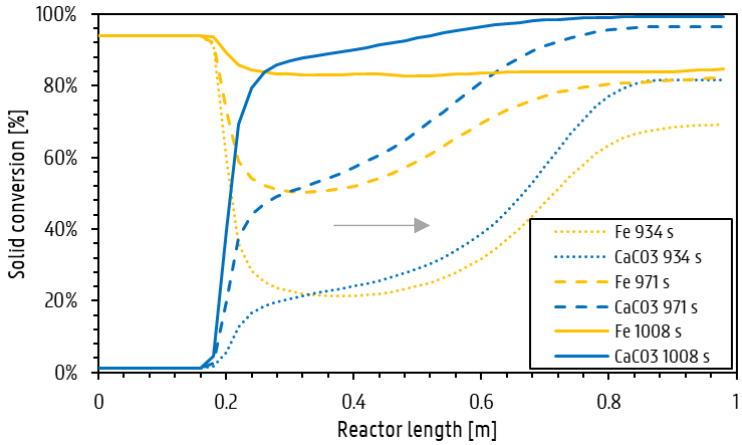

Figure 8-9: Dynamic behavior in reactor during oxidizer regime at 1170 K and 1 bar at 943 s, 971 s and 1008 s: solid conversion profile of CaO and FeO as function of reactor length.

In the first region, however, no calcination occurs because there is no Fe present to keep driving the calcination reaction. Moreover, due to the momentum balance, the pressure drop generated in the bed also yields a higher pressure in the beginning of the bed. Therefore, the partial pressure of CO_2 remains too high in the first region as confirmed by the CO_2 pressure profile in Figure 8-10. Consequently, there is no conversion of $CaCO_3$ in the first region as can be seen Figure 8-9. This implies that all the reduced iron that is lost by re-oxidation in the reducer regime makes that the CO_2 captured by the CaO in the same region cannot be used to produce CO_2. It thus needs to be removed in a following purge step. It is, however, beneficial for the extract product purity that the $CaCO_3$ in the beginning of the bed doesn't calcine, as it would dilute the product with CO_2.

During the oxidizer regime, 89% of the Fe assigned to the reaction of CO/CO_2 is oxidized to FeO and 74% of the total amount of $CaCO_3$ is calcined to CaO. The latter only differs 2% from

the fraction of $CaCO_3$ present together with Fe after 897 *s* in the reducer step. Thus it can be concluded that all $CaCO_3$ in the second region of the bed is calcined.

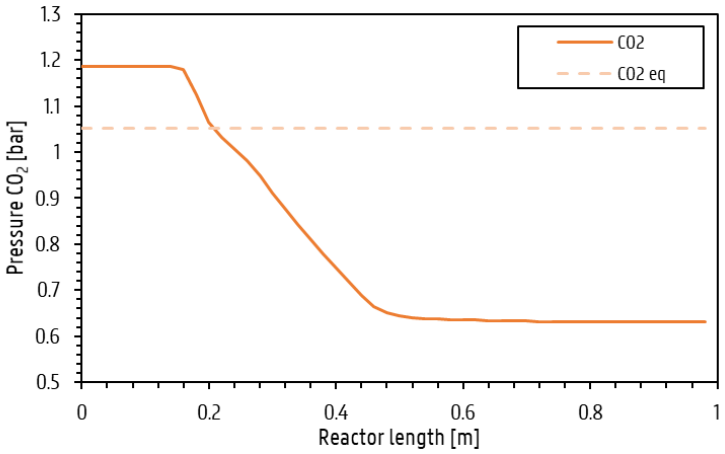

Figure 8-10: Pressure profile in reactor during the oxidizer regime at 1170 K and 1 bar at time 1008 s.

The composition profile in Figure 8-11 shows that in the second region the released CO_2 is instantly converted to CO according to the equilibrium of the oxidation of Fe with CO_2. As only CO_2 is released in this step, the H_2 and H_2O present are pushed out.

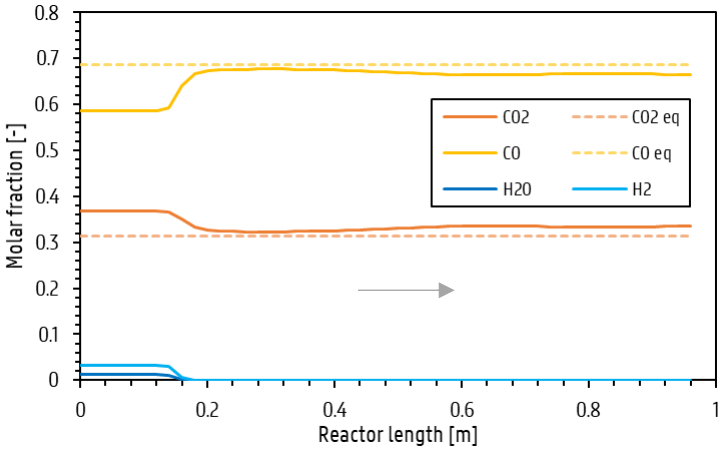

Figure 8-11: Dynamic behavior in reactor during oxidizer regime at 1170 K and 1 bar at 943 s, 971 s and 1008 s: Gas phase composition profile as function of reactor length. Arrow indicates direction of flow.

The obtained equilibrium composition of the simulation yields, however, a slightly higher CO_2 molar fraction in the extract than expected. A molar fraction of 0.665 and 0.335 for CO and CO_2 respectively are obtained, while the equilibrium composition is 0.687 and 0.313 respectively. This is due to the unbalanced amount of $CaCO_3$ and Fe present in the bed, as the solid composition of the bed consists of 55 *wt%* calcium and 45 *wt%* iron. Consequently, there is a large amount of CO_2 that is released while there is not enough Fe present to oxidize

it. Therefore, a slightly increased CO_2 fraction can be seen. The higher CO_2 molar fraction can also be due to the decreased steepness factor.

A counter-current self-purge is also performed, but indicated inferior extract product purity. The latter is due that the calcination of the $CaCO_3$ present in the beginning of the bed dilutes the extract composition with CO_2 because there is no Fe present to produce CO. An extract composition with 58.7 mol% CO and 41.3 mol% CO_2 is obtained. Consequently, a counter-current self-purge is not recommended because of poor product purity.

The simulation indicates that a co-current self-purge can be used in the oxidizer regime. Furthermore, the simulation shows that an extract product with high purity of CO can be obtained using a co-current self-purge.

8.3.3. Purge

At last a purge step is performed which has the goal to regenerate the two solids inside the bed: $CaCO_3$ should be fully calcined to CaO and Fe should be fully oxidized to FeO to be able to restart the cycle. The purge gas is a mixture that can either be one of the product streams, i.e. the raffinate or the extract, or an inert gas. The purge starts from 1008 *s* and takes until 1651 *s*.

The purge step is preferably performed co-current with respect to the feed in the reducer regime. In this way, the $CaCO_3$ still present in the first region of the bed will be calcined thereby producing CO_2. Subsequently, this CO_2 will oxidize the Fe when it reaches the second region of the bed. In case a counter-current purge is used, there will be no CO_2 released that re-oxidizes the iron as the feed goes over the second region first.

In this simulation, part of the raffinate product stream is selected as the ideal candidate for the purge; its high pressure, low CO_2 partial pressure and being regarded more as a waste product than a main product makes it suitable as a purge stream.

The dynamic behavior of the conversion profile during the purge step clearly shows that the $CaCO_3$ is calcined in the first region, whereas the Fe in the second region is instantly oxidized as shown in Figure 8-12. Again, the iron assigned to the H_2/H_2O cannot be re-oxidized with the CO_2 and thus part of the Fe can be seen the remain unoxidized. During the further continuation of the purge step, part of the CO_2 released during calcination is observed to be adsorbed on CaO in the second region. Consequently the $CaCO_3$ peak can be seen moving upward in the bed following the direction of the purge flow. However, the calcination effect still remains

greater than the re-carbonation and thus eventually total calcination is reached. After 1651 *s* all $CaCO_3$ and Fe are regenerated.

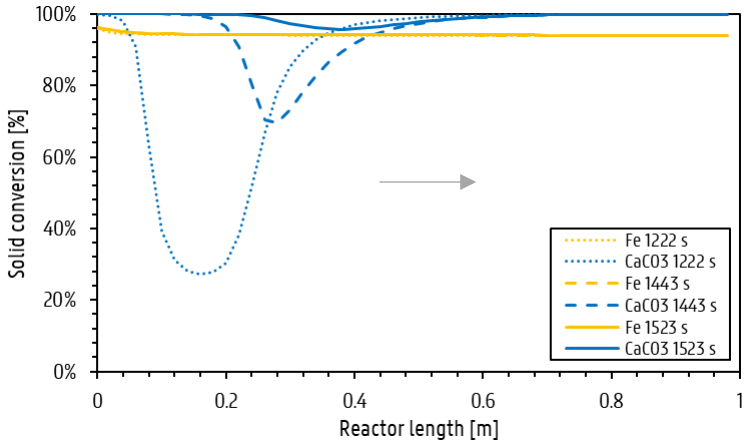

Figure 8-12: Conversion profile in reactor during the purge step at 1170 K and 1 bar at 1222, 1443 and 1523 s.

The composition profile in the reactor during the purge step shows that before the $CaCO_3$ conversion peak the raffinate product composition is present, which acts as the purge stream. Behind the $CaCO_3$ conversion peak the mixture mostly contains CO_2 as it is released by the calcination reaction. As the purge product purity is still high in CO_2, recycle to the reformer feed can be proposed. In this case, however, less fresh CO_2 will be utilized overall.

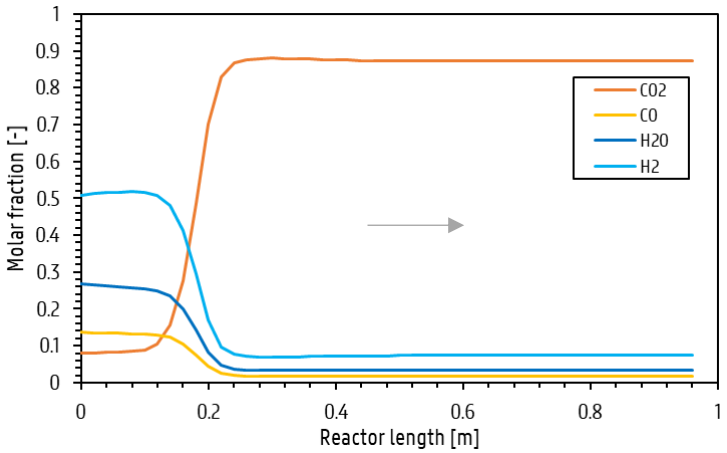

Figure 8-13: Composition profile in reactor during the purge step at 1170 K and 1 bar at time of 1443 s.

At the end of the purge cycle it can be seen that 100% of the $CaCO_3$ is calcined and that 100% of the iron assigned to the CO/CO_2 reaction is reoxidized. The 6% of the maximal loading capacity of iron that is assigned to the H_2/H_2O reaction remains unoxidized. In total 5% of the raffinate product is used as a purge stream. The simulation of the purge step thus shows its ability to fully regenerate the bed.

8.3.4. Full cycle performance

The simulation shows to satisfy the purpose of this work; i.e. being able to do a conceptual analysis and getting insights in the dynamics of the whole process at 1170 *K*. The performance of the four steps in the cycle – based on the reducer step to last 467 *s* – can be summarized as follows:

I. **Pressurization:** The simulation is able to increase the pressure from 1 to 15 *bar*.
II. **Reducer regime:** 100% CaO conversion is achieved, whereas only 80% of reduced iron is obtained. The remaining 20% of iron is reoxidized because of the oxidizing nature of the feed when the calcium is saturated. 73% of CO is converted to CO_2 and 91% of CO_2 from the feed and produced from CO is retained in the bed in the form of $CaCO_3$. The product composition of the raffinate is 1 *mol%* of CH_4, 11 *mol%* of CO, 6% *mol%* of CO_2, 52 *mol%* of H_2 and 30 *mol%* of H_2O.
III. **Oxidizer regime:** a self-purging concept can be used in the oxidizer regime. 81% of the calcium is calcinated, whereas in total 87% of the iron is re-oxidized at the end of the oxidizer step. In total 66.5 *mol%* of the released CO_2 from calcination is converted to CO, thereby yielding an extract product purity of 66.5 *mol%* CO and 33.5 *mol%* of CO_2.
IV. **Purge:** The remaining 19% of $CaCO_3$ is regenerated, whereas only 7% of Fe is further oxidized. This is because the other 6% can not be reoxidized due to its assignment to the H_2/H_2O reaction.

The overall performance metrics based on the total amount of CO and CO_2 are interesting as they represent the performance with respect to the main product of the process. In total 75% of the amount of CO_2 and CO combined in the feed are stored in the bed in the form of $CaCO_3$ during the reducer regime. 81% thereof is recovered as extract product with a composition of 66.5 *mol%* CO and 33.5 *mol%* of CO_2. Consequently the overall conversion efficiency of the feed to the extract product is 60% in this simulation. This is significantly lower than the theoretical 86% conversion efficiency as calculated from equilibrium due to two main reasons: (i) because of the breakthrough of the feed at the end of the reducer regime, the total amount of CO and CO_2 retained in the bed decreases significantly, and (ii) the increased losses in extract recovery caused by the reoxidation of iron in the reducer regime. The percentage of re-oxidized iron during the reducer regime is directly related to the conversion efficiency. Consequently, this should be minimized as much as possible.

The simulation shows that it is able to perform all four steps of the cycle and consequently give insight in the dynamics of the combined chemical looping process with a pressure swing operation. The obtained results are not as accurate with respect to the calculated

thermodynamic equilibria of the system, however, they are still within acceptable limits and thus the simulation is also able to give reasonable results. The deviation of the calculated equilibrium can be assigned to too low steepness factors used in the sigmoid functions and too low mass transfer coefficients used in the simulation. The choice of both input values is a compromise of letting the simulation reach convergence and obtaining accurate results. One important drawback of the applied methodology in the simulation is that the reduced iron with H_2 can not be reoxidized by CO_2 in the oxidizer regime.

8.4. Optimization potential of combined chemical looping process

In this section the combined chemical looping process is further optimized by tackling the key performance issues found in the simulation of Section 8.3. The breakthrough of CO and CO_2 and the fraction of iron re-oxidized during the reducer regime are determined to be the main factors that affect the feed conversion efficiency to the extract product. Whereas the extract purity is affected by the amount of carbonated calcium and iron present together in the oxidizer regime.

It is known that the breakthrough of the feed can be directly minimized by solely increasing the mass transfer coefficient as discussed previously. Performing solely this change would intuitively increase the performance of the cycle as the model will yield more accurate results with respect to the simulation goal of reaching instantaneous equilibrium. This would, however, not provide additional insight regarding which parameters could affect the cycle's performance. Consequently, the effect of only increasing the mass transfer coefficient is not performed.

The effect of three chosen process parameters on the cycle's performance are evaluated in the coming sections; i.e. the solid's composition loaded in the bed, the feed pressure in the reducer regime and the solid's distribution. A sensitivity analysis with the latter three process parameters on the fraction of iron that is re-oxidized, the fraction of CO and CO_2 in the feed that breaks through during the reducer regime and the amount of carbonated calcium and iron present together in the oxidizer regime will be performed. The simulations are only run during the reducer regime because of convergence issues during the depressurization step.

The mass transfer coefficients and steepness factor are increased to 1 $m.s^{-1}$ and 500 respectively, in order to obtain more accurate results with respect to equilibrium and consequently make more profound conclusions. The latter is no problem when simulating solely the reducer regime.

8.4.1. Effect of solid composition

In this section, the effect of the solid composition of the bed on the performance of the process is investigated. During the simulation, the operating conditions are kept constant at 1170 *K* and 15 *bar* and consequently the fraction of CO and CO_2 that breaks through is the same for all cases in this sensitivity as it is determined by the thermodynamics of the system. The effect of the solid composition on the other two main challenges, i.e. the re-oxidation of iron in the reducer regime and the uneven amount of carbonated calcium and reduced iron present in the oxidizer regime, will thus be investigated.

A better understanding of the system with the two combined solids at its corresponding operating conditions can be found by looking at two specific system properties: the oxidizing and the reducing ratio.

An "*oxidizing ratio*" represents the total moles of oxidized iron per mole of CO_2 to reach the exact equilibrium composition of its reaction, as presented in Eq. (8.1). During the oxidizer regime, this ratio represents the amount of reduced iron required per mole of $CaCO_3$ to achieve the equilibrium composition in the extract in case the calcium sorbent is fully calcined. This ratio is equal to the equilibrium molar fraction of CO of the CO/CO_2 reaction with iron and thus depends solely on temperature.

$$Oxidizing\ ratio = \left[\frac{Mol\ of\ FeO\ produced}{Mol\ of\ CO_2}\right]_{eq} = \left[\frac{Mol\ of\ Fe\ required}{Mol\ of\ CaCO_3}\right]_{eq} \quad (8.1)$$

A "*reducing ratio*" can also be determined that represent the total moles of reduced iron per mole of carbonated calcium during the reducer regime as presented in Eq. (8.2)

$$Reducing\ ratio = \left[\frac{Mol\ of\ Fe\ produced}{Mol\ of\ CaCO3\ produced}\right]_{eq} \quad (8.2)$$

This ratio depends on both pressure and temperature. Ideally, the oxidizing ratio and the reducing ratio are equal, so that the carbonated calcium and the reduced iron obtained in the reducer regime, yield exactly the equilibrium composition in the oxidizer. In case the reducing ratio is smaller than the oxidizing ratio, not enough reduced iron is formed during the reducer regime to obtain the equilibrium composition in the oxidizer regime and consequently the extract product will be diluted with CO_2 in case all calcium is calcined. In case the reducing ratio is greater than the oxidizing ratio, not enough carbonated calcium is present in the oxidizer regime, thereby leading to only a fractional conversion of the reduced iron. Table 8-4 indicates that for a pressure of 15 *bar* and a temperature lower than 1050 *K* the oxidizing ratio is smaller than the reducing ratio and *vice versa* for temperatures higher than 1050 *K*. Consequently, for the operating conditions in this work – i.e. 15 *bar* and 1170 *K* – there is an inherent mismatch

between the oxidizing and reducing ratio. Therefore, it is expected that the reducer regime is prone to producing less reduced iron than is required in the oxidizer regime and consequently that the extract product will be off its equilibrium composition in case total calcination takes place.

Table 8-4: Oxidizing and reducing ratio from thermodynamic calculations at 15 bar for 950, 1050 and 1170 K.

[mol reduced iron/mol carbonated calcium]	950 K	1050 K	1170 K
Oxidizing ratio	0.60	0.65	0.69
Reducing ratio	0.63	0.65	0.66

In this section, the effect of a chosen solid composition relative to the reducing ratio and oxidizing ratio of the system is investigated. Because of the methodology applied in this work all ratios are based on the iron corresponding to only the CO/CO_2 reaction, as there is no interaction with the iron for the H_2/H_2O reaction. The corresponding reducing ratio for the operating conditions of 1170 *K* and 15 *bar* is then 0.62. Seven different solid compositions are used in this sensitivity that all yield a different ratio of iron and calcium relative to the reducing and oxidizing ratio; two ratios greater than the oxidizing ratio, a ratio equal to the oxidizing ratio, a ratio between the oxidizing and reducing ratio, a ratio equal to the reducing ratio and two ratios smaller than the reducing ratio as shown in Table 8-5. In this way, the behavior of the bed can be linked to regimes that depend on the two system properties; i.e. the oxidizing and reducing ratio.

Table 8-5: Simulation results of the effect of different input ratios of iron and calcium on the performance parameters at the end of the reducer regime.

	OR = 0.687				**RR = 0.619**		
	R_1 >> OR	**R_2 > OR**	**R_3 = OR**	**OR>R_4>RR**	**R_5 = RR**	**RR > R_6**	**RR >> R_7**
R_i iron/calcium input	0.945	0.773	0.687	0.657	0.619	0.585	0.236
wt% calcium	0.500	0.550	0.579	0.590	0.600	0.610	0.800
wt% iron	0.500	0.450	0.421	0.410	0.400	0.390	0.200
Final Fe [kmol]	1.132	1.215	1.246	1.206	1.160	1.113	0.541
Final FeO [kmol]	0.599	0.302	0.152	0.148	0.139	0.131	0.055
Final CaCO3 [kmol]	1.825	1.958	2.012	1.957	1.870	1.794	0.884
Final Fe/CaCO3	0.621	0.620	0.619	0.616	0.620	0.620	0.612
% Reduced iron	65%	80%	89%	89%	89%	89%	91%
% Carbonated calcium	100%	100%	99%	95%	89%	84%	35%

Table 8-5 presents the results of all the different solid compositions. Herein, for all the different iron and calcium ratios, the ratio of the final amount of reduced iron and carbonated calcium are approximately the same and equal to the reducing ratio. This means that independent of the solid composition used in the bed, the reducing ratio – and thus the temperature and pressure – determines the final ratio of Fe and $CaCO_3$ in the bed.

The fraction of reduced iron and carbonated calcium at the end of the reducer regime are, however, dependent on the input ratio of iron and calcium. On the one hand, it is observed that the fraction of reduced iron increases significantly with decreasing solid input ratio until it is equal to the oxidizing ratio. Thereafter, the fraction of reduced iron remains constant at a maximum value of approximately 89%. On the other hand, the fraction of carbonated calcium remains constant at approximately 100% for input ratios higher and equal to the oxidizing ratio. Whereas for lower input ratios, the fraction of carbonated calcium decreases significantly. These observations indicate that the initial input ratio of iron and calcium significantly affects on the operation of the reducer regime. An input ratio equal to the oxidizing ratio yields both the highest fraction of reduced iron and carbonated calcium at the end of the reducer regime.

The obtained fraction of reduced iron and carbonated calcium depends on the limiting solid reactant with respect to the oxidizing ratio as is shown by Table 8-6. On the one hand, in case calcium is the limiting solid reactant or if there is none, the fraction of reduced iron is determined by the potential of the system to reduce iron with the limiting amount of calcium present, i.e. input ratio and the reducing ratio. For this case, the fraction of carbonated calcium is 100%, as it is the limiting reactant and thus fully consumed. On the other hand, in case iron is the limiting solid reactant, the fraction of reduced iron is determined by the oxidizing potential and the reducing potential of the system, i.e. the oxidizing ratio and the reducing ratio. Consequently, the fraction of reduced iron has a maximal value depending on both system properties. For this case, the fraction of carbonated calcium is determined by the potential of the system to carbonate calcium with the limiting amount of iron present, i.e. the input ratio and the oxidizing ratio.

Table 8-6: Comparison of input ratio R_i with oxidizing ratio (OR) and reducing ratio (RR) to obtain theoretical fraction of reduced iron and carbonated calcium at the end of reducer regime.

% Reduced iron % Carbonated calcium	OR = 0.687				RR = 0.619		
Regimes	**R_1 >> OR**	**R_2 > OR**	**R_3 = OR**	**OR>R_4>RR**	**R_5 = RR**	**RR > R_6**	**RR >> R_7**
R_i iron/calcium input	0.945	0.773	0.687	0.657	0.619	0.585	0.236
RR/OR	90%	90%	90%	**90%**	**90%**	**90%**	**90%**
RR/R_i	**65%**	**80%**	**90%**	94%	100%	106%	262%
R_i/OR	138%	113%	100%	**96%**	**90%**	**85%**	**34%**
OR/OR	**100%**	**100%**	**100%**	100%	100%	100%	100%
Limiting reactant (OR)	Calcium	Calcium	/	Iron	Iron	Iron	Iron

Besides the fraction of reduced iron at the end of the reducer regime, the other challenge of the system is an uneven amount of carbonated calcium and reduced iron present together. Figure 8-14 presents the solid conversion and corresponding loading profiles that show the distribution of the carbonated calcium and reduced iron at the end of the reducer step for the same input ratio of calcium and iron as in Table 8-5.

(A) (B)

R1

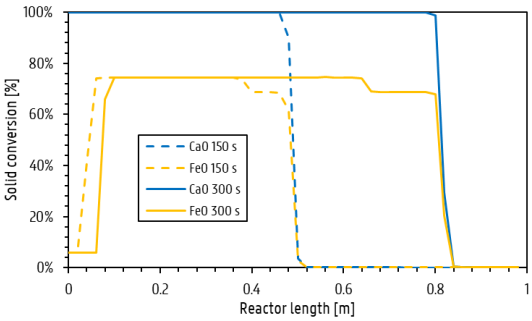

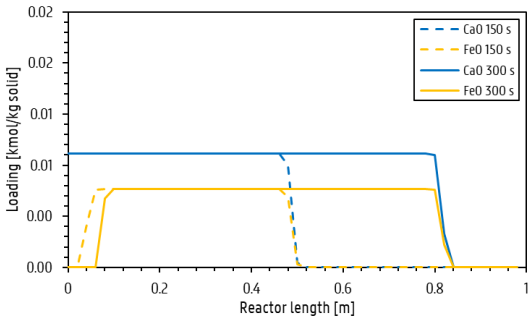

R2

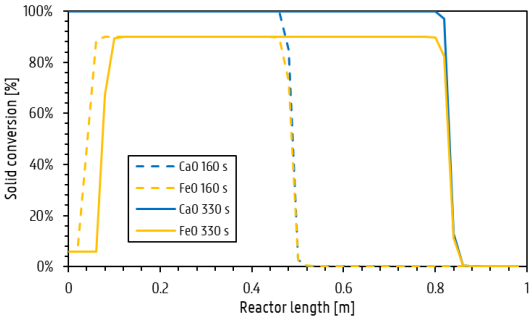

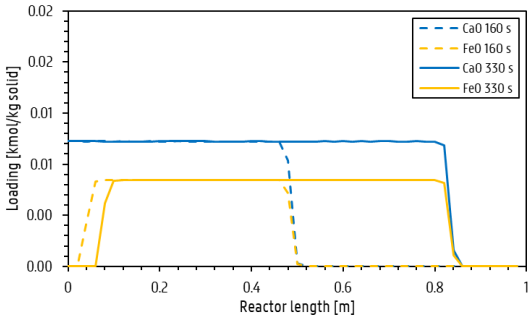

R3

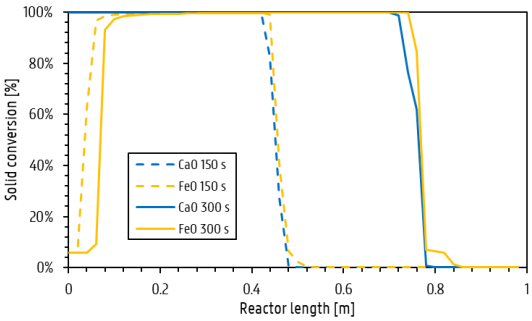

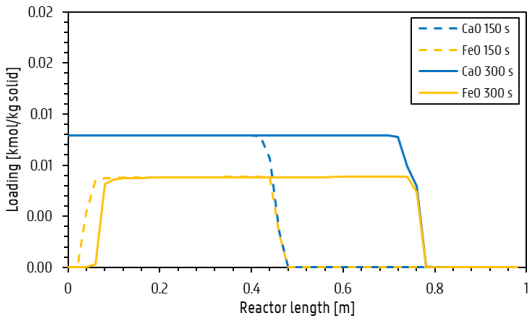

R4

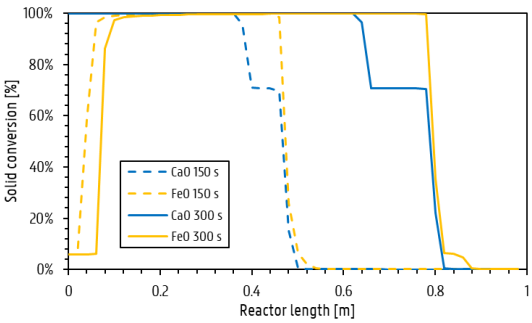

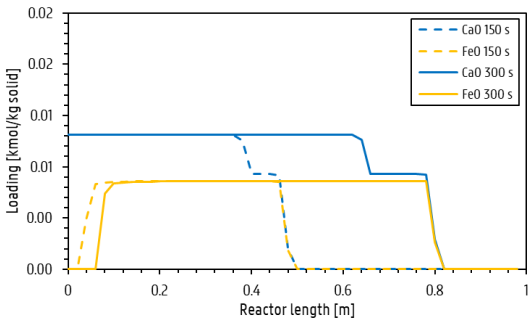

R5

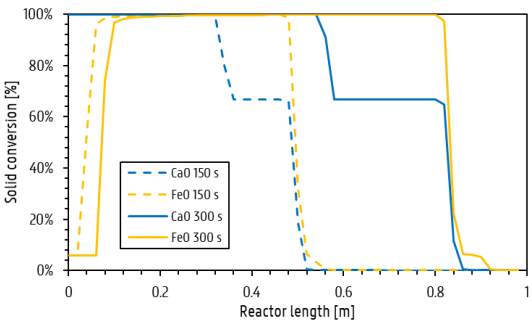

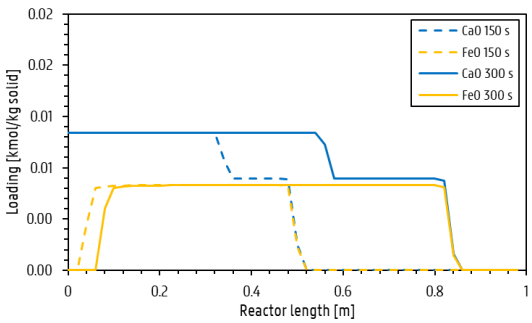

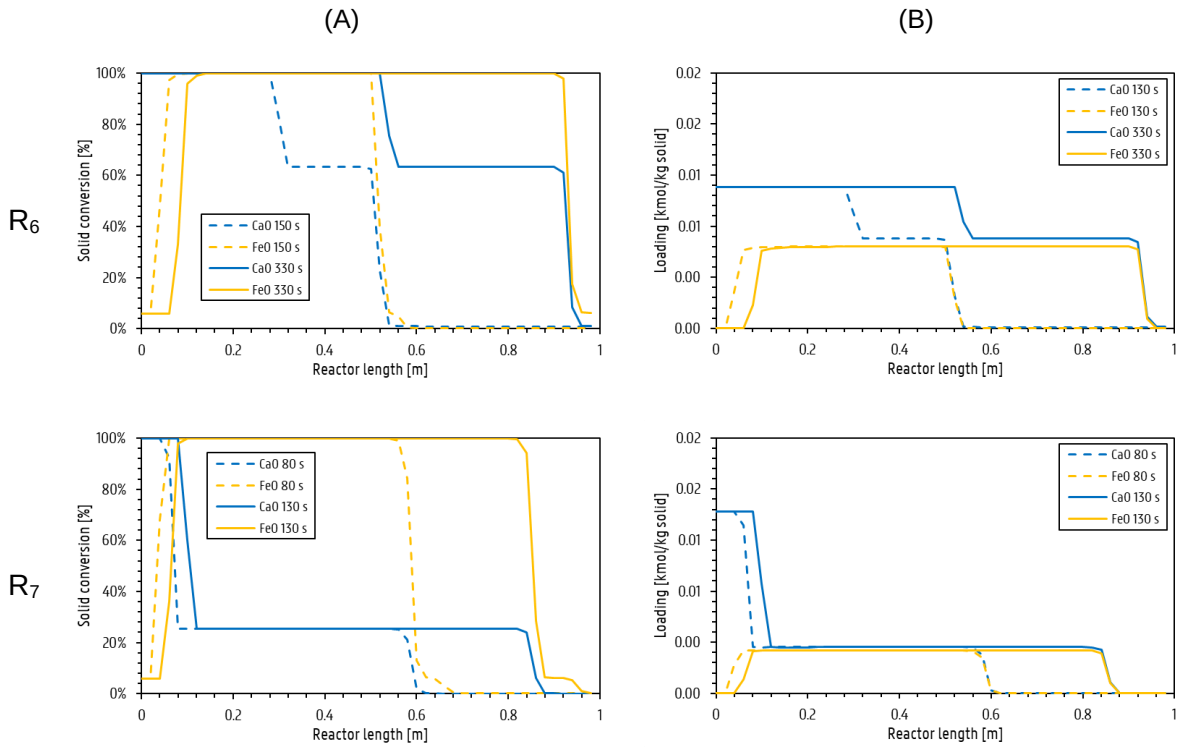

Figure 8-14: Dynamic behavior of (A) conversion profiles and (B) corresponding loading profiles in the reactor for all seven input ratios of iron and calcium arranged from high to low: $R_1 > R_2 > R_3 = OR > R_4 > R_5 = RR > R_6 > R_7$.

In all cases the enhancing effect of the combination of the solids makes that the iron and the calcium conversion front stick together as it moves through the bed. However, the carbonated calcium and reduced iron are not evenly distributed for all cases. Again, the different dynamics of the system can be assigned to the limiting solid reactant.

In case calcium is the limiting reactant with respect to the oxidizing ratio, i.e. for input ratios R_1, R_2 and R_3, the carbonated calcium and reduced iron can be seen evenly distributed along the reactor. Because calcium is the limiting reactant, the amount of iron at each position in the reactor is determined by the oxidizing ratio. Consequently, the ratio at each position of the reactor – except for the re-oxidized part in the front – equals that of the oxidizing ratio. The latter is optimal for the oxidizer regime to obtain the equilibrium composition at full calcination. Moreover, for input ratio equal to the oxidizing ratio (R_3), 100% conversion is achieved in both calcium and iron and thus both solids are completely utilized. Whereas with increasing input ratios (R_1 and R_2), the conversion of iron decreases as it is more limited by calcium.

In case iron is the limiting reactant with respect to the oxidizing ratio – i.e. for input ratios R_4 until R_7 – an uneven distribution of the carbonated calcium and reduced iron can be seen. Now two distinct conversion fronts can be seen. The first front moves the fastest in the bed and has full conversion of iron while calcium only reaches partial conversion. The latter is because iron is the limiting reactant in this case. The second front moves the slowest in the bed in which calcium reaches full conversion. This is because the calcium is not yet saturated before the

first conversion front and thus it captures CO_2 until reaching full conversion. The ratio of carbonated calcium and reduced iron is equal to that of the input ratio in front of the second front. Whereas after the second front, the ratio is approximately equal. The latter is because the CO_2 from the feed is already taken out and thus there is only the further combined the enhancing effect of both solids. For decreasing input ratios, it can be seen that the higher adsorption capacity of calcium makes that there is a build-up of carbonated calcium in front of the reactor, whereas the rest of the reactor contains almost equimolar amount of carbonated calcium and reduced iron. Consequently, a higher fraction of carbonated calcium is present together with the re-oxidized iron and can thus not be used in the oxidizer regime. The equimolar amount of carbonated calcium and reduced iron would lead to only a fractional conversion of the iron. Therefore, input ratios higher than the oxidizing ratio are detrimental for the performance of the whole process.

The oxidizing ratio is determined to be the optimal input ratio for the performance of the reactor. It yields the maximum fraction of reduced iron and equal distribution of the carbonated calcium and reduced iron. Furthermore, the ratio of the latter two solids is equal to the oxidizing ratio which is optimal for obtaining an extract composition equal to the equilibrium composition.

8.4.2. Effect of feed pressure

In this sensitivity, the effect of the feed pressure on the dynamics of the reducer regime in the process is evaluated. The temperature is restricted to the operating temperature determined for the oxidizer regime, consequently only the pressure can be changed. A solid composition of 45 *wt%* iron and 55 *wt%* calcium is used for all cases in this sensitivity.

In Section 8.3.1 it is observed that when the calcium is fully saturated, the reduced iron is re-oxidized in the beginning of the reactor bed. The feed pressure in the reducer regime is known to be the driving force for the carbonation reaction. Consequently, by decreasing the feed pressure in the reducer regime, the driving force for carbonation is lowered. In this way, the saturation of the calcium is expected to be postponed and less iron is re-oxidized.

Five feed pressures are used in the sensitivity analysis; i.e. 20, 15, 10, 7 and 5.5 *bar*. The solid composition of 45 *wt%* iron and 55 *wt%* calcium yields an input ratio of calcium and iron lower than the oxidizing ratio and thus the system is operated in the calcium limited region as discussed in Section 8.4.1. Consequently, all simulations are run until all calcium is carbonated in the end of the reactor bed. Furthermore, all carbonated calcium and reduced iron remain evenly distributed along the reactor. The effect on the fraction of CO and CO_2 retained in the bed and the fraction of reduced iron at the end of the reducer regime can then be further

translated to an overall conversion efficiency of the feed to the extract product in a simplified manner; it is assumed that the fraction of the reduced iron at the end of the reducer regime can be completely used during the oxidizer regime. The multiplication of the fraction of CO and CO_2 of the feed retained in the bed and the fraction of reduced iron yields an estimate of the overall conversion efficiency of the feed to the extract product, shown in Eq. (8.3).

$$Feed\ conversion\ efficiency = \left(1 - \frac{mol\ (CO\ +\ CO_2)_{raffinate}}{mol\ \ (CO\ +\ CO_2)_{feed}}\right) \cdot \left(\frac{mol\ Fe}{mol\ iron}\right)_{reducer} \tag{8.3}$$

This will serve as a good indication of the effect of the feed pressure on the performance of the process. Table 8-7 represents the obtained performance metrics for all different feed pressures in the reducer regime.

Table 8-7: Performance metrics obtained via simulations of the reducer regime for feed pressures of 20, 15, 10, 7 and 5.5 bar.

Feed pressure [bar]	**20**	**15**	**10**	**7**	**5.5**
Total reducer time [s]	335.0	420.0	632.0	1157.0	3521.0
Total amount of feed [kmol]	3.2	3.4	3.9	5.3	20.3
Fraction CO+CO_2 retained	90%	86%	76%	56%	24%
Fraction reduced iron	82%	81%	80%	77%	62%
Feed conversion efficiency	74%	70%	61%	43%	15%

It can be seen that with decreasing feed pressure, the total time taken to complete the reducer step increases. Moreover, with decreasing feed pressure an increased amount of feed is required to reach completion of the reducer step. The latter observation can be explained by looking at the change in the amount of iron that is reduced and the amount of calcium that is carbonated for the different feed pressures. Table 8-8 represents the calculated change of moles of the feed to reach thermodynamic equilibrium for CO and CO_2 in the combined solid system. With decreasing feed pressure, the amount of reduced FeO and carbonated CaO decreases substantially. The latter is due to less CO_2 being adsorbed on the calcium at lower pressures, thereby decreasing the amount of iron that needs to be reduced with CO to compensate for the CO_2 adsorption. In this way, a less reducing and carbonating feed mixture is created as the feed pressure decreases and thus more feed is required to reach completion of the reducer step as can be seen from the simulation results. As a consequence, more time

is required because the flowrate is restricted by the pressure drop over the bed.

Table 8-8: Calculated change in moles of reformer outlet as feed to reach thermodynamic equilibrium for feed pressures of 20, 15, 10, 7 and 5.5 bar.

Feed pressure [bar]	**20**	**15**	**10**	**7**	**5.5**
Mol FeO reduced by CO per mol feed	0.374	0.354	0.304	0.209	0.063
Mol CaO carbonated per mol feed	0.601	0.572	0.499	0.360	0.148

Furthermore, it is observed in Table 8-7 that with decreasing feed pressure the fraction of CO and CO_2 from the feed that is retained in the bed decreases considerably. As the latter is one of the main factors affecting the performance of the process, the feed pressure will significantly impact performance of the process. At lower feed pressures, less carbonation will take place accompanied with less CO that is converted to CO_2 and thus it is expected that the raffinate product obtained during the reducer step is richer in CO and CO_2 as the feed pressure decreases. The latter is confirmed by looking at the raffinate composition of the simulations in Table 8-9, which approximate the calculated thermodynamic equilibrium well because of the high steepness factors used in the simulation.

Table 8-9: Raffinate composition in reducer regime obtained from simulation and thermodynamic equilibrium calculations for feed pressure of 20, 15, 10, 7 and 5.5 bar.

	Raffinate composition: simulation & *thermodynamic equilibrium* [mol%]									
Component	**20 bar**		**15 bar**		**10 bar**		**7 bar**		**5.5 bar**	
CH_4	0.01	*0.01*	0.01	*0.01*	0.01	*0.01*	0.00	*0.01*	0.00	*0.00*
CO	0.11	*0.12*	0.15	*0.15*	0.22	*0.23*	0.31	*0.33*	0.40	*0.42*
CO_2	0.05	*0.05*	0.07	*0.07*	0.10	*0.11*	0.15	*0.15*	0.19	*0.19*
H_2	0.53	*0.53*	0.50	*0.49*	0.43	*0.42*	0.34	*0.33*	0.26	*0.25*
H_2O	0.30	*0.29*	0.28	*0.27*	0.24	*0.23*	0.19	*0.18*	0.15	*0.14*

Additionally, the simulations show that the fraction of reduced iron at the end of the reducer step increases with increasing pressure. The difference between feed pressures of 20, 15 and 10 *bar* are, however, only minor. The simulations are run in the calcium limiting region and consequently the fraction of reduced iron is determined by the input ratio of iron and calcium and the reducing ratio of the system. As the input ratio is fixed, the fraction of reduced iron only depends on the reducing ratio. In Table 8-10 a pressure dependency of the reducing ratio can clearly be seen. The fraction of reduced iron from the simulation is approximately equal again to the ratio of the reducing ratio and input ratio, following the same reasoning as in Section 8.4.1.

Table 8-10: Reducing ratio and corresponding calculated fraction of reduced iron compared to simulation results for feed pressures of 20, 15, 10, 7 and 5.5 bar.

	Input ratio iron/calcium = 0.773				
Feed pressure [bar]	**20**	**15**	**10**	**7**	**5.5**
Reducing ratio [mol Fe/mol $CaCO_3$]	0.623	0.620	0.610	0.580	0.427
% Reduced iron simulation	81%	80%	79%	75%	55%
Reducing ratio/input ratio	82%	81%	80%	77%	62%

It can be seen that the reducing ratio increases with increasing feed pressure and consequently the fraction of reduced iron increases as well. For lower feed pressures, a higher fraction of the iron will thus be re-oxidized compared to higher feed pressures. Operating at higher feed pressures is thus beneficial to minimize the amount of iron that is re-oxidized. Furthermore, it is observed that there is only a minor difference in the reducing ratio for feed pressures of 20, 15 and 10 *bar*, whereas the difference in the reducing ratio for lower feed pressures is significantly higher. As a consequence, increasing the feed pressure at already high pressures, doesn't yield significantly better results. An explanation is found by looking at the behavior of the equilibrium of the system at different pressures as shown by Figure 8-15 (A)-(C).

(A)

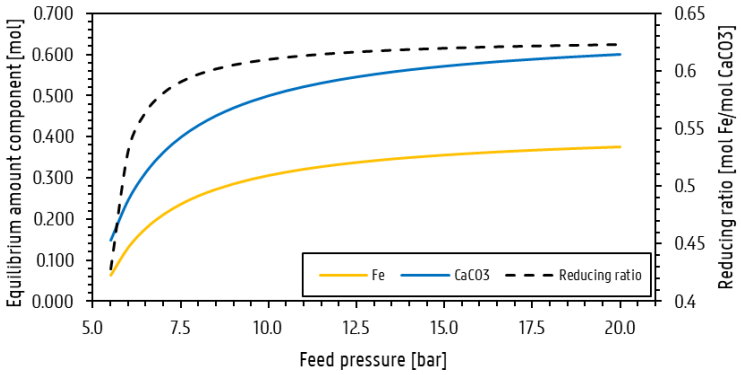

(B)

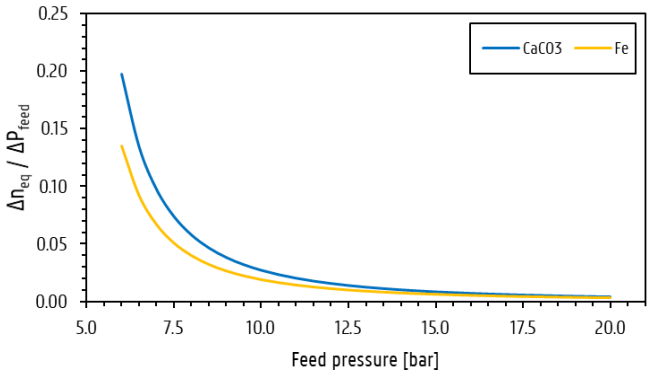

(C)

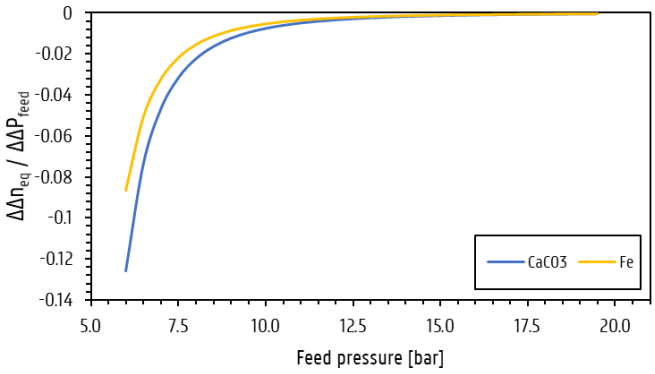

Figure 8-15: (A) Total, (B) first derivative (C) second derivative of equilibrium amount of carbonated calcium and reduced iron at feed pressures between 5.5 and 20 bar.

The total amount of carbonated calcium and reduced iron based on equilibrium calculations – shown in Figure 8-15 (A) – indicates that for increasing feed pressure, both the total amount of carbonated calcium and reduced iron increases. This is expected, as a higher pressure yields a higher driving force for carbonation and consequently also for reduction of iron to take place. The latter can also be seen in Figure 8-15 (B) in which the first derivative of the equilibrium amount of carbonated calcium and reduced iron with respect to the feed pressure remains positive. Furthermore, it can be seen that at higher pressures, the change of the amount of carbonated calcium and reduced iron becomes smaller and approximately equal to zero, as indicated by the first derivative asymptotically approaching zero in Figure 8-15 (B). The second derivative – as shown in Figure 8-15 (C) – indicates that the change of the amount of carbonated calcium decreases faster than the change of the amount of reduced iron. Consequently, the reducing ratio increases with increasing feed pressure as it is the ratio of the amount of reduced iron and carbonated calcium. Moreover, as the second derivative of both solids asymptotically approaches zero at higher pressures, a negligible change in the reducing ratio can be seen at higher pressures.

Because both the fraction of CO and CO_2 retained from the feed and the fraction of reduced iron increases with increasing feed pressure, the feed conversion efficiency increases with increasing pressure as depicted in Table 8-7. A feed pressure of 15 *bar* does not differ that much from a feed pressure of 20 bar in terms of feed conversion efficiency and whilst taking into account the cost considerations accompanied with creating high pressures by the use of compressors, 15 bar is assumed as a considerable trade-off between cost and process efficiency.

8.4.3. Effect of solid distribution: solids in series

In this section, the solids in the bed are distributed in an ideal way that yield no iron re-oxidation during the reducer regime. It is known that the re-oxidation of iron takes place when the calcium sorbent is saturated, thereby letting the feed of the reactor retain its oxidizing nature. In a fully mixed bed of calcium and iron, calcium saturation in the beginning of the bed cannot be avoided because of the high reducing feed that is created, accompanied with a fast utilization of the calcium. An alternating bed with alternating calcium and iron layers can, however, avoid the re-oxidation phenomenon. In this case, calcium and iron are physically separated, thereby avoiding the instantaneous creation of the highly reducing feed and thus avoiding the fast conversion of calcium in the beginning of the bed.

In section 0 the dynamics of alternating layers of calcium and iron indicate that consecutive layers of calcium and iron have a lower degree of solid conversion. The latter is because after each calcium layer, iron always produces an amount of CO_2 from CO equal to 68.7% of the amount of CO_2 that is carbonated in the previous calcium layer, to achieve its equilibrium composition. Consequently, in every subsequent layer of calcium, less CO_2 is carbonated again to achieve its corresponding equilibrium. This successive lower production and consumption of CO_2 makes that less amount of iron and calcium respectively are required to reach equilibrium every subsequent layer, as can be seen in Figure 8-16. The first layer of calcium requires a relative higher amount as the feed contains a lot of CO_2.

Consequently, a reactor bed with successive decreasing amount of calcium and iron – required to reach equilibrium in each layer – can be configured. In this way all layers will have equal conversion rates and reach complete conversion simultaneously at which point the reducer step is stopped. This makes that the calcium is never saturated and thus no re-oxidation of the iron can take place.

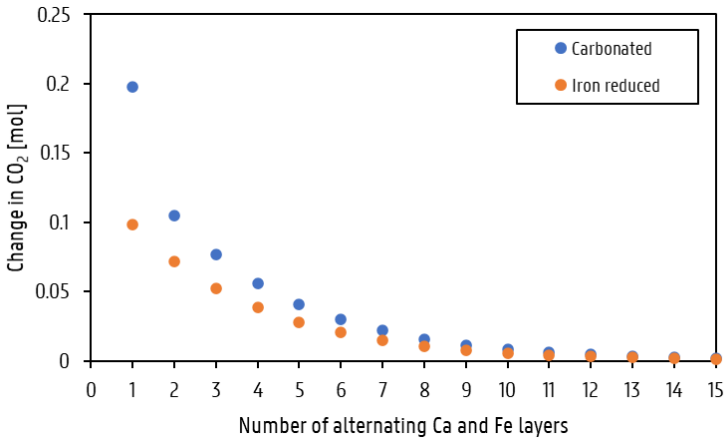

Figure 8-16: Theoretically calculated molar change of CO_2 in subsequent alternating layers of calcium and iron by carbonation and reduced iron in the reducer regime at 1170 K and 15 bar for 1 mol of feed.

Figure 8-16 indicates that after approximately ten alternating layers negligible changes take place because the equilibrium of the total system is almost achieved, therefore a simulation of ten alternating layers of calcium and iron is configured. The length of each layer – at fixed diameter – is calculated to reach total conversion of the bed for 10 *kmol* of feed at 1170 *K* and 15 *bar*. Figure 8-17 depicts the alternating layers of calcium an iron. Because of the lower density of calcium, longer layers are required than iron and at the beginning of the reactor a relatively high amount of calcium is needed because of the high CO_2 fraction in the feed.

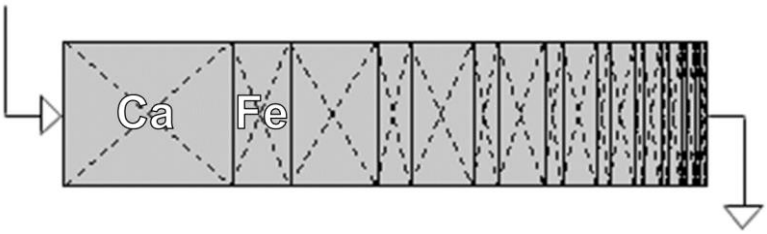

Figure 8-17: Reactor bed with alternating calcium and iron layer in equilibrium amount for each reaction stage.

The solid conversion profiles of the calcium and iron solid in the bed in Figure 8-18 (a) show the equal conversion of all solid layers inside the reactor during the reducer regime. At the end of the reducer step – after 2187 *s* – all solids achieve full conversion as is depicted in Figure 8-18 (b) without any iron that is re-oxidized, as expected. After 10 *kmol* of feed, the reducer step should be stopped, as further feeding would lead to re-oxidation of the iron. This reactor configuration thus allows for the avoidance of reduced iron loss during the reducer regime.

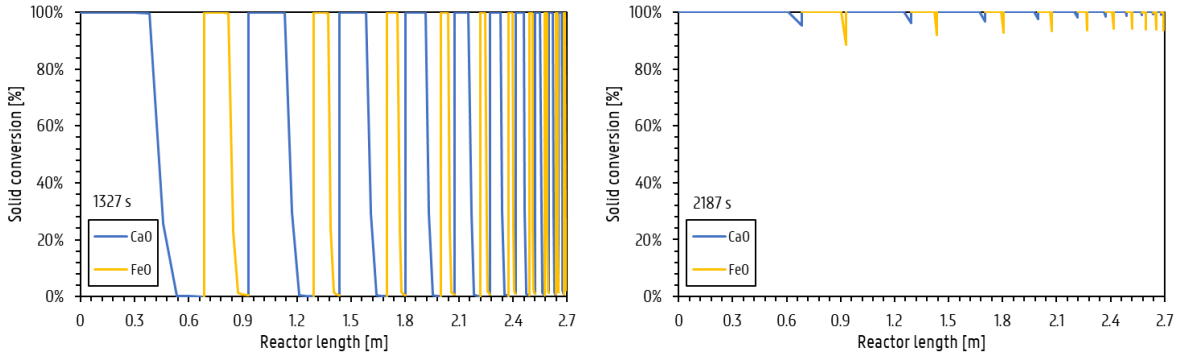

(a) (b)

Figure 8-18: Conversion profile in reactor with alternating beds of calcium and iron in equilibrium amount during reducer regime at 1170 K and 15 bar at 1327 s and 2187 s.

The composition inside the reactor – shown by Figure 8-19 – gets closer to the equilibrium of the combined system every successive alternating layer and eventually approximates it at the end of the reactor. This composition profile remains constant inside the reactor until all solids reach full conversion.

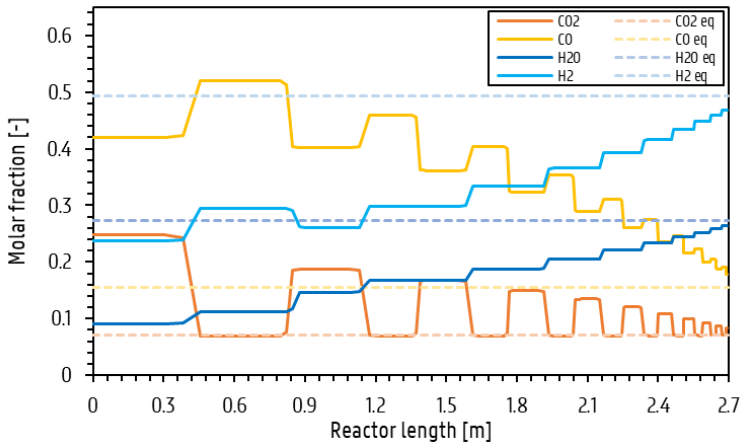

Figure 8-19:Composition profile in reactor with alternating beds of calcium and iron in equilibrium amount during reducer regime at 1170 K and 15 bar at 1327 s.

The simulation is also further run in the oxidizer regime. Herein, calcination could take place closest to the product outlet, as the pressure is the lowest here It could be seen that an extract product with a purity of 68 *mol%* CO and 32 *mol%* CO_2 is produced. The oxidizer step, however, only continues until 49% of the $CaCO_3$ is carbonated and 54% of the Fe is oxidized. At this point, the pressure drop over the bed yields a too high pressure in the beginning of the bed and whilst there is no calcium present together with iron, there is no enhancing effect that can overcome this. Consequently, a self-purge is not able to fully oxidize the bed. An additional purge step with the raffinate product allows for further regeneration of the bed, by which an outlet composition of poor quality is obtained; 49 *mol%* CO, 23 *mol%* CO_2, 18 *mol%* H_2 and 10 *mol%* H_2O.

Although the alternating layers with equilibrium amount of solids indicate to be beneficial for reducer regime with respect to avoiding the re-oxidation of iron, it only has poor performance in the oxidizer regime in case a self-purge and additional purge is used. Moreover, the practicality of the process can not be justified for industrial purpose as the loading of the alternating layers inside the reactor would be too time consuming. For industrial processes, a fully mixed bed will be preferred.

Chapter 9

Conclusions & further research

9.1. Conclusive remarks

A novel combined chemical looping process further enhances CO_2 utilization after a dry reformer reactor for the production of high purity CO. The process consists of two chemical looping systems; i.e. iron looping for RWGS redox reactions and calcium looping for inherent CO_2 capture. The process is split in two separate operating regimes; i.e. a reducer and a oxidizer regime. In the reducer regime, the syngas from the dry reformer is used to reduce the iron solid, thereby producing H_2O and CO_2. The reduction is further enhanced by inherent CO_2 capture on the calcium solid. In the oxidizer regime, the CO_2 captured on the calcium solid is released by calcination and so re-oxidizes the reduced iron, thereby producing a high purity CO product stream. The process is operated in an isothermal packed bed reactor and the looping between the reducer and oxidizer regime is done by means of a pressure swing operation.

In this work, a first dynamic simulation – of the combined chemical looping process using a pressure swing operation – is performed through an equilibrium process simulation in Aspen Adsorption© to gain insight in the dynamic behavior of the process. An equilibrium model based on adsorption isotherms is developed and implemented within the simulation software. Herein, all gas-solid reactions are presented by adsorption processes that take place depending on the departure from their corresponding thermodynamic equilibrium. FactSage© is used for the construction of equilibrium relationships that further serve as the basis for the selection of the operating conditions in this work; i.e. an isothermal temperature of 1170 *K* and a feed pressure of 15 *bar* in the reducer regime and 1 bar in the oxidizer regime.

After a verification of the simulation for a separate calcium and iron bed, the equilibrium model is used for the dynamic simulation of the combined chemical looping process. Principles of pressure swing adsorption are used to configure a process cycle in which the pressure swing operation is used, yielding four distinct steps through which is cycled.

In the first, pressurization step, the bed pressure is increased to reach the required reducer pressure of 15 *bar*. In the second, reducer step, the reactor is operated in the reducer regime by feeding the syngas at 15 *bar*. During this step, reduction of iron and carbonation of calcium takes place. A raffinate product close to the equilibrium composition, that is poor in CO and

CO_2, is withdrawn. Thereafter, in the third oxidizer step, the reactor is operated in the oxidizer regime by decreasing the pressure to 1 *bar*. The release of CO_2 by a co-current self-purging mechanism is confirmed and by re-oxidation of the reduced iron, an extract product close to the equilibrium composition of 68.7 *mol%* CO is obtained. In the last purge step, the bed is regenerated by making use of a co-current purge with the raffinate product.

Although, the simulation does not yield the exact equilibrium compositions because of relaxed solver options, they remain within acceptable limits. The simulation confirms the operating concept of the combined chemical looping process using a pressure swing operation and provides key insights in the dynamic behavior of the reducer and oxidizer regime. In the reducer regime, it is found that in the beginning of the reactor bed, a significant amount of reduced iron is re-oxidized by the feed because of the saturation of calcium; 20% of the reduced iron is re-oxidized in the simulated case. In the oxidizer regime, it is found that only the $CaCO_3$ present together with the reduced iron is able to be recovered. These observations significantly affect the performance of the process.

A sensitivity analysis reveals that the solid composition of the bed dictates the operating behavior in the reducer regime. It is found that the re-oxidation of the reduced iron at the inlet of the reactor is inevitable. It can, however, be minimized by using an input ratio of iron and calcium equal to a so-called "*oxidizing ratio*", which is equal to the equilibrium partial pressure of CO with respect to its reaction with iron. Deviation from this optimal input ratio yields inferior performance in terms of fraction of re-oxidized iron and distribution of carbonated calcium and reduced iron. An increasing feed pressure is found to be superior in terms of the fraction of reduced iron and the retention of CO and CO_2 during the reducer regime. However, at high pressures the difference in performance is minor and consequently a pressure of 15 *bar* is a good trade-off between cost of compressor operation and achievable process performance.

As a first dynamic simulation, the equilibrium approach provides numerous insights into challenges of the process that could not have been assessed without the dynamic nature. These insights can be used to decide up on the viability of the process in terms of reactor selection and performance.

9.2. Future simulation recommendations

The equilibrium representation of the gas-solid reaction by the adsorption isotherms introduced some challenges and limitations to the simulation. On the one hand, the adsorption isotherm approach are limited to only one sorbent that represents both solids at the same time in Aspen Adsorption©. Consequently, an *a priori* assignment of a maximal loading capacity has to be done for each reaction which limits the flexibility of the process. On the other hand, as a

consequence of the assignment of a specific loading for each reaction, there is no interaction possible between the loading of the different reaction – i.e. the reduced/oxidized iron by the H_2/H_2O reaction cannot be reoxidized by CO_2 reaction or *vice versa*. Consequently, the simulation does not represent completely accurate results. Nevertheless, the model is determined to be suitable for the conceptual analysis which is the purpose of this work.

The isotherm approach was found to be the only working strategy for equilibrium simulations during the time of this thesis. There are, however, other option available within the Aspen Adsorption© simulator. One can make use of simple kinetic expressions that yield instantaneous equilibrium of the corresponding reactions. Herein, distinct solids can be defined for calcium and iron components. Moreover, each gas component can interact with this solid and thus the limitations of the adsorption isotherm can be overcome.

The isothermal equilibrium approach used in this work is, however, a very simplified representation of the real process, i.e. the actual heat management is not considered because of the isothermal operation and there are no differences in reactions rate considered by assuming instantaneous equilibrium. Consequently, a complete model still requires further research in the latter two steps:

- **Heat management:** by considering a simulation with non-isothermal operation of the process, more insight can be found on the viability of isothermal operation. Herein, the energy balance should consider all of the possible effects, namely; the compression and expansion heat effects, Joule-Thompson effects by valves, heat of reactions and heat transfer in the reactor. This should provide insight on the possibility of autothermal operation or heat and/or cooling requirements of the process.

- **Full kinetic model:** there is a wide variety of kinetic models in literature that not always suit the exact reactor conditions and environment as used in the combined chemical looping process. Moreover, there is no real agreement on the proposed kinetic models. Therefore, an experimental setup is crucial to validate and differentiate between the available kinetic models.

Furthermore, the Aspen Adsorption© flowsheet simulator can also be used for investigating the operation of the combined chemical looping process using an inert sweep gas to enhance the calcination in the oxidizer regime, as a purge step in the proposed cycle indicated to have the same effect.

This thesis is thus only one of the first steps and certainly not an end point in the development of an accurate and complete dynamic simulation of the combined chemical looping process for high purity CO production.

References

[1] Intergovernmental Panel on Climate Change, “Global Warming of 1.5 ºC,” 2021. https://www.ipcc.ch/sr15/ (accessed Jan. 27, 2021).

[2] European Commission, “COMMUNICATION FROM THE COMMISSION TO THE EUROPEAN PARLIAMENT, THE EUROPEAN COUNCIL, THE COUNCIL, THE EUROPEAN ECONOMIC AND SOCIAL COMMITTEE AND THE COMMITTEE OF THEREGIONS: The European Green Deal.” European Commission, Nov. 12, 2019.

[3] “CO2 Utilization Pathways: Techno-Economic Assessment and Market Opportunities | Elsevier Enhanced Reader.” https://reader.elsevier.com/reader/sd/pii/S1876610214026496?token=72CF1F30175E0A17E0396AE339E33FB968B32DB59CCC1A84B4572FEBA74384D5993B647A63D1A77FFCD51A241A8332A4 (accessed Jan. 26, 2021).

[4] M. V. Dael, “Market study report CCU,” p. 49, Dec. 2018.

[5] P. Summa, B. Samojeden, and M. Motak, “Dry and steam reforming of methane. Comparison and analysis of recently investigated catalytic materials. A short review.,” *Pol. J. Chem. Technol.*, vol. 21, no. 2, pp. 31–37, Jun. 2019, doi: 10.2478/pjct-2019-0017.

[6] X. Wang, J. Wei, and J. Zhang, “Can Steam- and CO-Rich Streams Be Produced Sequentially in the Isothermal Chemical Looping Super-Dry Reforming Scheme?,” *ACS Omega*, vol. 5, no. 10, pp. 5401–5406, Mar. 2020, doi: 10.1021/acsomega.9b04464.

[7] Linde, “Carbon Monoxide,” *Linde Gas*, 2021. https://www.linde-gas.com/en/products_and_supply/packaged_chemicals/product_range/carbon_monoxide.html (accessed Jan. 27, 2021).

[8] D. Claus, “Process simulation of CO2 utilization through Super-Dry Reforming,” UGent, Gent, 2019.

[9] L. C. Buelens, V. V. Galvita, H. Poelman, C. Detavernier, and G. B. Marin, “Super-dry reforming of methane intensifies CO2 utilization via Le Chateliers principle,” *Science*, vol. 354, no. 6311, pp. 449–452, Oct. 2016, doi: 10.1126/science.aah7161.

[10] “moonshotflanders.be.” https://moonshotflanders.be/ (accessed May 17, 2021).

[11] Catalisti, “SDR,” *Flanders Industry Innovation Moonshot*, 2021. https://moonshotflanders.be/mot3-sdr/ (accessed Jan. 27, 2021).

[12] “SYN-CAT – moonshotflanders.be.” https://moonshotflanders.be/mot3-syn-cat/ (accessed May 17, 2021).

[13] “D2M – moonshotflanders.be.” https://moonshotflanders.be/mot3-d2m/ (accessed May 17, 2021).

[14] “Electrification & Radical Process Transformation – moonshotflanders.be.” https://moonshotflanders.be/mot3-electrification-and-radical-process-transformation/ (accessed May 17, 2021).

[15] North-CCU-Hub, “North-CCU-hub – Towards a climate-neutral economy in North Sea Port,” 2021. https://northccuhub.eu/nl/ (accessed Jan. 27, 2021).

[16] M. Wenzel, L. Rihko-Struckmann, and K. Sundmacher, “Continuous production of CO from CO2 by RWGS chemical looping in fixed and fluidized bed reactors,” *Chem. Eng. J.*, vol. 336, pp. 278–296, Mar. 2018, doi: 10.1016/j.cej.2017.12.031.

[17] R. K. Parsapur, S. Chatterjee, and K.-W. Huang, “The Insignificant Role of Dry Reforming of Methane in CO2 Emission Relief,” *ACS Energy Lett.*, vol. 5, no. 9, pp. 2881–2885, Sep. 2020, doi: 10.1021/acsenergylett.0c01635.

[18] M. Ishida, D. Zheng, and T. Akehata, “Evaluation of a chemical-looping-combustion power-generation system by graphic exergy analysis,” *Energy*, vol. 12, no. 2, pp. 147–154, Feb. 1987, doi: 10.1016/0360-5442(87)90119-8.

[19] M. M. Hossain and H. I. de Lasa, “Chemical-looping combustion (CLC) for inherent CO2 separations—a review,” *Chem. Eng. Sci.*, vol. 63, no. 18, pp. 4433–4451, Sep. 2008, doi: 10.1016/j.ces.2008.05.028.

[20] A. A. A. Solieman, J. W. Dijkstra, W. G. Haije, P. D. Cobden, and R. W. van den Brink, “Calcium oxide for CO2 capture: Operational window and efficiency penalty in sorption-enhanced steam methane reforming,” *Int. J. Greenh. Gas Control*, vol. 3, no. 4, pp. 393–400, Jul. 2009, doi: 10.1016/j.ijggc.2009.02.002.

[21] L. C. Buelens, V. V. Galvita, H. Poelman, C. Detavernier, and G. B. Marin, “Supplementary material for: Super-dry reforming of methane intensifies CO2 utilization via Le Chateliers principle,” *Science*, vol. 354, no. 6311, pp. 449–452, Oct. 2016, doi: 10.1126/science.aah7161.

[22] H. P. Hamers, M. C. Romano, V. Spallina, P. Chiesa, F. Gallucci, and M. van S. Annaland, “Comparison on process efficiency for CLC of syngas operated in packed bed and fluidized bed reactors,” *Int. J. Greenh. Gas Control*, vol. 28, pp. 65–78, Sep. 2014, doi: 10.1016/j.ijggc.2014.06.007.

[23] B. Moghtaderi, “Review of the Recent Chemical Looping Process Developments for Novel Energy and Fuel Applications,” *Energy Fuels*, vol. 26, no. 1, pp. 15–40, Jan. 2012, doi: 10.1021/ef201303d.

[24] Z. Zhou, L. Han, and G. M. Bollas, “Overview of Chemical-Looping Reduction in Fixed Bed and Fluidized Bed Reactors Focused on Oxygen Carrier Utilization and Reactor Efficiency,” *Aerosol Air Qual. Res.*, vol. 14, no. 2, pp. 559–571, 2014, doi: 10.4209/aaqr.2013.06.0198.

[25] L. Han and G. M. Bollas, “Dynamic optimization of fixed bed chemical-looping combustion processes,” *Energy*, vol. 112, pp. 1107–1119, Oct. 2016, doi: 10.1016/j.energy.2016.07.031.

[26] J. Adanez, A. Abad, F. Garcia-Labiano, P. Gayan, and L. F. de Diego, “Progress in Chemical-Looping Combustion and Reforming technologies,” *Prog. Energy Combust. Sci.*, vol. 38, no. 2, pp. 215–282, Apr. 2012, doi: 10.1016/j.pecs.2011.09.001.

[27] J. Blamey, E. J. Anthony, J. Wang, and P. S. Fennell, “The calcium looping cycle for large-scale CO2 capture,” *Prog. Energy Combust. Sci.*, vol. 36, no. 2, pp. 260–279, Apr. 2010, doi: 10.1016/j.pecs.2009.10.001.

[28] C. C. Dean, J. Blamey, N. H. Florin, M. J. Al-Jeboori, and P. S. Fennell, “The calcium looping cycle for CO2 capture from power generation, cement manufacture and hydrogen production,” *Chem. Eng. Res. Des.*, vol. 89, no. 6, pp. 836–855, Jun. 2011, doi: 10.1016/j.cherd.2010.10.013.

[29] S. Zhang, R. Xiao, and W. Zheng, “Comparative study between fluidized-bed and fixed-bed operation modes in pressurized chemical looping combustion of coal,” *Appl. Energy*, vol. 130, pp. 181–189, Oct. 2014, doi: 10.1016/j.apenergy.2014.05.049.

[30] V. Spallina, F. Gallucci, and M. van Sint Annaland, “Chemical Looping Processes Using Packed Bed Reactors,” in *Handbook of Chemical Looping Technology*, R. W. Breault, Ed. Weinheim, Germany: Wiley-VCH Verlag GmbH & Co. KGaA, 2018, pp. 61–92. doi: 10.1002/9783527809332.ch3.

[31] R. Douglas M., F. Shamsuzzaman, and K. Kent S, *Pressure Swing Adsorption*. United State of America: VCH Publishers, Inc., 1994.

[32] S. Noorman, M. van Sint Annaland, and Kuipers, “Packed Bed Reactor Technology for Chemical-Looping Combustion,” *Ind. Eng. Chem. Res.*, vol. 46, no. 12, pp. 4212–4220, Jun. 2007, doi: 10.1021/ie061178i.

[33] J. Yin, C. Qin, H. An, W. Liu, and B. Feng, “High-Temperature Pressure Swing Adsorption Process for CO2 Separation,” *Energy Fuels*, vol. 26, no. 1, pp. 169–175, Jan. 2012, doi: 10.1021/ef201142w.

[34] P. Heidebrecht and K. Sundmacher, “Thermodynamic analysis of a cyclic water gas-shift reactor (CWGSR) for hydrogen production,” *Chem. Eng. Sci.*, vol. 64, no. 23, pp. 5057–5065, Dec. 2009, doi: 10.1016/j.ces.2009.08.011.

[35] P. Heidebrecht, C. Hertel, and K. Sundmacher, “Conceptual Analysis of a Cyclic Water Gas Shift Reactor,” *Int. J. Chem. React. Eng.*, vol. 6, no. 1, Feb. 2008, doi: 10.2202/1542-6580.1495.

[36] M. Sharma, R. K. Vyas, and K. Singh, “Theoretical and Experimental Analysis of Reactive Adsorption in a Packed Bed: Parallel and Branched Pore-Diffusion Model Approach,” *Ind. Eng. Chem. Res.*, vol. 55, no. 20, pp. 5945–5954, May 2016, doi: 10.1021/acs.iecr.5b04223.

[37] J. C. Abanades, R. Murillo, J. R. Fernandez, G. Grasa, and I. Martínez, “New CO2 Capture Process for Hydrogen Production Combining Ca and Cu Chemical Loops,” *Environ. Sci. Technol.*, vol. 44, no. 17, pp. 6901–6904, Sep. 2010, doi: 10.1021/es101707t.

[38] F. N. Ridha, D. Lu, A. Macchi, and R. W. Hughes, “Combined calcium looping and chemical looping combustion cycles with CaO–CuO pellets in a fixed bed reactor,” *Fuel*, vol. 153, pp. 202–209, Aug. 2015, doi: 10.1016/j.fuel.2015.02.069.

[39] A. Arora, “GRAMS: A general framework describing adsorption, reaction and sorption-enhanced reaction processes,” *Chem. Eng. Sci.*, p. 24, 2018.

[40] A. Arora, S. S. Iyer, I. Bajaj, and M. M. F. Hasan, “Optimal Methanol Production via Sorption-Enhanced Reaction Process,” *Ind. Eng. Chem. Res.*, vol. 57, no. 42, pp. 14143–14161, Oct. 2018, doi: 10.1021/acs.iecr.8b02543.

[41] D. K. Lee, I. H. Baek, and W. L. Yoon, “Modeling and simulation for the methane steam reforming enhanced by in situ CO2 removal utilizing the CaO carbonation for H2 production,” *Chem. Eng. Sci.*, vol. 59, no. 4, pp. 931–942, Feb. 2004, doi: 10.1016/j.ces.2003.12.011.

[42] K. R. Wood, Y. A. Liu, and Y. Yu, *Design, Simulation and Optimization of Adsorptive and Chromatographic Separations: A Hands-On Approach*. Weinheim, Germany: Wiley-VCH Verlag GmbH & Co. KGaA, 2018. doi: 10.1002/9783527815029.

[43] G. Keith, *Adsorption technology and design*. 1998.

[44] J. W. Niemantsverdriet and I. Chorkendorff, *Concepts of Modern Catalysis and Kinetics*. Wiley-VCH, 2003.

[45] L. Rahmanzadeh, “Sorption-enhanced ethanol steam reforming on Ce-Ni/MCM-41 with simultaneous CO2 adsorption over Na- and Zr- promoted CaO based sorbent,” *N T E R N T O N J O U R N O F H R O G E N E N E R G*, p. 13.

[46] H. Guo, Z. Xu, T. Jiang, Y. Zhao, X. Ma, and S. Wang, “The effect of incorporation Mg ions into the crystal lattice of CaO on the high temperature CO2 capture,” *J. CO2 Util.*, vol. 37, pp. 335–345, Apr. 2020, doi: 10.1016/j.jcou.2020.01.012.

[47] L. Yang, H. Yu, S. Wang, H. Wang, and Q. Zhou, “Carbon Dioxide Captured from Flue Gas by Modified Ca-based Sorbents in Fixed-bed Reactor at High Temperature,” *Chin. J. Chem. Eng.*, vol. 21, no. 2, pp. 199–204, Feb. 2013, doi: 10.1016/S1004-9541(13)60459-0.

[48] C. S. Martavaltzi, E. P. Pampaka, E. S. Korkakaki, and A. A. Lemonidou, “Hydrogen Production via Steam Reforming of Methane with Simultaneous CO_2 Capture over $CaO-Ca_{12}Al_{14}O_{33}$,” *Energy Fuels*, vol. 24, no. 4, pp. 2589–2595, Apr. 2010, doi: 10.1021/ef9014058.

[49] X. Zhu, S. Li, Y. Shi, and N. Cai, “Recent advances in elevated-temperature pressure swing adsorption for carbon capture and hydrogen production,” *Prog. Energy Combust. Sci.*, vol. 75, p. 100784, Nov. 2019, doi: 10.1016/j.pecs.2019.100784.

[50] AspenTech, “Aspen Adsorption V11 Help.” Oct. 13, 2020.

[51] S. Sircar, “PRESSURE SWING ADSORPTION TECHNOLOGY FOR HYDROGEN PURIFICATION - A STATUS REVIEW,” in *Adsorption*, Tianjin, China, Sep. 2007, pp. 29–45. doi: 10.1142/9789812770264_0002.

[52] H. Li, Z. Liao, J. Sun, B. Jiang, J. Wang, and Y. Yang, “Modelling and simulation of two-bed PSA process for separating H2 from methane steam reforming,” *Chin. J. Chem. Eng.*, vol. 27, no. 8, pp. 1870–1878, Aug. 2019, doi: 10.1016/j.cjche.2018.11.022.

[53] J. Boon, P. D. Cobden, H. A. J. van Dijk, and M. van Sint Annaland, “High-temperature pressure swing adsorption cycle design for sorption-enhanced water–gas shift,” *Chem. Eng. Sci.*, vol. 122, pp. 219–231, Jan. 2015, doi: 10.1016/j.ces.2014.09.034.

[54] Z. Liu and W. H. Green, “Analysis of Adsorbent-Based Warm CO2 Capture Technology for Integrated Gasification Combined Cycle (IGCC) Power Plants,” *Ind. Eng. Chem. Res.*, vol. 53, no. 27, pp. 11145–11158, Jul. 2014, doi: 10.1021/ie4030006.

[55] J. W. Butler, C. J. Lim, and J. R. Grace, “CO2 capture capacity of CaO in long series of pressure swing sorption cycles,” *Chem. Eng. Res. Des.*, vol. 89, no. 9, pp. 1794–1804, Sep. 2011, doi: 10.1016/j.cherd.2010.10.004.

[56] G. Tomaszewicz, M. Kotyczka-Morańska, and A. Plis, “Studies on the carbonation of Czatkowice limestone in Calcium Looping process,” *Pol. J. Chem. Technol.*, vol. 18, no. 2, pp. 53–58, Jun. 2016, doi: 10.1515/pjct-2016-0029.

[57] A. Scaltsoyiannes, A. Antzaras, G. Koilaridis, and A. Lemonidou, “Towards a generalized carbonation kinetic model for CaO-based materials using a modified random pore model,” *Chem. Eng. J.*, p. 127207, Oct. 2020, doi: 10.1016/j.cej.2020.127207.

[58] S. K. Bhatia and D. D. Perlmutter, “Effect of the product layer on the kinetics of the CO2-lime reaction,” *AIChE J.*, vol. 29, no. 1, pp. 79–86, Jan. 1983, doi: 10.1002/aic.690290111.

[59] L. Fedunik-Hofman, A. Bayon, and S. W. Donne, “Kinetics of Solid-Gas Reactions and Their Application to Carbonate Looping Systems,” *Energies*, vol. 12, no. 15, p. 2981, Aug. 2019, doi: 10.3390/en12152981.

[60] A. Scaltsoyiannes and A. Lemonidou, “CaCO3 decomposition for calcium-looping applications: Kinetic modeling in a fixed-bed reactor,” *Chem. Eng. Sci. X*, vol. 8, p. 100071, Nov. 2020, doi: 10.1016/j.cesx.2020.100071.

[61] A. Scaltsoyiannes, A. Antzara, and A. Lemonidou, “LIMESTONE AND DOLOMITE AS THERMOCHEMICAL ENERGY STORAGE MATERIALS: REACTION KINETICS AND DEACTIVATION MODELING,” p. 6, 2019.

[62] P. Sun, J. R. Grace, C. J. Lim, and E. J. Anthony, “Determination of intrinsic rate constants of the CaO–CO2 reaction,” *Chem. Eng. Sci.*, vol. 63, no. 1, pp. 47–56, Jan. 2008, doi: 10.1016/j.ces.2007.08.055.

[63] R. H. Borgwardt, “Calcination kinetics and surface area of dispersed limestone particles,” *AIChE J.*, vol. 31, no. 1, pp. 103–111, Jan. 1985, doi: 10.1002/aic.690310112.

[64] W. Liu, “Kinetics of the reduction of wüstite by hydrogen and carbon monoxide for the chemical looping production of hydrogen,” *Chem. Eng. Sci.*, p. 18, 2014.

[65] L. Buelens, “Process Concept and Materials for Carbon Dioxide Capture and Conversion: Super-Dry Reforming of Methane.” UGent, 2019 2018.

[66] M. G. Plaza, I. Durán, N. Querejeta, F. Rubiera, and C. Pevida, “Experimental and Simulation Study of Adsorption in Postcombustion Conditions Using a Microporous Biochar.

1. CO_2 and N_2 Adsorption," *Ind. Eng. Chem. Res.*, vol. 55, no. 11, pp. 3097–3112, Mar. 2016, doi: 10.1021/acs.iecr.5b04856.

[67] C. W. Bale, "FactSage Thermochemical Software and Databases," p. 40.

[68] "Sigmoid function," *Wikipedia*. May 06, 2021. Accessed: May 15, 2021. [Online]. Available: https://en.wikipedia.org/w/index.php?title=Sigmoid_function&oldid=1021825762